STRUCTURAL INVESTIGATIONS ON SEMICONDUCTOR NANOSTRUCTURES

-WET CHEMICAL APPROACHES FOR THE SYNTHESIS OF NOVEL FUNCTIONAL STRUCTURES

RAJEEVAN KOZHUMMAL

Graduation committee

Chairman

Prof. dr. P.M.G. Apers   University of Twente, The Netherlands

Promoters

Prof. dr. Miko Elwenspoek   University of Twente, The Netherlands

Prof. dr. Margit Zacharias   University of Freiburg, Germany

Members

Prof. dr. Martin Steinhart   University of Osnabrück, Germany

Prof. dr. Han Gardeniers   University of Twente, The Netherlands

Prof. dr. ir. Jurriaan Huskens   University of Twente, The Netherlands

Dr. ir. N. A. M. Besseling   TUDelft, The Netherlands

Dr.ir. Léon Woldering   University of Twente, The Netherlands

Cover design by Rajeevan Kozhummal

Front cover: SEM images of ZnO nanowire array and modified morphologies. Back cover: SEM images of CuI superstructures prepared by antisolvent crystallization without and with polymer additives (top). A smiley is drawn on the SEM image of a CuI superstructure (bottom).

STRUCTURAL INVESTIGATIONS ON SEMICONDUCTOR NANOSTRUCTURES

-WET CHEMICAL APPROACHES FOR THE SYNTHESIS OF NOVEL FUNCTIONAL STRUCTURES

DISSERTATION

to obtain
the degree of doctor at the University of Twente,
on the authority of the rector magnificus
Prof. dr. H. Brinksma
on account of the decision of the graduation committee,
to be publicly defended
on Friday 24th October 2014 at 14:45 hours

By

Rajeevan Kozhummal

born on 18th April 1986

at Karivellur, Kannur, India

This dissertation is approved by

Prof. dr. Miko Elwenspoek   University of Twente, The Netherlands

Prof. dr. Margit Zacharias   University of Freiburg, Germany

Dedicated to my father

Abstract

Recently nanotechnology is experiencing a flourishing progress in a variety of arenas from science to engineering and to biology. The fabrication of nanoscale building blocks, understanding their properties, and organizing these building blocks in to devices for various applications are the main objectives of nanotechnology. As an active field in nanotechnology, the work presented in this thesis is mostly focused on the fundamental study about the fabrication of functional semiconductor nanostructures by wet chemical approaches. In particular, the effects of structure-directing agents, which is the core objective of this research are discussed in detail. Zinc oxide is intrinsically an n-type semiconducting materials that finds applications in electronics, optics, and catalysis. ZnO nanowires have been emerged as a potential candidate in various modern devices with enhanced efficiency. Hydrothermal growth is a widely used technique for the synthesis of ZnO nanowires owing to cost effectiveness, simplicity, and easy upscaling. The use of a polymer additive, polyethylene glycol in the reaction medium has a huge effect on the final morphology of the prepared structures. This method is used to grow hexabranched ZnO nanostructures with increased total and polar surface area. The structures have shown enhanced photocatalytic activity than the conventional nanowires. ZnO based heterostructures have attracted research attention in recent years for their novel interface properties. Controlled secondary growth approaches using organic capping agents, in combination with doping, have been intrigued for the preparation of ZnO core-shell nanowires. Thus Sb-doped and Co-doped ZnO core-shell nanowires have been prepared by this method. The Sb-doped ZnO core-shell nanowires have been synthesized using polyethylene glycol-assisted process in aqueous medium. The Co-doped ZnO core-shell nanowires have been prepared in ethylene glycol-assisted process where ethylene glycol acts both as the growth medium and a structure-directing agent. Since both the routes use a secondary growth method, the shell is grown on an already prepared nanowire core; the dopants are selectively distributed in the shell. CuI is intrinsically a p-type semiconductor that is mainly studied for its applications in the fields of solar energy conversion, catalysis, and solid electrolytes. In the later chapters, antisolvent crystallization of CuI nanoparticles and their assembly to form superstructures are discussed. This process also has been tuned using polymer additives to obtain specific morphologies with high porosity. Owing to the chemical flexibility of CuI to convert to other materials, the superstructures have been used as sacrificial templates to fabricate highly convoluted and porous CuO and TiO_2 structures. When the CuI superstructures prepared by polymer assisted assembly has been used as

adsorbents, they showed a high adsorption capability. As mentioned above, the works presented in this thesis are fundamental study on the synthesis of functional semiconductor nanostructures. In general, this study gives an account on the effect of specific structure-directing agents on the morphology and optimized synthetic routes for the preparation of specific semiconductor nanostructures with desired structures.

Contents

1 General Introduction

In device designs the concept of going small in size is often associated with aesthetics and enhanced utility. But miniaturization in materials science and engineering has lead to a new realm of understanding, encouraged by the dramatic changes in physical properties observed at smaller sizes. The effects were extensive than the expected properties triggered by the expanded surface area. For example, the color of light emitted from CdSe nanoparticles changes with their sizes;[1] the melting point of gold nanoparticles drops considerably when their size is about 2 Å;[2] carbon nanotubes are found to be the strongest and stiffest materials on earth so far, in terms of tensile strength and elastic modulus.[3–5] The changes in electrical and optical properties in the domain of smaller dimensions are due to quantum effect, which is the physics that governs the motion and interaction of electrons in atoms.

Nanotechnology is the preparation and use of functional materials designed from atomic or molecular scale with at least one characteristic dimension measured in nanometers. The rational control over the size of matter on that scale allows the tailoring of macroscopic physical, chemical, and biological properties. Nanostructured materials comprise atomic clusters, films, filamentary structures, and bulk nanostructured materials. Over the last two decades nanotechnology is experiencing a flourishing development in various fields of

science and engineering. The rapid advances in the field of nanotechnology and nanoscience have offered an array of nanoscale materials with highly controlled and distinctive electrical, optical, magnetic, or catalytic properties.[6–16] Engineering the composition (inorganic or organic, metals or semiconductors), shape (particles, rods, wires, tubes, films), and the surface functionalization (physical, chemical, or biological) have spawned many nanoscale devices. [7,14,15,17–19] But the design and synthesis of nanoscale materials with controlled properties is a significant and ongoing challenge within nanotechnology.

Semiconductor nanostructures, owing to their large surface area or quantum size effects, are promising for applications in many fields such as solar cells, nanoscale electronic devices, light-emitting nano devices, laser technology, waveguides, chemical and biosensors, and catalysts.[20] Broad selection of compositions and band structures make these semiconductor nanostructures potential components in a wide range of nanoscale device applications. In order to fully utilize these nanostructures the current research has focused on the rational synthetic control of nanoscale building blocks, novel properties characterization and device fabrication based on these nanostructures.

The synthesis and characterization of nanomaterials and the construction of devices are two main research areas in nanoscience. Nanosynthesis is majorly operated through various physical and chemical methods. The major inherent advantages of wet chemical methods in comparison with high temperature processes lie in low cost, low synthesis temperature, mild and environmentally benign reaction conditions as well as easy scaling up.

Zinc oxide (ZnO) is an important multifunctional semiconducting oxide which is widely used in energy conversion, electronics, optics, catalysis, and sensing.[21–32] The development of hydrothermal synthesis has prominently stimulated bottom-up nanosynthesis for the growth of various ZnO nanostructures.[26–37] Moreover, a distinctive advantage emerging *via* this approach is the possibility of providing ZnO nanostructures with specific morphology or arrangement, which are directly linked to the functional requirements of practical devices for optimal performances.[26–32,38,39] For instance, well-aligned crystalline ZnO nanowires have been grown on flexible organic substrates, compatible with the design of inorganic–organic hybrid LEDs.[38] High throughput fabrication of patterned ZnO nanowire arrays on a wafer scale has been readily achieved by combination with different lithographic techniques, which is especially of use in ZnO-based light emitters and electrochromic displays.[39]

It is considered that molecular structure-directing agents play a significant role in the kinetic control of the nanocrystal growth by preferentially adsorbing onto specific crystal

faces, thus impeding growth of that surface. Organic and inorganic additives have been widely added to the wet chemical nanosynthesis for designed morphology.[30,34] For example, in the presence of polyvinyl pyrrolidone (PVP), most silver particles can be directed to grow into nanowires with uniform diameters owing to the preferential bonding of the PVP to specific faces.[40] Similarly in the synthesis of ZnO nanowires, structure-directing agents (capping agents or soft templates) with preferential binding abilities on specific ZnO crystal surfaces in low-temperature alkaline hydrothermal synthesis have been used for systematic manipulation of the aspect ratio of ZnO nanowires toward the goal of morphology-coupled photocatalytic activity or field emission.[28,30]

In *Chapter 2*, the growth of ZnO nanowires by wet chemical process is discussed. The influence of polyethylene glycol (PEG) as a structure-directing agent to inhibit the axial growth of ZnO nanowires to obtain controlled radial growth is discussed in *Chapter 3*. PEG– assisted growth of ZnO nanowires, when used for secondary growth can be used for site-selective doping of ZnO nanowires as described in *Chapter 4*. This pathway also can be modified using ethylene glycol which offers a non-aqueous route for transition metal doped ZnO core-shell nanowires as demonstrated in *Chapter 5*.

Synthesis of inorganic micro and nanostructures with well-defined morphology plays a significant role in uncovering their shape-dependent properties and fully realizing their prospective practical applications. Controlled self-organization of nanoparticles can lead to materials with novel properties. These superstructures or mesocrystals represent a class of functional materials that drew research attention for their large surface area, controllable level of porosity, crystallinity of subunits, oriented subunit alignment, and complex 3D network structure. Mesocrystals are structures composed of nanocrystal subunits aligned in a crystallographic pattern but separated by porosity or a second phase. They are formed non-classically, through the growth process typically by the integration of classically crystallized subunits in an oriented manner *via* mesoscale assembly.[42,43] CuI is intrinsically a p-type semiconductor (direct band gap 3.1 eV) which is constantly studied for its applications in the fields of solar energy conversion,[44–47] catalysis,[48–50] and solid electrolyte.[51] The formation of CuI superstructures by an anti-solvent crystallization process is demonstrated in *Chapter 6*. Since the assembly of colloidal subunits leads to the superstructures, organic additives can be used to control the formation and resultant morphology. Organic additives act as structure-directing agents in the formation of these superstructures, because of their ability to adhere to the subunits partially or fully depending on the nature of surfaces and the additives used. In

Chapter 7, the role of polyvinyl pyrrolidone (PVP), an organic additive, in the process of anti-solvent crystallization of CuI and the following morphology is demonstrated.

A major constraint of the synthetic approach using structure-directing agents is that most of the capping agents are selected *via* an empirical trial and error methodology.[41] As far as the works presented in this thesis are concerned, the structure-directing agents have been chosen based on the coordinating abilities of additives such as polyethylene glycol (PEG), ethylene glycol, and PVP with specific ZnO and CuI crystal facets. As a dynamic field in nanotechnology, the works discussed here are mostly focused on the fundamental study about the fabrication of functional semiconductor structures by wet chemical methods, which are envisioned to be potential building blocks of modern devices.

In addition to the core part of the thesis, a method to prepare micron-sized tetrahedral structures bounded by (111) faces by micromachining of (111)-oriented silicon wafers is appended as *Appendix 1*. The detailed description of experimental procedures is given as *Appendix 2*. In general this thesis is based on the papers published, which are accordingly stated in the beginning of each individual chapters. In addition to the data presented in the papers, additional results are also included in this thesis. The list of publications is given at the end of this book.

References

[1]   A. P. Alivisatos, A. L. Harris, N. J. Levinos, M. L. Steigerwald, L. E. Brus, *J. Chem. Phys.* **1988**, *89*, 4001.

[2]   P. Buffat, J.-P. Borel, *Phys. Rev. A* **1976**, *13*, 2287.

[3]   P. Poncharal, Z. L. Wang, D. Ugarte, W. A. de Heer, *Science* **1999**, *283*, 1513.

[4]   M.-F. Yu, O. Lourie, M. J. Dyer, K. Moloni, T. F. Kelly, R. S. Ruoff, *Science* **2000**, *287*, 637.

[5]   J.-P. Salvetat, G. A. D. Briggs, J.-M. Bonard, R. R. Bacsa, A. J. Kulik, T. Stöckli, N. A. Burnham, L. Forró, *Phys. Rev. Lett.* **1999**, *82*, 944.

[6]   J. F. Hicks, F. P. Zamborini, A. J. Osisek, R. W. Murray, *J. Am. Chem. Soc.* **2001**, *123*, 7048.

[7]   A. P. Alivisatos, *J. Phys. Chem.* **1996**, *100*, 13226.

[8]   J. F. Hicks, D. T. Miles, R. W. Murray, *J. Am. Chem. Soc.* **2002**, *124*, 13322.

[9]   S. Chen, R. W. Murray, *J. Phys. Chem. B* **1999**, *103*, 9996.

[10]   J. F. Hicks, F. P. Zamborini, R. W. Murray, *J. Phys. Chem. B* **2002**, *106*, 7751.

[11]   P. Mulvaney, *Langmuir* **1996**, *12*, 788.

[12]   M. B. Jr., M. Moronne, P. Gin, S. Weiss, A. P. Alivisatos, *Science* **1998**, *281*, 2013.

[13]   L. Brus, *Appl. Phys. A Solids Surfaces* **1991**, *53*, 465.

[14]   A. N. Shipway, E. Katz, I. Willner, *Chemphyschem* **2000**, *1*, 18.

[15]   M.-C. Daniel, D. Astruc, *Chem. Rev.* **2004**, *104*, 293.

[16]   M. M. Alvarez, J. T. Khoury, T. G. Schaaff, M. N. Shafigullin, I. Vezmar, R. L. Whetten, *J. Phys. Chem. B* **1997**, *101*, 3706.

[17]   T. Trindade, P. O'Brien, N. L. Pickett, *Chem. Mater.* **2001**, *13*, 3843.

[18]   P. Schwerdtfeger, *Angew. Chem.* **2003**, *42*, 1892.

[19]   R. Gangopadhyay, A. De, *Chem. Mater.* **2000**, *12*, 608.

[20]   M. Grundmann, *The Physics of Semiconductors*; Graduate Texts in Physics; 2nd ed.; Springer Berlin Heidelberg: Berlin, Heidelberg, 2010.

[21]   H. Morkoc, U. Ozgur, *Zinc Oxide: Fundamentals, Materials and Device Technology*; Wiley-VCH Verlag GmbH & Co. KGaA: Weinheim, Germany, 2009.

[22] M. H. Huang, S. Mao, H. Feick, H. Yan, Y. Wu, H. Kind, E. Weber, R. Russo, P. Yang, *Science* **2001**, *292*, 1897.

[23] M. Law, L. E. Greene, J. C. Johnson, R. Saykally, P. Yang, *Nat. Mater.* **2005**, *4*, 455.

[24] F. Patolsky, C. Lieber, *Mater. today* **2005**, *8*, 20.

[25] Z. L. Wang, J. Song, *Science* **2006**, *312*, 242.

[26] C. Y. Jiang, X. W. Sun, G. Q. Lo, D. L. Kwong, J. X. Wang, *Appl. Phys. Lett.* **2007**, *90*, 263501.

[27] W. Liang, B. D. Yuhas, P. Yang, *Nano Lett.* **2009**, *9*, 892.

[28] A. McLaren, T. Valdes-Solis, G. Li, S. C. Tsang, *J. Am. Chem. Soc.* **2009**, *131*, 12540.

[29] A. L. Briseno, T. W. Holcombe, A. I. Boukai, E. C. Garnett, S. W. Shelton, J. J. M. Fréchet, P. Yang, *Nano Lett.* **2010**, *10*, 334.

[30] J. Joo, B. Y. Chow, M. Prakash, E. S. Boyden, J. M. Jacobson, *Nat. Mater.* **2011**, *10*, 596.

[31] S. Ko, D. Lee, H. Kang, K. Nam, J. Yeo, *Nano Lett.* **2011**, *11*, 666.

[32] Y. Qiu, K. Yan, H. Deng, S. Yang, *Nano Lett.* **2012**, *12*, 407.

[33] A. Taubert, D. Palms, Ö. Weiss, *Chem. Mater.* **2002**, *14*, 2594.

[34] Z. R. Tian, J. A. Voigt, J. Liu, B. McKenzie, M. J. McDermott, M. A. Rodriguez, H. Konishi, H. Xu, *Nat. Mater.* **2003**, *2*, 821.

[35] L. E. Greene, M. Law, D. H. Tan, M. Montano, J. Goldberger, G. Somorjai, P. Yang, *Nano Lett.* **2005**, *5*, 1231.

[36] S. Xu, Y. Wei, M. Kirkham, J. Liu, W. Mai, D. Davidovic, R. L. Snyder, Z. L. Wang, *J. Am. Chem. Soc.* **2008**, *130*, 14958.

[37] S. Xu, Z. L. Wang, *Nano Res.* **2011**, *4*, 1013.

[38] S. Xu, Y. Shen, Y. Ding, Z. L. Wang, *Adv. Funct. Mater.* **2010**, *20*, 1493.

[39] Y. Wei, W. Wu, R. Guo, D. Yuan, S. Das, Z. L. Wang, *Nano Lett.* **2010**, *10*, 3414.

[40] Y. Sun, Y. Yin, B. T. Mayers, T. Herricks, Y. Xia, *Chem. Mater.* **2002**, *14*, 4736.

[41] M. Law, J. Goldberger, P. Yang, *Annu. Rev. Mater. Res.* **2004**, *34*, 83.

[42] Y. Liu, Y. Zhang, J. Wang, *CrystEngComm* **2014**, *16*, 5948.

[43] H. Cölfen, M. Antonietti, *Angew. Chem.* **2005**, *44*, 5576.

[44] H. Chen, C.-Y. Wang, J.-T. Wang, Y. Wu, S.-X. Zhou, *Phys. B Condens. Matter* **2013**, *413*, 116.

[45] J. Zhu, M. Gu, R. Pandey, *Appl. Surf. Sci.* **2013**, *268*, 87.

[46] H. Sakamoto, S. Igarashi, M. Uchida, K. Niume, M. Nagai, *Org. Electron.* **2012**, *13*, 514.

[47] H. Sakamoto, S. Igarashi, K. Niume, M. Nagai, *Org. Electron.* **2011**, *12*, 1247.

[48] P. Wang, L. Li, C. Yang, Y. Li, *J. Phys. Chem. A* **2008**, *112*, 435.

[49] H.-T. Yang, X.-C. Liang, Y.-H. Wang, Y. Yang, X.-Q. Sun, C.-B. Miao, *Org. Lett.* **2013**, *15*, 4650.

[50] P. K. Kalita, P. Phukan, *Tetrahedron Lett.* **2013**, *54*, 4442.

[51] L. Meng, R. Mo, H. Zhou, G. Wang, W. Chen, D. Wang, Q. Peng, *Cryst. Growth Des.* **2010**, *10*, 3387.

2 Hydrothermal Growth of ZnO Nanowires

Zinc oxide (ZnO) nanowires are important functional units that find applications in various fields like energy conversion, electronics, and optics. This chapter gives an introduction on ZnO nanowires, the crystalline structure and the synthetic methods. Hydrothermal synthesis is attractive method for the fabrication of ZnO nanowires owing to the better purity and crystallinity of the structures compared to other physical deposition methods. It involves simple chemical reactions, which allow the use of diverse substrates on which the nanowires can be grown. This wet chemical approach is environmental friendly and highly reproducible. The nature of growth process and the flexibility on the choice of substrates are discussed. The morphology and the crystallinity of the ZnO nanowires grown hydrothermally are also investigated.

2.1 Introduction

ZnO is a group II-VI compound semiconductor with a wide band gap of 3.4 eV. It crystallizes preferentially in the hexagonal wurtzite-type structure. ZnO occurs in nature as zincite mineral ((Zn,Mn)O) which contains a certain amount of manganese and some other elements like iron which gives zincite a yellow to red color. Pure ZnO is colorless and clear material due to its large band gap. Though the research on ZnO has started in 1930s, it thwarted after 1980s. The main reason was the difficulty to dope ZnO in both n- and p-type manner, which is the vital requirement for applications in electronics and optics. The last two decades marked the resurgence of ZnO research that is mainly due to the advent of growth of epitaxial layers, quantum wells, nanowires, quantum dots etc. and successful doping which enabled it for various applications in optoelectronics and spintronics. The major intended applications were (i) as a supplementary/alternative material to GaN-based structures in blue/ultra violet optoelectronics, light emitting or laser diodes, (ii) as a material for transparent electronic circuits in visible light, (iii) as diluted magnetic semiconductor (DMSs) when doped with transition metals (Co, Mn, Fe) for semiconductor spintronics, and (iv) as a cheaper alternative to indium tin oxide (ITO) when doped with group III elements (Al, Ga, In) as a transparent conducting oxide.

2.1.1 ZnO Nanowires

The inherent properties of ZnO combined with the novel developments in the field of nanotechnology fueled and fanned the renaissance in ZnO research in the last decade. There are many nanostructures of ZnO being synthesized and investigated for various applications. Nanowires,[1–5] nanoribbons/belts, [6–8] hierarchical nanostructures,[9–12] bridge and nail-like nanostructures,[13] tubular nanostructures,[14,15] nanosheets,[16–19] nanopropeller arrays,[20,21] nanohelixes,[20,22,23] nanorings,[20,23] etc. are some of them.

Among one-dimensional morphologies of ZnO, nanowires (NWs) are the most extensively studied nanostructures for various applications in the field of electronics, optics, energy conversion, lasing, catalysis, sensing, and spintronics.[24–30] Usually ZnO nanowires are of hexagonal prism shape with diameter ranging from 20-200 nm. The length of the nanowires prepared by different synthetic methods varies from 1-10 μm. with an aspect ratio of about 50-500.

2.1.2 Crystal Structure of ZnO

ZnO nanostructures, nanowires in particular, are the platform used to develop functional materials in this and following three chapters. So as to manipulate the morphology and thereby to exploit the structure-related properties, basic understanding of the material such as crystal structure and nature of growth is in order. ZnO crystallizes in three forms under different conditions. The wurtzite form is the most common since it is the most stable structure at ambient conditions. The crystal has a hexagonal unit cell with lattice parameters a=0.3296 and c=0.52065 nm. In addition to normal sp^3 hybridized covalent bonding, ZnO has a substantial ionic bonding component which is a characteristic of iono-covalent materials.[31,32] The cubic zinc blende-type structure can be obtained by epitaxial growth of ZnO on suitable cubic substrates while the rock salt structure cannot be stabilized by epitaxial growth. Under compression at relatively high pressure of about 10 GPa, reduction of the lattice dimensions causes the interionic Coulomb interaction to favor the ionicity more over the covalent nature and wurtzite-type to rock salt-type transition is achieved.[33] Furthermore, calculations show that crystal structure of ZnO can be transformed from rock salt-type to CsCl-type at very high pressure of about 260 GPa.

As shown in figure 1, in wurtzite crystal structure hexagonal ions of zinc are surrounded by four counter oxygen ions situated at the corners of a tetrahedron and vice versa. The crystal structure can be described as a number of alternating planes composed of tetrahedrally coordinated O^{2-} and Zn^{2+} ions, stacked alternatively along the *c*-axis. Although the whole unit cell of ZnO is neutral, due to specific distribution of Zn^{2+} and O^{2-} determined by crystallography, some surfaces are terminated entirely with cations or anions. This results in positively or negatively charged surfaces, called polar surfaces. The most common polar surfaces are {0001}. The group of planes {01-11} is also polar in nature but are rarely observed except for some nanohelical structures.[22]

The alternate stacking of oppositely charged ions produce positively charged Zn-terminated (0001) and negatively charged O-terminated (000-1) polar surfaces. The anisotropic nature of the crystal is responsible for normal dipole moment, spontaneous polarization along the *c*-axis, and divergence in surface energy. Three fast growing faces {10-10}, {11-20}, and {0001} determine the growth habit thereby the shape of the ZnO nanostructures. The {0001} surfaces, having the highest surface energy of the low-index planes grow faster than the other stable surfaces. This anisotropic crystal growth leads to

faster crystal growth along the *c*-axis minimizing the {0001} surface area. The surface of a nanowire is composed of Zn-terminated, polar (0001) top surface and six nonpolar {10-10} or {11-20} facets. Typical morphology of a ZnO nanowire and corresponding crystal facets are shown in figure 2.
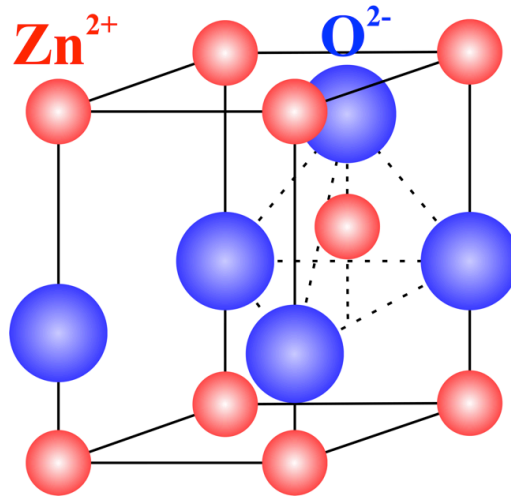
Figure 1: Wurtzite structure model of ZnO in which oxygen anions and Zn cations form a tetrahedral unit.
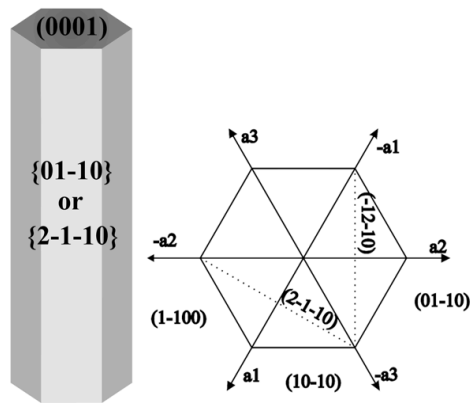
Figure 2: Typical growth morphology of ZnO nanowire and the corresponding facets.

2.1.3 Growth of ZnO Nanowires

ZnO nanowires are prepared using different techniques such as wet chemical routes,[3,4] vapor deposition methods,[7,34] metal–organic chemical vapor deposition (MOCVD),[35–37] molecular beam epitaxy (MBE),[38] pulsed laser deposition (PLD),[39,40] sputter deposition,[41] flux methods,[42] electrospinning,[43–45] and by etching ZnO films.[46]

13

Solution growth of ZnO nanowires is generally carried out by hydrolysis of zinc salts in alkaline medium and it is often referred to as chemical bath deposition (CBD) method, solvothermal method, or hydrothermal method when water is used as the medium for growth.

2.1.4 Hydrothermal Growth of ZnO Nanowires

Solution based techniques have unique advantages over other methods in many ways. The growth is carried out under relatively lower temperatures compared to physical vapor deposition methods. In hydrothermal route the temperature used ranges from 70 °C to 90 °C. Additionally low temperature processes help to avoid unwanted incorporation of impurities like catalysts in to the nanowires. Wide range of substrates e.g. silicon wafer, paper, or plastic are being used in solution based methods.[2,47–51] The compatibility with flexible organic substrates is advantageous in integration of the nanostructures in prospected ZnO nanowire-based foldable and portable electronic devices. There are no catalysts being used in hydrothermal method and the process is based on heterogeneous nucleation and oriented attachment on the seed layer. This ensures that all the nanowires in the array are in direct contact with the substrate surface and endow with a continuous pathway for carrier transport, an important advantage for electronic devices based on these materials.[52] Another advantage is that it can be combined with the well-developed lithographic techniques.[53] The cost of production is minimal for this technique compared to other methods due to the use of simpler equipments and cheaper chemicals. It uses less hazardous materials and is more environmental benign than other methods.

In hydrothermal growth of ZnO nanowires, a zinc salt is hydrolyzed to form ZnO. An alkaline solution is necessary for this reaction to occur since divalent metal ions normally do not hydrolyze in acidic medium. In general common alkali compounds like NaOH or KOH can be used for the growth.[54] But KOH is more preferred to NaOH, since K^+ ion has a larger radius and thus a lower chance of inclusion into the ZnO lattice.[54,55] Besides, Na^+ is attracted by the OH^- around the nanocrystal and forms a effective capping layer, thus inhibiting the growth.[52] Hexamethylenetetramine (HMTA, $(CH_2)_6N_4$) is the most commonly used alkali source for ZnO nanowire growth. It acts as a weak base and a pH buffer to facilitate ZnO growth. Slow and controlled release of OH^- ions is achieved by thermal decomposition of HMTA. The role of HMTA has been a topic of debate for a long time.[56–59] HMTA is a nonionic tertiary amine which can act as a bidentate ligand coordinating with two Zn^{2+} ions.[60] Some results argued that HMTA acts not only as OH^- source but aids anisotropic

14

growth by capping on to {10-10} surface.[56] But later with the help of XANES spectroscopy, it was shown that HMTA does not form a metal ion complex in solution.[57] Also it is revealed that HMTA helps the nanowire growth by keeping the crystallization of ZnO under thermodynamic control by the slow release of OH$^-$ ions.[58] The chemical reactions leading to ZnO growth can be simplified as given below.

$$(CH_2)_6N_4 + 6H_2O \quad \leftrightarrow \quad 6HCHO + 4NH_3 \qquad (1)$$

$$NH_3 + H_2O \quad \leftrightarrow \quad NH_4^+ + OH^- \qquad (2)$$

$$Zn^{2+} + 4NH_3 \quad \leftrightarrow \quad [Zn(NH_3)_4]^{2+} \qquad (3)$$

$$Zn^{2+} + 2OH^- \quad \leftrightarrow \quad Zn(OH)_2 \qquad (4)$$

$$Zn(OH)_2 \quad \leftrightarrow \quad ZnO + 2H_2O \qquad (5)$$

In growth solution HMTA readily hydrolyzes producing formaldehyde and ammonia (equation 1). This reaction is due to releasing the strain associated with its molecular structure. Ammonia combines with water to produce hydroxyl ions (equation 2) which is used for the formation of $Zn(OH)_2$ (equation 4). It also coordinates with Zn^{2+} and thus stabilizes aqueous zinc ions (equation 3). When heated, $Zn(OH)_2$ produces ZnO by dehydration (equation 5). But the combination of Zn^{2+} with OH$^-$ does not necessarily produce $Zn(OH)_2$. There can be other intermediates like $[Zn(OH)_4]^{2-}$, $[Zn(OH)]^+$ etc. formed which eventually undergo dehydration as $Zn(OH)_2$ does. Besides heating, dehydration of $Zn(OH)_2$ can be achieved by microwave irradiation, ultrasonication, or even by sunlight.[61–63] All these chemical reactions are very slow and are in equilibrium. Therefore each step can be driven to both sides of the equilibrium by adjusting the concentration of precursors and the growth temperature.

In hydrothermal growth, water acts as a solvent and it helps the hydrolysis of HMTA to produce the alkaline environment that is required for the hydrolysis. The oxygen in the final ZnO is not from H_2O, it actually comes from the alkali.[52] But in general, when the basic environment is provided, water is not necessary for growth. Organic solvents like methanol, ethanol, or their mixture with water also can be used as the solvent for growth.[64–66] Other organic compounds such as trioctylamine can be used as both the solvent and the

15

alkali source.[67] A similar approach is described in *Chapter 5* where ethylene glycol is used as the solvent.

In 1990, Verges *et al.* reported a hydrothermal synthetic route for preparation of ZnO rods.[3] In that report, rod-like ZnO microcrystals were prepared by hydrolysis of zinc salts in the presence of HMTA. The novelty or peculiarity of the crystallization mechanism was not recognized at that time. It was only later, in 2002, Pacholski *et al.* reported a mechanism based on oriented attachment of quasi-spherical ZnO nanoparticle units.[68] The necks formed between the attached units were later filled up and smoothened by Ostwald ripening.

2.1.5 Seeded Growth of ZnO Nanowires

Seeded growth of ZnO nanowires is advantageous in integration of nanowires in sensors and energy harvesting devices. In general ZnO nanowires can be grown hydrothermally on any substrates, provided there is ZnO seed layer. Different substrates such as silicon wafers, polydimethylsiloxane (PDMS), thermoplastic polyurethanes, paper, organic fibers, and carbon fibers are chosen for this purpose.[2,47–51] Various methods have been adopted to prepare the seed film on solid support such as sputtering, thermal decomposition of zinc acetate precursors etc. It has been shown that the vertical alignment of nanowire array is poor when polycrystalline seed were used.[5,69]

2.2 Results and Discussion

Atomic layer deposition (ALD) was used to grow a uniform ZnO film with a thickness of 30 nm on Si substrates to serve as the seed layer for the subsequent growth. The as-deposited ZnO film presents no preferred orientation, which could be slightly improved by post-annealing at elevated temperatures (figure 3).
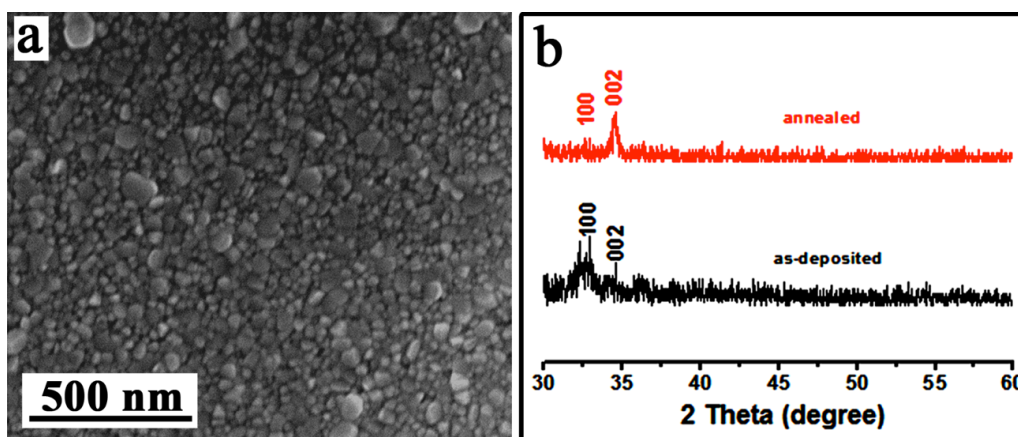
Figure 3: Nature of seed layer prepared by ALD. (a) SEM image of the surface morphology of the annealed ZnO film, not showing a highly oriented textured structure. (b) XRD patterns of 30 nm ZnO films by ALD deposition before and after annealing at 700 °C for 1 hour.

A silicon substrate with annealed seed layer (30 mm×5 mm) was put facing downward in a vial containing 15 mL, 12.5 mM equimolar solution of zinc nitrate and HMTA. The bottle was sealed and kept at 90 °C for 24 hours. As shown in figure 4, the resultant nanowire array contains nanowires with diameter of about 100 nm and with length of 4-5 µm. The SEM image given in the inset of figure 4a indicates that some tapering happens at the tips of the nanowires. As shown in the TEM image (figure 4c) the nanowires are single crystalline and show the axial growth proceeded in [0001] direction.
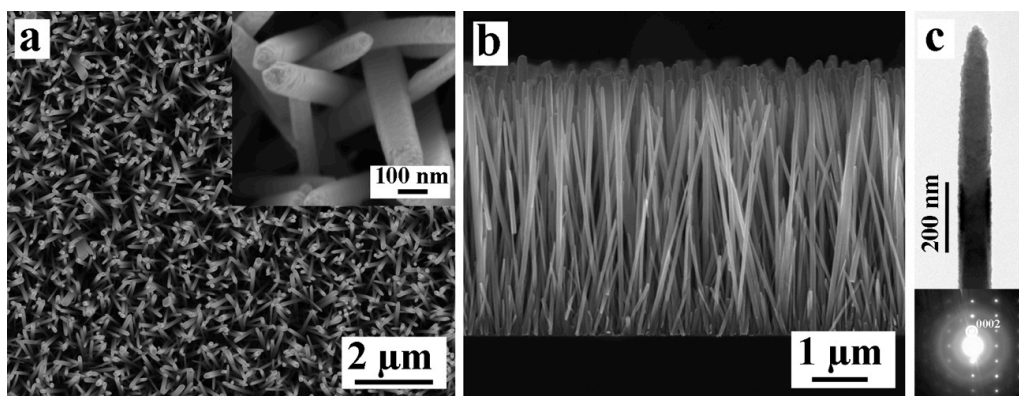
Figure 4: Morphology and structure of ZnO NWs grown by hydrothermal method. (a) SEM image of NW array. A magnified SEM image showing the tips of NWs is given in the inset. (b) SEM image of a cross section of NW array. (c) TEM image of a NW and corresponding ED pattern (inset).

The modality lies in the flexibility of this technique to grow nanowires in different types of surfaces. When combined with ALD, complex textured surfaces also can be used.[70] An example is shown in figure 5. A textured silicon surface is shown in figure 5a, which contains grooves of approximately a micron deep. This substrate is a leftover in the preparation of silicon tetrahedral particles by wet etching.[71] Seed layer of 30 nm ALD ZnO was deposited and the growth has been carried out in the same manner as described above. As given in the SEM images (figure 5b and 5c) the nanowires are formed all over the surface.
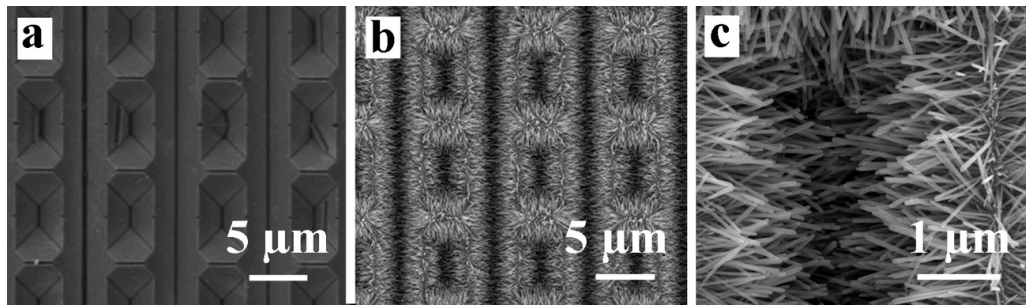
Figure 5: ZnO NWs grown on a textured silicon substrate. (a) SEM images of a textured silicon surface and (b) NWs grown after depositing ZnO seed layer. (c) A magnified SEM image of NW array

2.2.1 Patterned Growth of ZnO Nanowires

The density of nanowires on a substrate depends upon the number of heterogeneous nucleation taking place in the growth process. Other than reaction parameters, it can also be controlled using a non-continuous seed layer.[52] Here two types of seed layers are prepared and the subsequent growth of nanowires is demonstrated. One of them is an array of patterned holes prepared on a photoresist layer on top of a continuous ALD ZnO layer. The other one is patterned dots of ZnO on Si substrate. Initially a layer of continuous ZnO is deposited and then the photoresist is spin coated. Using phase-shift lithography, arrays of holes and patterned ZnO dots are generated as shown in the schematic illustration (figure 6a).

18
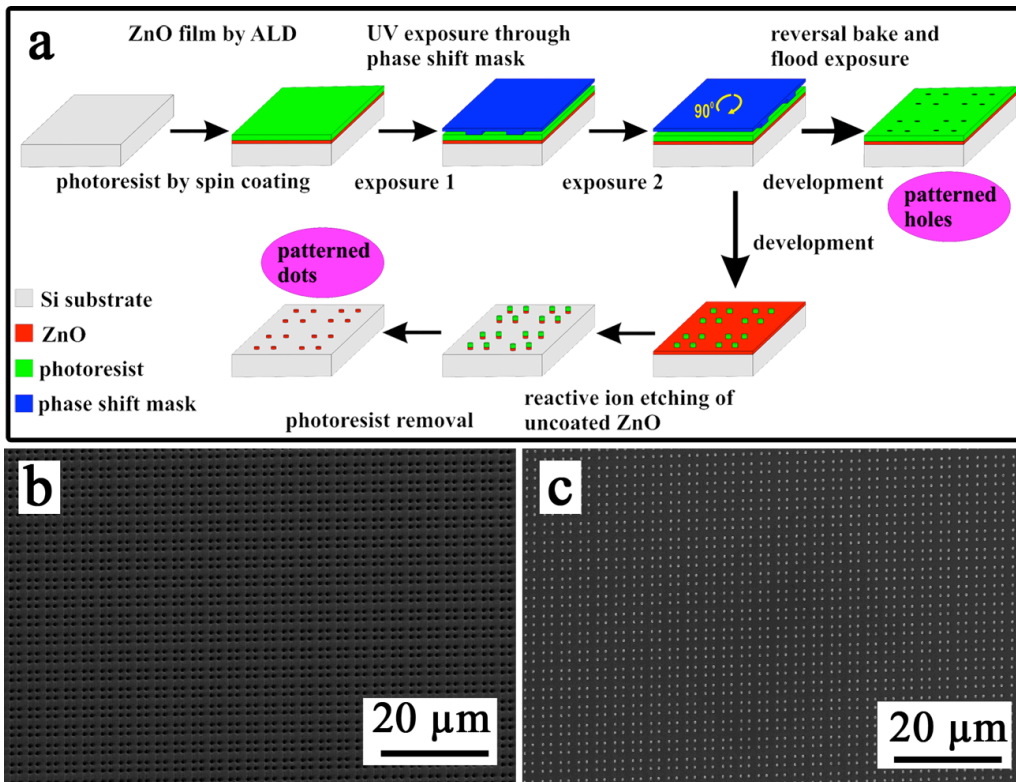
Figure 6: Fabrication of patterned ZnO seeds. (a) The scheme of fabrication of patterned ZnO holes and dots by near-field contact phase-shift photolithography. (b, c) SEM images of the patterned (b) holes and (c) dots that show perfect periodic order over a large area.

The holes prepared are of outer diameter ~750 nm (figure 7a) and the dots are of diameter ~400 nm (figure 7c). Note that the surface of each dot is smooth. Each area exposed does not act as a single seed but as a cluster of nucleation sites and many nanowires are grown from each hole/dot (figure 7b, 7d). In both cases, this process did not alter the polycrystalline nature and poor orientation of the seeds. However the density of nanowires formed can be controlled.

Figure 7: ZnO NWs grown on non-continuous seed layers. (a) SEM images of ALD ZnO layer covered with a photoresist layer with patterned holes and (b) NW array grown using this as the seed. (c) SEM image of patterned dots. A zoom in is given in the inset. (d) SEM image of NW array grown using patterned dots as the seed.

2.2.2 Nature of Growth of ZnO Nanowires

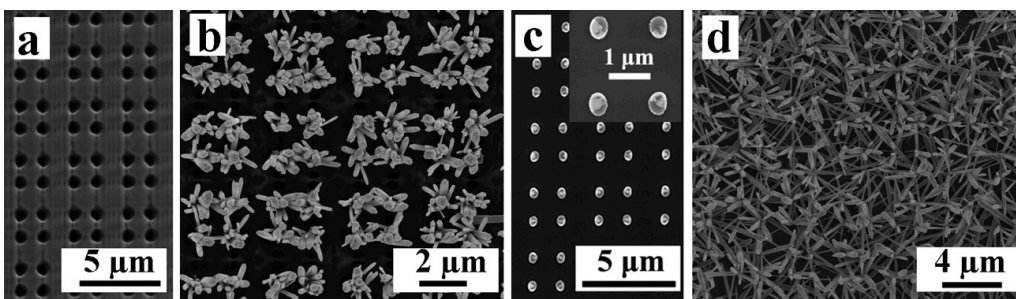The nature of growth of ZnO nanowires is influenced by different factors such as concentration of the precursors, size of the seed, and the reaction temperature. To understand this, a typical growth condition is chosen with 15 mL of 12.5 mM precursor solution. The size of the seed is selected to be 30 mm×5 mm and the temperature is set at 90 °C. Different sample bottles are prepared with the same concentration, volume of precursors, and size of the seed. All samples are kept in oven set at 90 °C. At different time intervals the samples are removed from the oven, substrates are taken out, cooled down and the morphologies of samples were observed (figure 8).

Based on the morphology of samples the growth of ZnO nanowires in hydrothermal method can be generally divided in to three phases. In the initial phase (1-3 hours) multiple nucleations and rapid growth take place. The nanowires grow in length and radius. In the second phase (3-12 hours) the growth rate is reduced. But all nanowires are of hexagonal prismatic structure and the tips are well faceted. In the third phase (12-24 hours) the growth is minimal but the tips of nanowires shows some tapering.
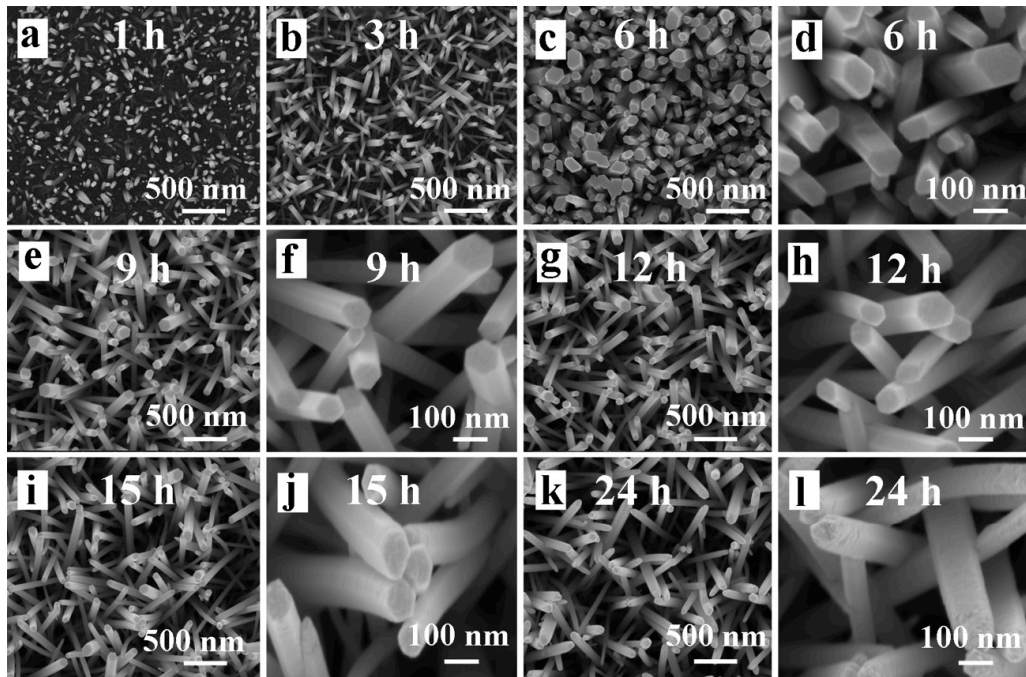
Figure 8: Nature of hydrothermal growth of ZnO NWs. SEM images of NW arrays prepared using different time of growth *viz* (a) 1 h, (b) 3 h, (c, d) 6 h, (e, f) 9 h, (g, h) 12 h, (i, j) 15 h, and (k, l) 24 h. Close views of the tips of NWs after different time intervals are shown in (d, f, h, j, l).

Furthermore the growth solution is examined for concentration of soluble zinc species using atomic absorption spectrometer (AAS). Prior to the AAS measurement, each growth solution was centrifuged at 4000 rpm for 10 min in order to remove the possible precipitates. The relation between the concentration of zinc ions in the solution and time exhibits the same nature as described above (figure 9). In the first phase, rapid decrease in concentration of zinc ions is observed. This is associated with numerous nucleation and rapid growth of ZnO crystals. In addition to heterogeneous nucleation, certainly there is homogenous nucleation and subsequent growth, which consumes Zn^{2+}. In the second phase the growth of crystals slowed down due to the decrease in concentarion of Zn^{2+}. As the concentration of Zn^{2+} decreases further, the dissolution-reprecipitation mechanism dominates over natural growth (third phase). The tapering of tips can be therefore ascribed to dissolution-reprecipitaion phenomenon that dominates in the third phase.
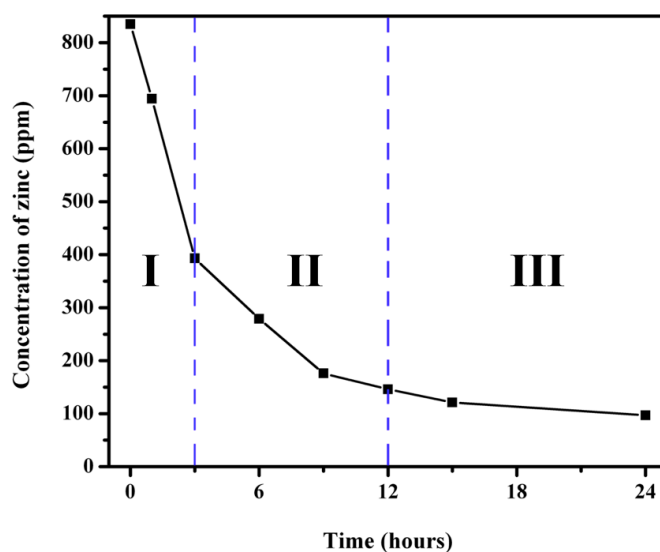
Figure 9: Relation between the overall Zn concentration in the growth solution and the reaction time. Different growth phases are marked with I, II, and III.

In general, in a growth system, provided no precursors are replenished, rapid growth happens initially. Due to depletion of Zn^{2+} ions the growth of the ZnO nanowires usually slowed down with time and eventually arrived at dissolution-reprecipitation equilibrium for longer reaction times. This is again clear from the morphology of nanowires when the concentration of the precursors is doubled and the time of growth was kept unchanged. As shown in the SEM image (figure 10), the tips of the nanowires are well faceted. This shows that the system is still in growth phase, apparently phase II, even after 24 hours.
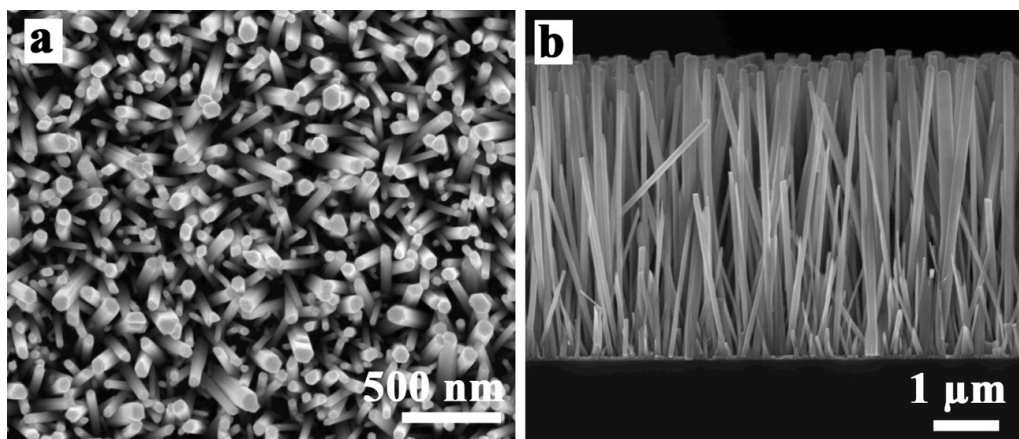
Figure 10: Morphology of NW array when the concentrations of the precursors are doubled (25 mM). SEM images of NW array (a) top view and (b) cross-sectional view.

2.3 Summary

ZnO is a multifunctional group II-VI compound semiconductor. ZnO nanowires are widely studied for their potential applications in various fields of electronics and optics. Hydrothermal seeded growth has advantages in terms of purity and crystallinity of the fabricated ZnO nanowires and simplicity of the process. It is an environmentally benign process and can be scaled up which makes it suitable for fabrication of components commercially. The use of seed layer prepared by ALD helps to grow nanowires on planar and textured substrates. The density of nanowires in an array can be controlled using a non-continuous seed layer. Although the growth is influenced by the concentration of the precursors and temperature, general morphology of ZnO nanowires remains unchanged. The nature of tips of nanowires can be altered by adjusting the growth time or concentration. But for a rational change in morphology, e.g. to prepare hierarchical or radial heterostructures, this will not be enough. Hydrothermal synthesis of ZnO nanostructure generally uses a relatively low temperature and mild reaction conditions. This opens up the possibility of addition of a large variety of chemicals including structure-directing agents for fabrication of modified functional structures, which will be discussed in the next chapters.

2.4 References

[1]   C. Lieber, P. Yang, *US Pat. 5,897,945* **1999**, *67*, 1.

[2]   L. E. Greene, M. Law, J. Goldberger, F. Kim, J. C. Johnson, Y. Zhang, R. J. Saykally, P. Yang, *Angew. Chem.* **2003**, *42*, 3031.

[3]   M. Vergés, A. Mifsud, C. Serna, *J. Chem. Soc. Faraday Trans.* **1990**, *86*, 959.

[4]   L. Vayssieres, K. Keis, *J. Phys. Chem. B* **2001**, *28*, 3350.

[5]   L. Vayssieres, *Adv. Mater.* **2003**, *15*, 464.

[6]   Z. W. Pan, Z. R. Dai, Z. L. Wang, *Science* **2001**, *291*, 1947.

[7]   B. D. Yao, Y. F. Chan, N. Wang, *Appl. Phys. Lett.* **2002**, *81*, 757.

[8]   H. Yan, R. He, J. Pham, P. Yang, *Adv. Mater.* **2003**, *15*, 402.

[9]   J. Lao, J. Wen, Z. Ren, *Nano Lett.* **2002**, *2*, 1287.

[10]   B. Li, Y. Wang, *J. Phys. Chem. C* **2010**, *114*, 890.

[11]   Q. Wu, X. Chen, P. Zhang, Y. Han, X. Chen, Y. Yan, S. Li, *Cryst. Growth Des.* **2008**, *8*, 3010.

[12]   S. Ko, D. Lee, H. Kang, K. Nam, J. Yeo, *Nano Lett.* **2011**, *11*, 666.

[13]   J. Y. Lao, J. Y. Huang, D. Z. Wang, Z. F. Ren, *Nano Lett.* **2003**, *3*, 235.

[14]   S. a Morin, M. J. Bierman, J. Tong, S. Jin, *Science* **2010**, *328*, 476.

[15]   Y. J. Xing, Z. H. Xi, X. D. Zhang, J. H. Song, R. M. Wang, J. Xu, Z. Q. Xue, D. P. Yu, *Solid State Commun.* **2004**, *129*, 671.

[16]   S. Konar, Z. R. Tian, *J. Phys. Chem. B* **2006**, *110*, 4054.

[17]   F. Xiang, D. Jianning, Y. Ningyi, L. Kuntang, W. Xiuqin, W. Shuyong, *Curr. Nanosci.* **2013**, *9*, 341.

[18]   J.-H. Park, H.-J. Choi, Y.-J. Choi, S.-H. Sohn, J.-G. Park, *J. Mater. Chem.* **2004**, *14*, 35.

[19]   G. Wei, W. Qin, L. Ning, R. Kim, G. Wang, D. Zhang, P. Zhu, K. Zheng, L. Wang, *J. Nanosci. Nanotechnol.* **2010**, *10*, 2065.

[20]   Z. L. Wang, X. Y. Kong, Y. Ding, P. Gao, W. L. Hughes, R. Yang, Y. Zhang, *Adv. Funct. Mater.* **2004**, *14*, 943.

[21]   P. X. Gao, Z. L. Wang, *Appl. Phys. Lett.* **2004**, *84*, 2883.

[22] R. Yang, Y. Ding, Z. Wang, *Nano Lett.* **2004**, *4*, 1309.

[23] X. Kong, Z. Wang, *Nano Lett.* **2003**, *3*, 1625.

[24] M. H. Huang, S. Mao, H. Feick, H. Yan, Y. Wu, H. Kind, E. Weber, R. Russo, P. Yang, *Science* **2001**, *292*, 1897.

[25] A. McLaren, T. Valdes-Solis, G. Li, S. C. Tsang, *J. Am. Chem. Soc.* **2009**, *131*, 12540.

[26] M. Grätzel, *Nature* **2001**, *414*, 338.

[27] M. Law, L. E. Greene, J. C. Johnson, R. Saykally, P. Yang, *Nat. Mater.* **2005**, *4*, 455.

[28] F. Patolsky, C. Lieber, *Mater. today* **2005**, *8*, 20.

[29] Z. L. Wang, J. Song, *Science* **2006**, *312*, 242.

[30] W. Liang, B. D. Yuhas, P. Yang, *Nano Lett.* **2009**, *9*, 892.

[31] U. Özgür, Y. I. Alivov, C. Liu, a. Teke, M. a. Reshchikov, S. Doğan, V. Avrutin, S.-J. Cho, H. Morkoç, *J. Appl. Phys.* **2005**, *98*, 041301.

[32] C. Klingshirn, *ChemPhysChem* **2007**, *8*, 782.

[33] S. Desgreniers, *Phys. Rev. B* **1998**, *58*, 14102.

[34] M. Huang, Y. Wu, H. Feick, N. Tran, *Adv. Mater.* **2001**, *13*, 113.

[35] W. Park, G. Yi, M. Kim, S. Pennycook, *Adv. Mater.* **2002**, 1841.

[36] W. I. Park, D. H. Kim, S.-W. Jung, G.-C. Yi, *Appl. Phys. Lett.* **2002**, *80*, 4232.

[37] H. Yuan, Y. Zhang, *J. Cryst. Growth* **2004**, *263*, 119.

[38] Y. W. Heo, V. Varadarajan, M. Kaufman, K. Kim, D. P. Norton, F. Ren, P. H. Fleming, *Appl. Phys. Lett.* **2002**, *81*, 3046.

[39] Y. Sun, G. M. Fuge, M. N. R. Ashfold, *Chem. Phys. Lett.* **2004**, *396*, 21.

[40] J.-I. Hong, J. Bae, Z. L. Wang, R. L. Snyder, *Nanotechnology* **2009**, *20*, 085609.

[41] W.-T. Chiou, W.-Y. Wu, J.-M. Ting, *Diam. Relat. Mater.* **2003**, *12*, 1841.

[42] C. Xu, G. Xu, Y. Liu, G. Wang, *Solid State Commun.* **2002**, *122*, 175.

[43] D. Lin, W. Pan, H. Wu, *J. Am. Ceram. Soc.* **2007**, *90*, 71.

[44] D. D. Lin, H. Wu, W. Pan, *Adv. Mater.* **2007**, *19*, 3968.

[45] X. M. Sui, C. L. Shao, Y. C. Liu, *Appl. Phys. Lett.* **2005**, *87*, 113115.

[46] J.-J. Wu, H.-I. Wen, C.-H. Tseng, S.-C. Liu, *Adv. Funct. Mater.* **2004**, *14*, 806.

[47] T.-Y. Liu, H.-C. Liao, C.-C. Lin, S.-H. Hu, S.-Y. Chen, *Langmuir* **2006**, *22*, 5804.

[48] Y. Qin, X. Wang, Z. L. Wang, *Nature* **2008**, *451*, 809.

[49] J. Bae, M. K. Song, Y. J. Park, J. M. Kim, M. Liu, Z. L. Wang, *Angew. Chem.* **2011**, *50*, 1683.

[50] J. Na, B. Gong, G. Scarel, G. Parsons, *ACS Nano* **2009**, *3*, 3191.

[51] A. Manekkathodi, M.-Y. Lu, C. W. Wang, L.-J. Chen, *Adv. Mater.* **2010**, *22*, 4059.

[52] S. Xu, Z. L. Wang, *Nano Res.* **2011**, *4*, 1013.

[53] R. Kozhummal, Y. Yang, F. Güder, A. Hartel, X. Lu, U. M. Küçükbayrak, A. Mateo-Alonso, M. Elwenspoek, M. Zacharias, *ACS Nano* **2012**, *6*, 7133.

[54] L. N. Demianets, D. V. Kostomarov, I. P. Kuz'mina, S. V. Pushko, *Crystallogr. Reports* **2002**, *47*, S86.

[55] L. Demianets, D. Kostomarov, *Ann. Chim. Sci. Mat.* **2001**, *26*, 193.

[56] A. Sugunan, H. C. Warad, M. Boman, J. Dutta, *J. Sol-Gel Sci. Technol.* **2006**, *39*, 49.

[57] K. M. McPeak, M. a. Becker, N. G. Britton, H. Majidi, B. a. Bunker, J. B. Baxter, *Chem. Mater.* **2010**, *22*, 6162.

[58] K. M. McPeak, T. P. Le, N. G. Britton, Z. S. Nickolov, Y. a Elabd, J. B. Baxter, *Langmuir* **2011**, *27*, 3672.

[59] K. Govender, D. S. Boyle, P. B. Kenway, P. O. Brien, *J. Mater. Chem.* **2004**, 2575.

[60] I. S. Ahuja, C. L. Yadava, R. Singh, *J. Mol. Struct.* **1982**, *81*, 229.

[61] S.-H. Jung, E. Oh, K.-H. Lee, W. Park, S.-H. Jeong, *Adv. Mater.* **2007**, *19*, 749.

[62] L. Shi, K. Bao, J. Cao, Y. Qian, *Cryst. Eng. Comm.* **2009**, *11*, 2009.

[63] H. E. Unalan, P. Hiralal, N. Rupesinghe, S. Dalal, W. I. Milne, G. a J. Amaratunga, *Nanotechnology* **2008**, *19*, 255608.

[64] B. Liu, H. C. Zeng, *J. Am. Chem. Soc.* **2003**, *125*, 4430.

[65] B. Cheng, E. T. Samulski, *Chem. Commun.* **2004**, 986.

[66] J. Zhang, L. Sun, J. Yin, H. Su, C. Liao, C. Yan, *Chem. Mater.* **2002**, *14*, 4172.

[67] B. D. Yuhas, D. O. Zitoun, P. J. Pauzauskie, R. He, P. Yang, *Angew. Chem.* **2006**, *118*, 434.

[68]   C. Pacholski, A. Kornowski, H. Weller, *Angew. Chem.* **2002**, *41*, 1188.

[69]   D. S. Boyle, K. Govender, P. O'Brien, *Chem. Commun.* **2002**, 80.

[70]   D. Tian, X. Zhang, Y. Tian, Y. Wu, X. Wang, J. Zhai, L. Jiang, *J. Mater. Chem.* **2012**, *22*, 19652.

[71]   J. W. Berenschot, N. R. Tas, H. V. Jansen, M. Elwenspoek, *Nanotechnology* **2009**, *20*, 475302.

3 Controlled Radial Growth of ZnO Nanowires

In this chapter a novel, environmental benign method to modify seeded growth of ZnO nanowires using a capping agent, polyethylene glycol (PEG) is demonstrated. It is achieved by inhibition of axial growth of ZnO and consequential enhancement of radial growth. The capping occurs at the polar surface during the growth and it amplifies the radial growth; eventually becomes hexabranched nanorods. The evolution of such structures and possible growth mechanism are discussed in detail. Fabrication of ZnO structures with large surface area especially polar surfaces makes this method attractive. The method is successfully used in modifying nanowires by secondary growth without altering the single crystallinity of the nanowires. Hexabranched ZnO structures show better catalytic activity when they are used for photocatalytic degradation of organic dyes.

3.1 Introduction

Tailoring the morphology of ZnO nanostructures especially, fabrication of oriented hierarchical nanostructures gained much attention over the last decade.[1–5] In comparison with normal ZnO nanowires, ZnO nanostructures with a larger surface area, for instance, branched nanowires are more attractive in the application fields of catalysis, sensing, dye-sensitized solar cells *etc*.[1–4,6–11]

There are many parameters governing the hydrothermal growth of ZnO nanowires like concentration of precursors, temperature, time of growth *etc*. Even the rate of heating may have some effect on the final structures. Bimodal distribution of aspect ratio was observed when very low concentration of precursors (0.33mM) and long reaction time (48 hours) were used.[12] In that system, layer-by-layer growth of ZnO compete with self-perpetuating dislocation growth which dominates toward depletion of precursors. A similar approach using long reaction time was used to prepare nanoscrews and discs.[13] This was based on dissolution-repreciptation process that is again dominant toward the lower degree of supersaturation. Thus initially formed faceted nanowires were transformed into nanoscrews and discs. The length of nanowires can be increased either by adding additional zinc salt solution,[14] or by replenishing the growth solution.[15–17]

3.1.1 Structure Directing Agents in Hydrothermal Growth of ZnO Nanowires

Controlling the morphology by adjusting the reaction parameters is limited in many aspects. For fabrication of nanowires with more complex morphologies, including hierarchical structures or structures with increased polar/nonpolar surface area, these methods are not sufficient. In this regard structure-directing agents are widely used in the synthesis of ZnO nanostructures. Long nanowires are prepared by addition of polyetheleneimine (PEI) which selectively gets capped on the nonpolar surface of ZnO and promotes axial growth.[18,19] ZnO microparticles with a diversity of well-defined morphologies, including rod-like, nut-like, and rice-like structures have been obtained when sodium dodecyl sulfate (SDS) and triethanolamine (TEA) were added.[20] Nearly spherical ZnO nanoparticles and twinned hexagonal plates were obtained in presence of dissolved gelatin.[21] In this case gelatin acts as a nucleating template in the mineralization process of ZnO. ZnO nanoparticles were also synthesized using a new bio-friendly method, at near-neutral pH and 37 °C using a tris(hydroxymethyl)aminomethane-assisted route.[22] Here the tris(alcohol)aminomethane acts both as a buffer and a polydentate binding agent to the zinc oxide limiting its crystal growth.

Flowerlike cupped-end ZnO microrod bundles were obtained when hydrazine hydrate was added with zinc salt and ammonia in the starting precursor solution.[23] Hydrazine was also used to prepare ZnO nanosheets in an ordered array.[24] When trisodium citrate was added to the precursors interconnected sheetlike ZnO nanostructures were formed.[25] The influence of similar additives such as citrates, oxalates, and tartrates have been used mainly for the preparation of structures with large surface area by inhibiting the axial growth.[1,2,26,27] Control over the crystallization and the size distribution of ZnO was achieved by using poly(ethylene oxide-block-methacrylic acid) (PEO-block-PMAA) copolymer.[28] Here PMAA block acts as an anchoring block, which prevents the axial growth while PEO block, as solution block inducing steric hindrance to avoid agglomeration. In a similar study, poly(ethylene oxide-block-styrene sulfonic acid) (P(EO-b-SSH)) has also been used.[29,30] ZnO nanorings were prepared by the addition of polyacrylamide (PAM).[31] Different morphologies such as flowerlike, disklike, and dumbbell-like ZnO microcrystals of hexagonal phase have been obtained using ammonia, citric acid (CA), and poly(vinyl alcohol) (PVA), respectively as the capping molecules.[32]

The influence of potassium chloride, ammonium fluoride (NH_4F), ammonium acetate (CH_3COONH_4), and ethylenediamine (EDA) on the final morphology were also investigated for electrodeposition of ZnO.[33] It was revealed that Cl^- or acetate anions (($CH_3COO)^-$) adsorbs preferentially onto the (0001) facet to produce platelet-like crystals whereas needlelike structures were obtained by addition of EDA or NH_4F.

As a wurtzite-structured metal oxide, ZnO crystal is composed of positively-charged Zn (0001) and negatively-charged O (000-1) planes which results in divergence in surface energy among the facets.[34] ZnO crystals have propensity to grow along the *c*-axis direction of the hexagonal wurtzite structure. This characteristic has been utilized in modification of ZnO nanowires *via* wet chemical approaches like capping. As described above, wide range of capping agents has been used for this process. In general they fall into two categories; cationic and anionic. The effectiveness of these capping agents also depends on the pH of the reaction mixture which can change the surface polarity of the nanowires.[35] As the (0001) surface carries positive charge, cationic capping agents adhere to the nonpolar surface and enhance the growth in *c*-direction and thus produces long nanowires.[16,18,36] On the other hand, anionic species get capped at the polar, zinc terminated, hexagonal faces and makes the growth at this surface difficult and promote radial growth.[1,2,26,27,37] But when anionic capping agents such as citrates and tartrates were used, the structures grew upward to a

considerable extend and finally became tower-like structures. ZnO grows radially to a less extend giving rough side surfaces. When the capping is not effective, it often leads to step formation and ultimately results in tower-like structures.[1,2,27] The possibility of using capping agents utilizing the coordination abilities hasn't been adequately intrigued for this purpose.
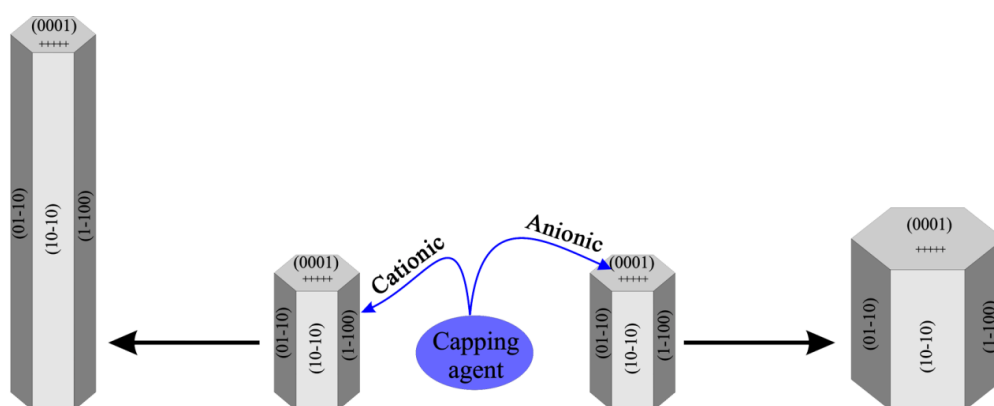

Figure 1: Effect of capping agents on the growth of ZnO nanowires. Schematic illustration showing the mechanism of anionic and cationic capping agents.

3.1.2 Hierarchical ZnO Structures

Hierarchical structures are particularly interesting for their large surface area, which is advantageous in surface related applications such as catalysis and sensing. Recently solution-grown ZnO nanowire arrays have been exploited in dye-sensitized solar cells (DSSCs) as an efficient photoanode alternative to traditional TiO_2 nanoparticle films.[8,19,35,38,39] However, the insufficient surface area of simple 1D ZnO nanostructures is unprofitable for high dye loading and light harvesting, which yet restricted the energy conversion efficiency to relatively low levels.[19] This limitation has been partly overcome by constructing DSSCs using ZnO nanowires with branched structures as photoanodes, which significantly improved the DSSC power conversion efficiency due to a greatly increased surface area.[8,38] However, so far the branched ZnO nanowires achieved by either one-step or multistep growth always present a boundary at the branch/stem interface due to nonepitaxial growth. This is supposed to generate an additional bottleneck for DSSC efficiency due to the amplified charge recombination during boundary percolation.[8,38,40–44]

In view of the above facts, a single-crystalline ZnO branched nanostructure is practically beneficial for photovoltaic applications owing to its high loading ability without sacrificing efficient electron transport. In this work, a versatile homoepitaxial solution synthesis strategy for seeded growth of single-crystalline ZnO hexabranched nanowires by selecting polyethylene glycol (PEG) as the capping agent is demonstrated.

3.2 Results and Discussion

3.2.1 Hexabranched Nanorods

To serve as the seed layer for the subsequent growth, atomic layer deposition (ALD) was used to grow a uniform ZnO film with a thickness of 30 nm on Si substrates. The substrate with the seed layer (30 mm × 5 mm) was put facing downward into a 15 mL growth solution containing 12.5 mM zinc nitrate and 12.5 mM hexamethylenetetramine (HMTA) with the addition of 1 mL PEG (Mw 400) in the starting solution and then maintained at 90 °C for 24 hours.

As described in *Chapter 2*, the same process without PEG resulted in ZnO nanowires. But when PEG is added, by the same procedure, it yielded nanorods with a star-like morphology (hexabranched nanorods) (figure 2a). As shown in figure 2b, the height of the formed nanostructures was significantly reduced to 500 nm in presence of PEG in the growth solution. Same reaction conditions without PEG, yielded nanowires of about 80 nm diameter and 3.5 μm length. XRD patterns in figure 2c confirmed the formation of phase-pure hexagonal wurtzite ZnO nanostructures in both the samples. It is known that growth of ZnO along the [0001] direction (*c*-axis) is thermodynamically favored.[45] When ZnO nanowires started to grow from the non-highly oriented seeds, a small amount of initial nanowires which were not aligned normal to the substrate were quickly impeded by neighboring crystals. Most vertical nanowires were easy to survive through competition and continued to grow, eventually forming [0001]-oriented arrays. As shown in figure 2b, there is only limited axial growth taking place, which could not completely overcome the underlying seed orientation. Thus, a relatively poor [0001]-orientation was presented.

The TEM image in figure 2d shows an individual ZnO nanowire and its related SAED pattern. The nanowire is single-crystalline and elongating along the inherent fast growth direction [0001] of ZnO. The nanorod presented in figure 2e follows the same *c*-oriented growth habit. Although the nanorod has a rough surface with an unusual edge contrast under

electron beam, it presents good single crystallinity. In addition, its diameter gradually declines from top to bottom. The configuration of six symmetric branches grown from a stem was clearly shown (figure 2f) when the nanorods located on the (0001)-basal plane. The extension direction of each branch corresponds to each *m*-orientation of six {10-10} axes symmetrically distributed in the ZnO (0001) foil plane.
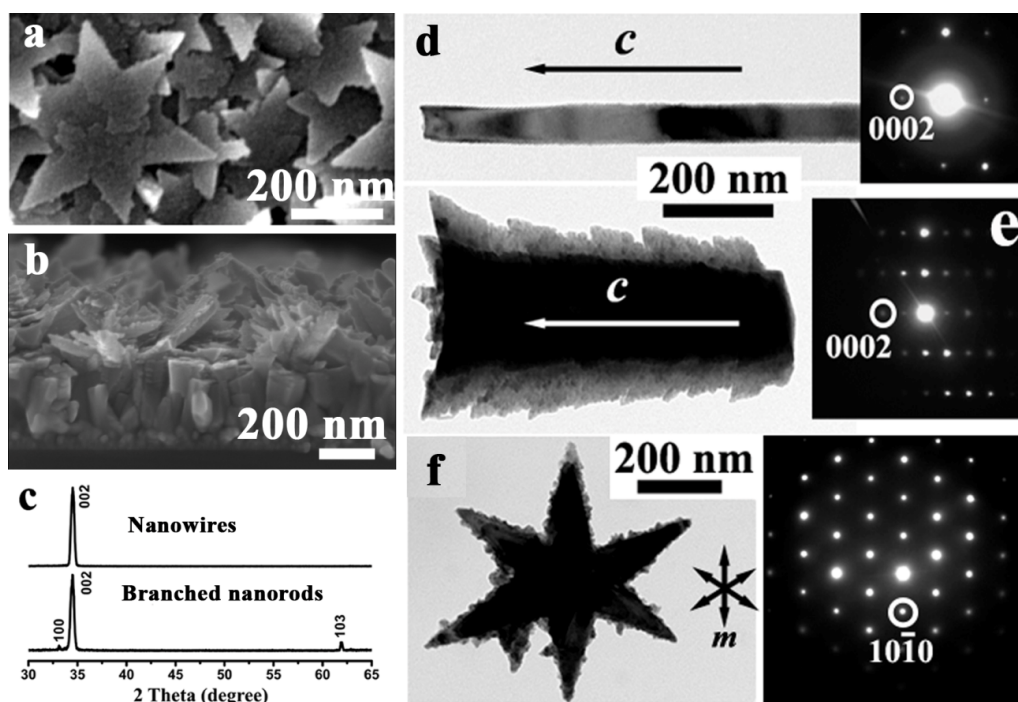

Figure 2: Morphology of hexabranched nanostructures. (a) SEM image of ZnO branched nanorods. (b) Cross-sectional SEM image of branched nanorods. (c) XRD patterns of NWs and branched nanorods. (d, e) TEM images together with their SAED patterns of individual NWs and branched nanorods with the same magnification. (f) TEM image of a branched nanorod showing six distinct branches and their orientation.

A similar evolution mode dominates even for the ZnO bipod crystals unavoidably precipitated in the bulk growth solution, in contrast to the reported cases.[41–43]. These crystals are formed by the fusion and stacking of neighboring ZnO blocks conforms with a star-like morphology (figure 3a and 3b), It is also seen that large ZnO crystals formed in bulk solution from 15 mL growth solution containing 3.125 mM zinc nitrate and 3.125 mM HMTA with the addition of 1 mL PEG (figure 3c). Due to the very low concentrations of the reactants, no visible seeded growth happened in this case. The ZnO crystals formed in bulk solution by homogeneous nucleation are smaller than the sample related to figure 3a. However, the

crystal evolution mode is similar. Under the same reaction conditions, fractal and tapered nanotrees were formed when the concentrations of zinc nitrate and HMTA in the nutrient solution were synchronously halved (6.25 mM) while the PEG amount was maintained the same (figure 3d). Inversely, drastic increase of the PEG amount while the reactant concentrations remained unchanged induced the formation of thinner and flatter structures like nanoplates and nanoslices (figure 3e and 3f). The above findings strongly hinted that the PEG is probably a previously 'underestimated' structure-directing agent, which is practically versatile for the geometric regulation of the solution-grown ZnO nanostructures. Therefore, the specific role of PEG in the seeded growth of ZnO will be revisited.
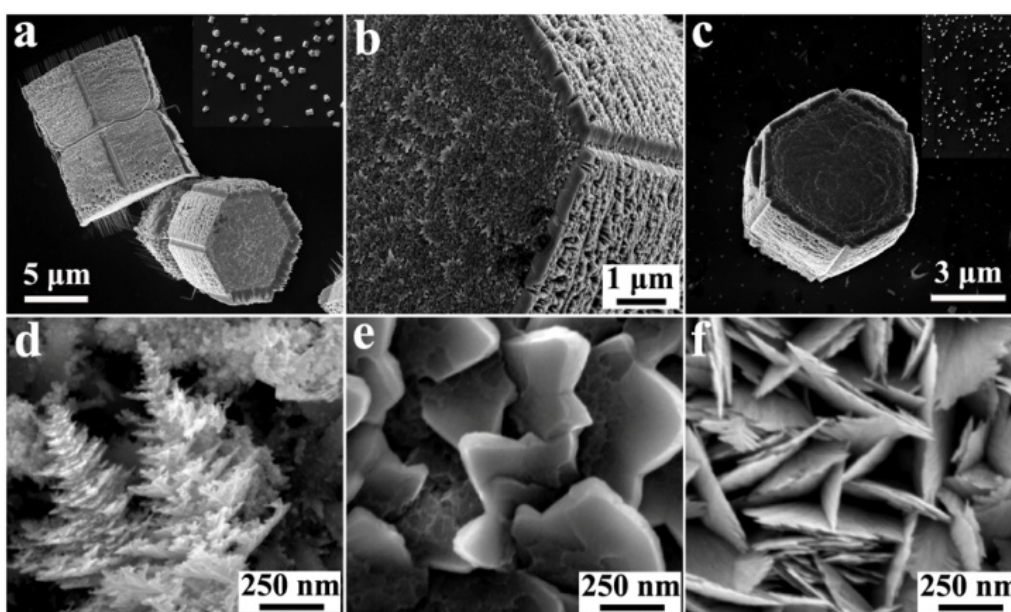
Figure 3. (a) SEM image of large ZnO crystals formed in bulk solution. (b) Zoomed SEM image on one crystal top surface, showing the stripes formed along the prismatic edges. Star-like patterns can be seen on the top surface. (c) SEM image of large ZnO crystals formed in bulk solution when 3.125 mM solution of precursors and 1 mL PEG were used. (d) SEM image showing morphology of fractal and tapered nanotrees grown from the seeds when 6.25 mM solution of precursors and 1 mL PEG were used. (e) SEM image showing morphology of nanoplates grown from the seeds when 12.5 mM solution of precursors and 2 mL PEG were used (f) SEM image showing morphology of nanoslices grown from the seeds when 12.5 mM solution of precursors and 4 mL PEG were used.

3.2.2 Growth Mechanism of Hexabranched ZnO Nanorods

PEG (Mw 400) is a common short-chain polymer with -(CH$_2$-CH$_2$-O)- repeating units. Previously, it was found that PEG could be exploited as a *c*-orientation crystal growth inhibitor only to selectively promote the formation of ZnO nanowires or nanorods in solution due to the coordination abilities of its oxygen atoms with zinc ions.[46] However, for the PEG-assisted ZnO growth based on the heterogeneous nucleation from the seeds, the single-crystalline hexabranched polymorph was first realized.

For better understanding how the single-crystalline ZnO hexabranched nanorods developed under the assistance of PEG, a time-dependent synthetic study was conducted. In order to maximally weaken the influence of steric hindrance on the structure evolution, patterned ZnO dots were used as the seeds instead of the continuous ZnO film. By using a non-continuous seed layer the density of nanorods formed are reduced so that the change in morphology at different growth levels can be observed. Patterned ZnO dots were generated by a modified phase shift photolithography technique as described in *Chapter 2*.[25]

Figure 4a-4h shows the PEG-assisted evolution of ZnO from the patterned dot arrays at selected time intervals *viz.* 1 h, 9 h, 12 h and 24 h. In all the stages, the emergence of diverse nanostructures was exclusively centered at each dot, persisting with the initial periodicity. After the growth for 1 h (figure 4a and 4b), multiple nucleation sites came out from each polycrystalline dot. Up to 9 h (figure 4c and 4d), the growth occurred both axially and laterally leaving thick hexagonally prismatic structures. In all these structures axial stripes can be detected along all the six prism edges. A longer reaction time until 12 h resulted in negligible growth along both the directions (figure 4e and 4f). But the structures have an apparent 18-sided shape with a flat top surface. The stripes observed in the previous phase have been changed into deeper axial grooves that separate six outspread branches. At a later reaction stage from 12 to 24 h, the branches elongated, sharpened and slightly upturned at the tips, leading to the formation of hexabranched nanostructures with a six-angle-star-like cross-section, as shown in figure 4g and 4h. Note that the diameter of most ZnO nanostructures formed in the later stages shrank from the top toward the nucleation sites (figure 4g and 4h).

Based on the above observations, a possible growth mode for the ZnO hexabranched nanostructures is proposed. A graphical illustration is also presented in figure 4i. At the initial stage, tiny ZnO nuclei with faceted surfaces were grown from the seeds by competitive

nucleation. The Zn^{2+} terminated (0001) surface was specifically capped by PEG *via* coordination with oxygen atoms, which suppressed the growth of ZnO on this thermodynamically preferred surface. Initially, the precursor in the solution was abundant and the growth occurred axially (*c*-axis) in a low rate together with the enhanced lateral growth. Thick hexagonal prismatic structures were thus produced. With the gradual depletion of Zn^{2+} ions in a prolonged reaction process, the growth of ZnO slowed down and got close to the growth–dissolution equilibrium.[26] Because the fast etching (0001)-plane of ZnO was efficiently capped by PEG, the six prismatic edges intersecting adjacent *m*-planes together with the six top edges became the most unstable fronts. The dissolution of ZnO on the edges was faster than its reprecipitation, which initiated six axial etched stripes and gradually deepened them. In contrast, the prism faces as the growth fronts continued to extend and branched epitaxially along the six *m*-axes. As the reaction further proceeded, increasingly limited supply of the reactant precursor ended the branches with tips.[27]
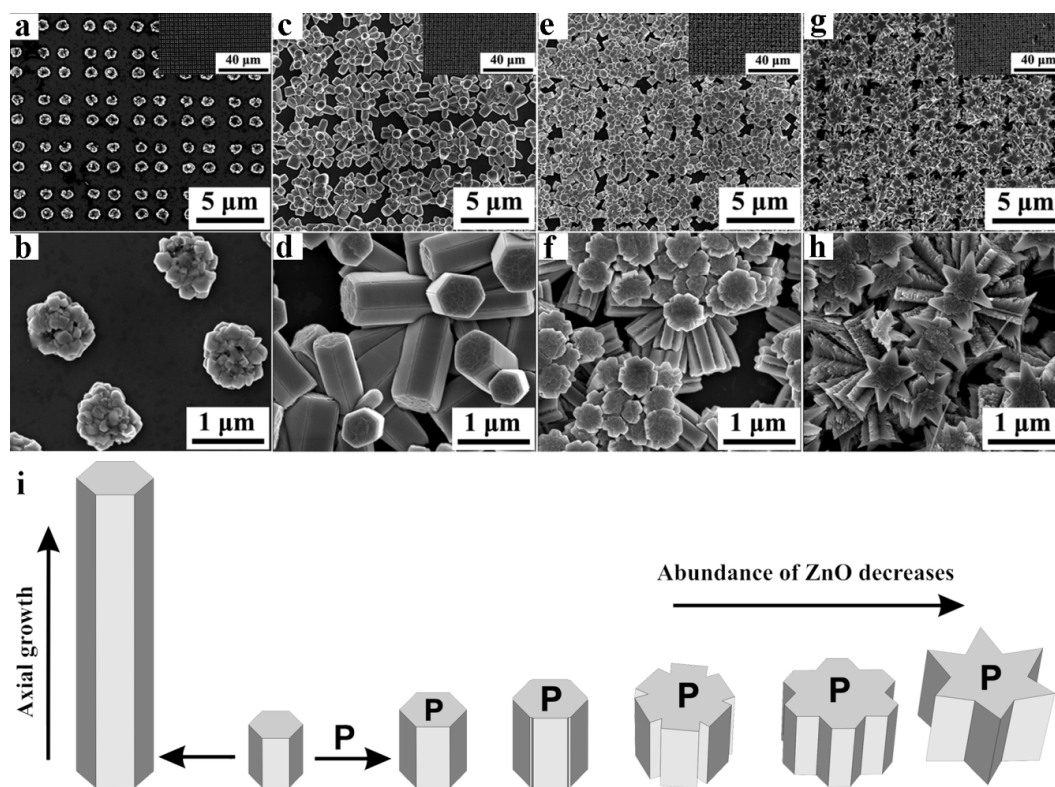

Figure 4. SEM images of the time-dependent morphological evolution of ZnO nanostructures grown from the seed arrays in presence of 1 mL PEG: (a, b) 1 h; (c, d) 9 h; (e, f) 12 h; (g, h) 24 h. Each inset in (a), (c), (e), and (g) shows a corresponding general view. (i) Pictorial

representation of the mechanism for the formation of single-crystalline ZnO hexabranched nanostructures. PEG is represented as P in the scheme.

For confirming the branching mechanism proposed above, the actual concentrations of overall soluble Zn species (simplified as Zn ions) in the growth solution during different reaction stages were measured by atomic absorption spectrometer (AAS). Here, continuous ZnO films were used as the seed layer. All the other reaction parameters followed the standard setup in our experiments. By analyzing the AAS result (red curve) shown in figure 5, it can be seen that the concentration of Zn ions in the growth solution reduced significantly from 800 to 340 ppm during the initial 6 h for the ZnO-forming reaction. In this stage, heterogeneous nucleation of ZnO on the seeded substrate was favorable because the existing seeds bypassed the nucleation step.[17] On condition that the supersaturation of ZnO clusters maintained in the solution, ZnO nanorods could form and continue to develop by anisotropic growth, though the growth along *c*-orientation was severely restricted due to the presence of PEG. Within the next 6 h, the depletion of Zn ions started to slow down. Accordingly, the growth rate of ZnO nanorods also reduced. Afterward, the concentration of Zn ions was only decreased from 150 to 110 ppm up to 12 h till the end of the reaction. Therefore, only a slight depletion of Zn ions occurred during the latter 12 h, which confirmed that the system herein was in a state close to a dynamic equilibrium while the branching of ZnO nanowires happened in this time window. The above AAS results provided a crucial support for the proposed dissolution–reprecipitation mechanism that is responsible for the formation of ZnO hexabranched nanostructures. For comparison, the time-dependent change of the Zn concentration for the seeded solution growth without PEG is also given in figure 5 (black curve). The change of the Zn concentration over time was almost similar in both the cases. Therefore, the depletion of Zn ions subject to the ZnO-forming reaction was hardly influenced by the addition of PEG (1 mL) in the system. This result presented an additional evidence for the non-acidic feature and weak reactivity of PEG in this solution reaction system.
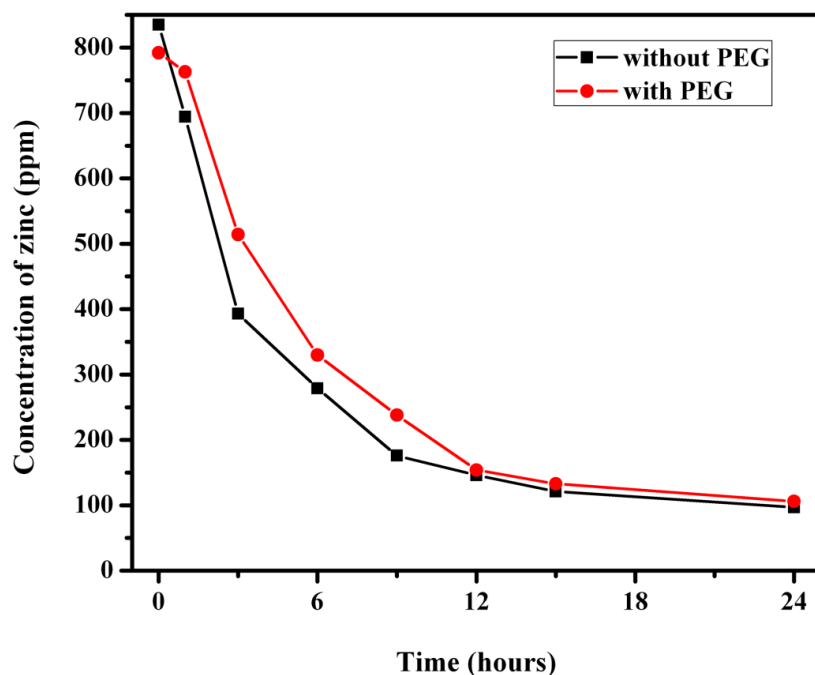
Figure 5. Relation between the overall Zn concentration in the growth solution and the reaction time with and without PEG. Prior to the AAS measurement, each growth solution was centrifuged at 4000 rpm for 10 min for removing the possible precipitates.

Regarding the *c*-axis inhibitors, anionic citrate has been most popularly used to tune the aspect ratio of ZnO nanostructures.[1,2,41–43] Recently various metal complex ions also demonstrated efficient control on the morphology of ZnO nanostructures by face-selective electrostatic adsorption.[35] However, neither of the strategies has been found applicable for the branched nanostructure formation. It can be considered that the distribution of species responsible for the capping in the ionic inhibitors is extremely sensitive to the solution environment. Especially, the significantly decreased pH value accompanied by the limited precursor supply could convert the capping agents to invalid forms. For this reason, the layered ZnO nanostructures in the citrate-assisted process were still tapered along the *c*-axis enduring a longer reaction time.[1,27] When more citrate ions were added, a porous structure with no alignment was formed due to the dissolution of ZnO,[27] most possibly induced by the strong hydrolysis of concentrated citrate ions near the end of the reaction. Therefore, the formation of the branched nanostructures is greatly beneficial from the nonionic, non- protic and weak-reactive features of PEG, which represents a more versatile structure-directing agent for ZnO solution growth.

40

3.2.3 Controlled Secondary Radial Growth

Furthermore the PEG-assisted approach for secondary growth using ZnO nanowires as the seeds was investigated. During the PEG-assisted secondary growth, the length and diameter of the evolving nanowires were investigated at different time intervals within 24 h (figure 6).

Figure 6: Cross-sectional SEM images showing the time-dependent morphological evolution of ZnO nanowires grown from the nanowire seed arrays by secondary growth in presence of 1 mL PEG: (a) original; (b) 1 h; (c) 6 h; (d) 9 h; (e) 12 h; (f) 24 h.

The relations of the average length and diameter as a function of the growth time were plotted in figure 7. It is clear that the nanowires hardly grew along [0001] direction with the *c*-axis inhibitor PEG, while the lateral growth was favored, continuing throughout the secondary growth.

Figure 7: Change in average length (red) and diameter (black) of ZnO nanowires as a function of the growth time by the PEG-assisted secondary growth.

In contrast, when the secondary growth was conducted in the nutrient solution without PEG, the initial ZnO nanowires gradually grew along the *c*-direction. After 6 hours of growth they show an increase less than 1µm and no visible change in diameter (figure 8).
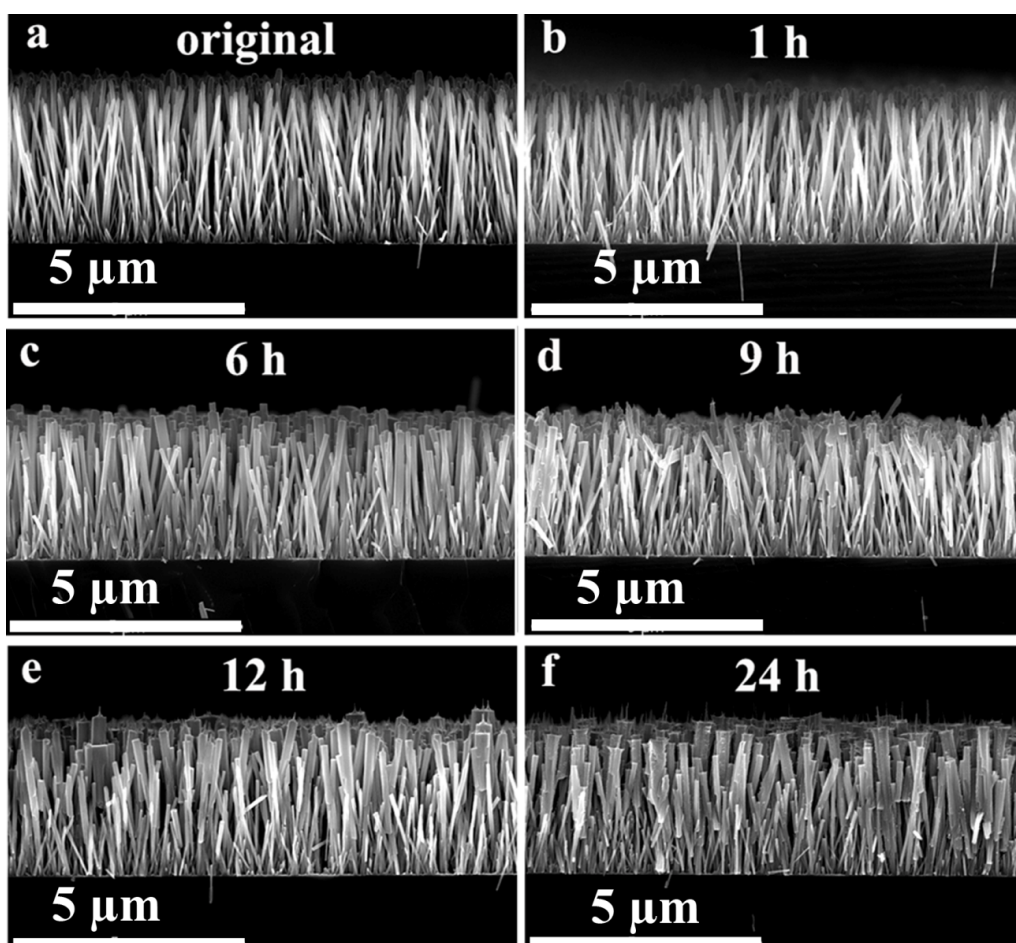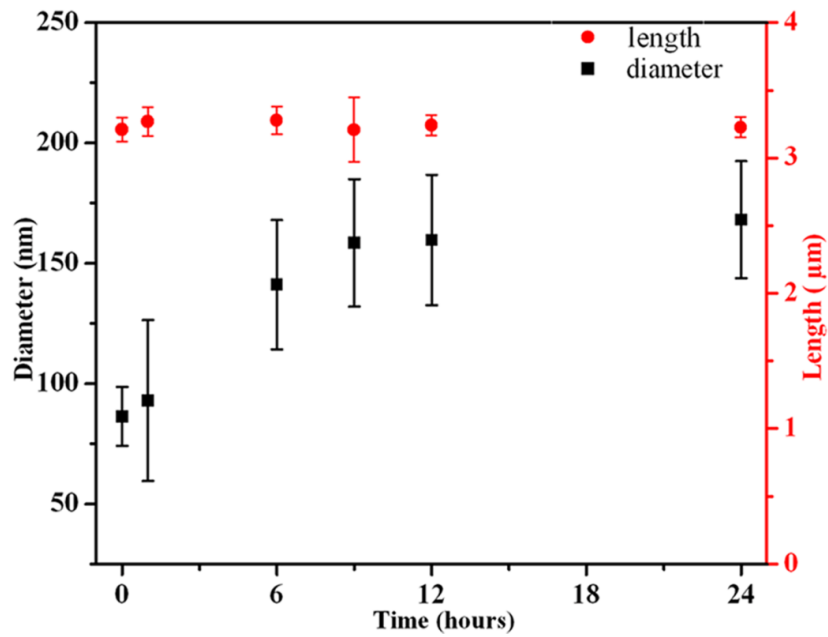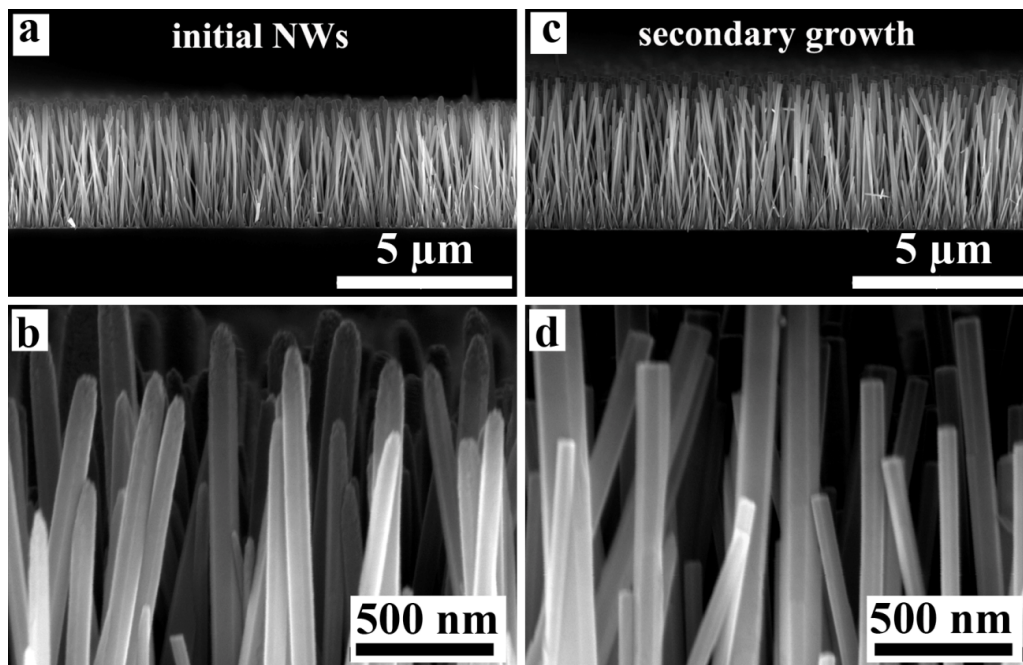
Figure 8: Cross-sectional SEM images showing the morphological evolution of ZnO nanowires grown from the nanowire seed arrays by secondary growth without PEG: (a) General view of original nanowires and (b) close view; (c) General view of nanowires after secondary growth and (d) close view.

For the PEG-assisted secondary growth, there are two important stages worth a special mention. Compared with the seed nanowires, the ZnO nanowires by secondary growth up to 6 h are much thicker and more hexagonal faceted (figure 9a and 9c). The unidirectional lateral growth mode governed by PEG indeed provides a potential solution route for achieving purposely doped homoepitaxial ZnO coaxial nanowires. This can be used for selective incorporation of dopants into the regenerative shell, which will be discussed in *Chapter 4*. After 24 h of growth, single-crystalline hexabranched nanowires with a six-angle-star-like cross-section were obtained (figure 9b and 9d). Each nanowire is multilayered with a flat top surface and a uniform width from top to bottom. The free space between adjacent nucleation units in vertical nanowire seeds is much larger than those in the polycrystalline film and the patterned dots each consisting of multiple nuclei. Therefore, it is expected that the upturned star tips and the reverse pyramidal shape occurring in the former cases (figure 2) were caused by gradually restricted aqueous precursor diffusion toward the nucleus bottoms rather than the growth habit.

Structural analysis of the secondarily grown nanowire (6 h) using TEM, as shown in figure 9e-9g, reveals perfectly single crystalline structure. The TEM images (figure 9e and 9f) show the individual nanowires with smooth side facets and flat top surfaces. The HRTEM image (figure 9g) taken at the edge of a nanowire with the FFT pattern given in the inset confirms the single-crystallinity of the resultant structure. The observed double layer spacing of 0.52 nm agrees well with the ZnO wurtzite crystal structure.
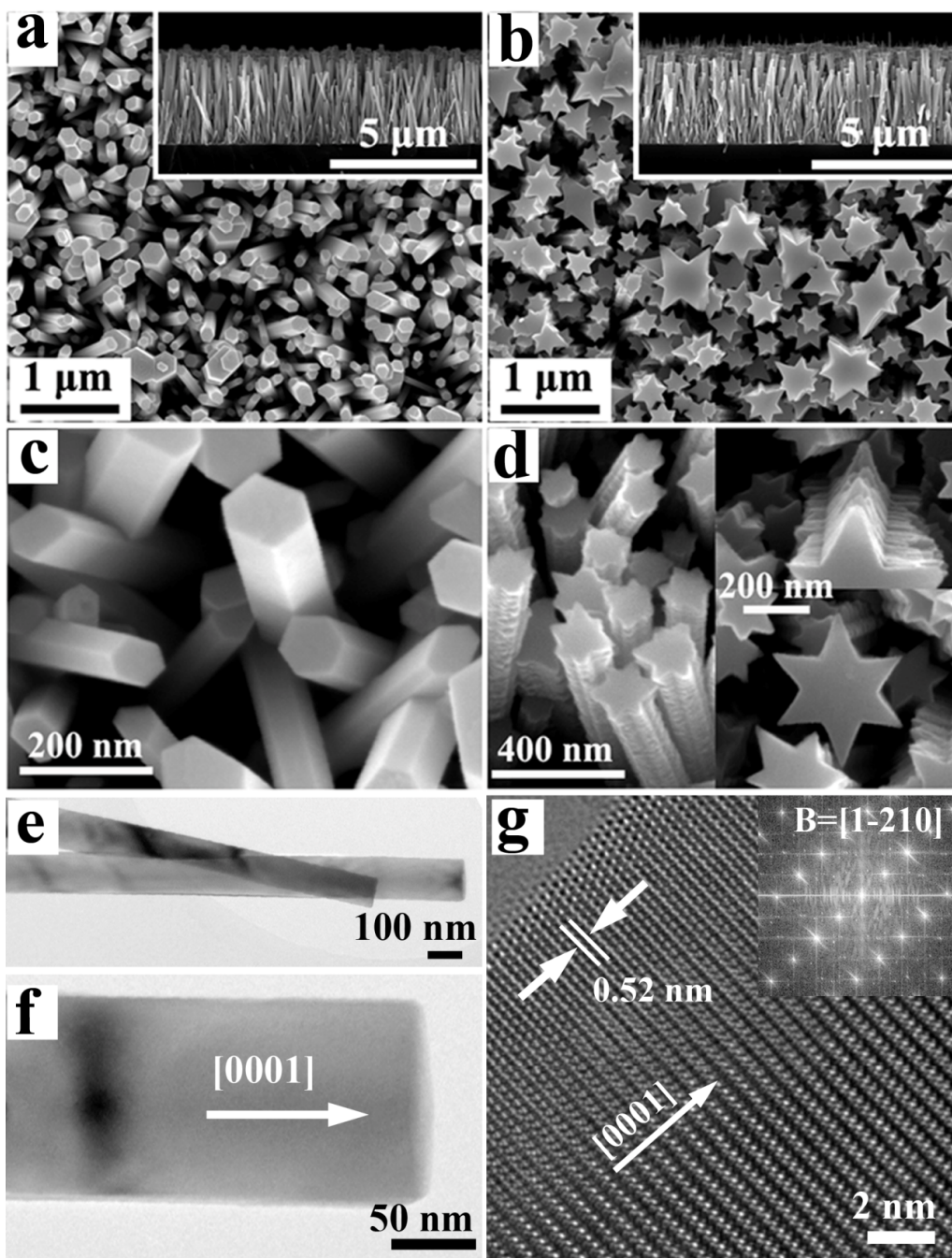
Figure 9: (a) SEM image of the morphologies of two important stages: (a, c) 6 h (b, d) 24 h. Inset in (a) and (b) show the corresponding cross-sectional SEM image of each sample. (e, f) Bright field TEM images of a NW after 6 h of PEG-assisted secondary growth. (g) HRTEM image and corresponding FFT pattern of the same sample.

By tuning the PEG amount or precursor concentrations or both, diverse hierarchical 1D ZnO nanostructures were obtained by the secondary growth (figure 10). Generally, increasing the PEG quantity for fixed precursor concentrations more efficiently inhibited the *c*-direction growth and benefited the branching. When the PEG amount was insufficient, long helical ZnO nanowires were finally grown along *c*-direction on the top of aligned ZnO hexabranched nanowires (figure 10a and 10b). When the excess PEG amount was added, the high viscosity of the nutrient solution would severely retard the aqueous diffusion of precursors deep into the nanowire seeds, which again led to a reverse pyramidal geometry of the epitaxial structures (figure 10c and 10d).

Figure 10: Top view (a) and cross-sectional view (b) of nanostructures grown from the nanowire seeds after secondary growth for 24 h at 90 °C using 0.5 mL PEG and 12.5 mM of precursor concentrations for both $Zn(NO_3)_2$ and HMTA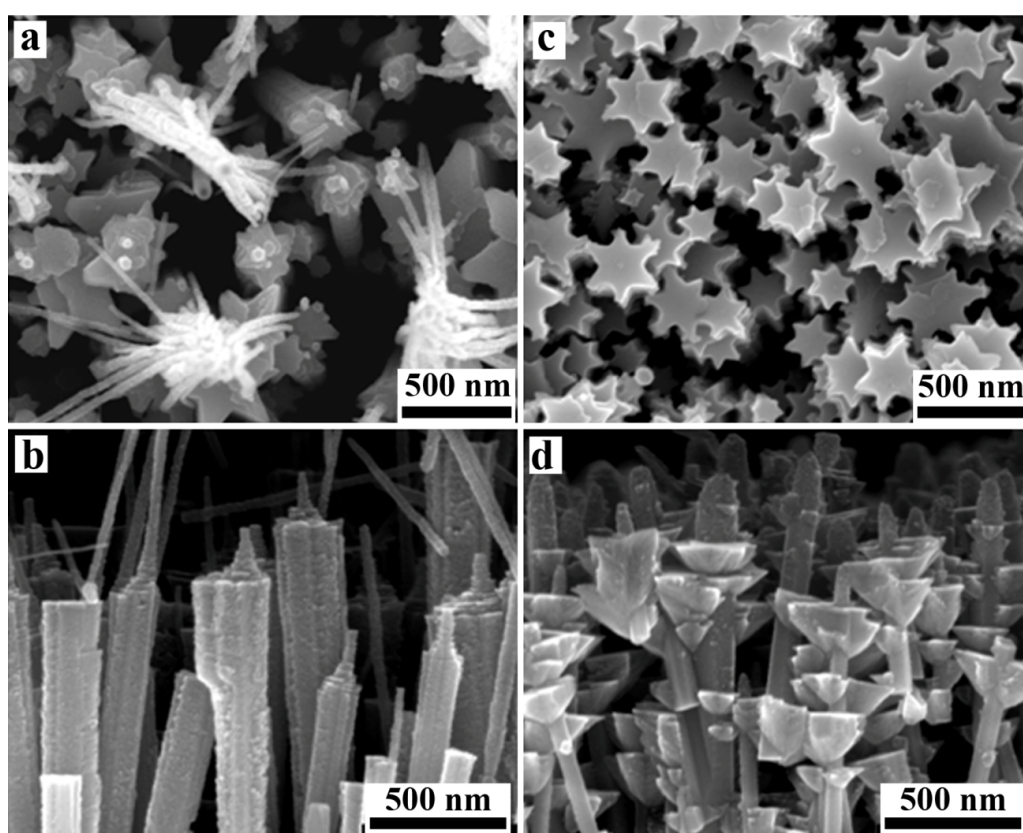; Top view (c) and cross-sectional view (d) of nanostructures grown from the nanowire seeds after secondary growth for 24 h at 90 °C using 4 mL PEG and 12.5 mM of precursor concentrations for both $Zn(NO_3)_2$ and HMTA.

The influence of concentration of precursors and amount of PEG on the morphology of secondarily grown ZnO nanowires is shown in figure 11. From the morphologies, it is suggested that 1~2 mL of PEG is the optimal window for the formation of uniform hexabranched nanowires in the current experimental setup.
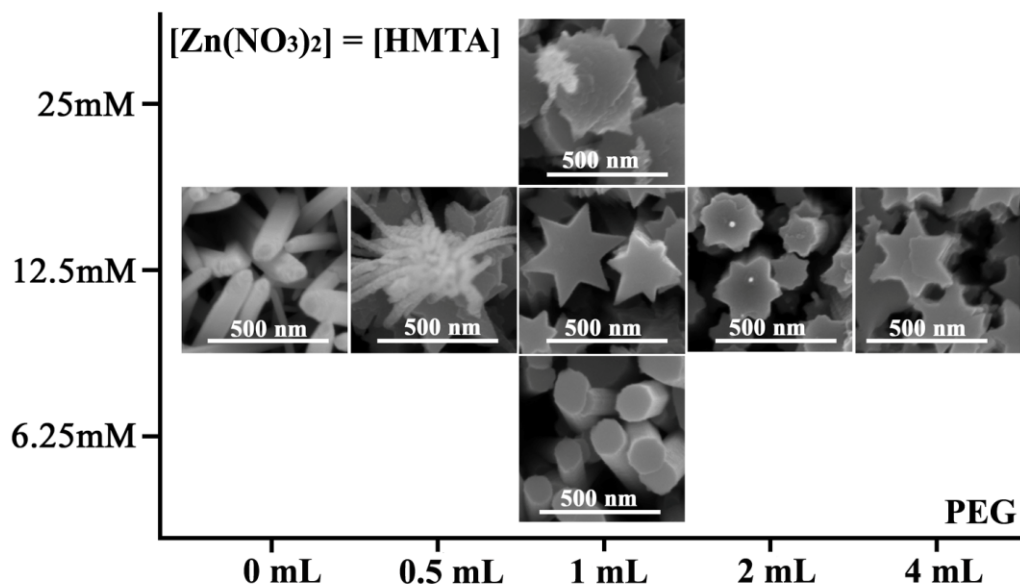
Figure 11: Morphology mapping of nanowire seeds after secondary growth for 24 h at 90 °C using different PEG amount and precursor concentrations.

Additionally the intersection angle and the extent of six branches could also be adjusted by varying the number, diameter or length of ZnO nanowires used as the seeds. Figure 12a and 12b shows SEM images of the ZnO hexabranched nanowires by secondary growth from a smaller piece of substrate containing solution-grown ZnO nanowire seeds with the same density. In contrast to the result presented in figure 9b, longer branches accompanied with reduced intersection angles between adjacent branches can be clearly observed. The decrease in the number of the ZnO nanowire seeds indeed increased the average amount of ZnO precipitates for each *m*-plane near the end of the reaction. So the branching could occur in a slower tapered fashion, leading to more developed branches. Inversely, if the number, average diameter or length of nanowires which serve as the seeds is increased, a short and undeveloped branched configuration can be expected due to the fast depletion of the limited ZnO precursors shared by excess *m*-plane areas.

Figure 12c shows an SEM image of the ZnO nanowires grown by chemical vapor deposition (CVD) method. Compared with the solution-grown ZnO nanowires, these nanowires are much thicker and longer. When these CVD-grown ZnO nanowires were used as the seeds for the secondary growth subject to 24 h in the presence of PEG, ZnO nanowires with increased diameters and immature branched configuration were finally produced (figure 12d), consistent with the postulation. This result also demonstrated that this PEG-assisted secondary growth process is compatible with primary ZnO nanowires produced by both solution and gas routes for achieving effective structural tuning.
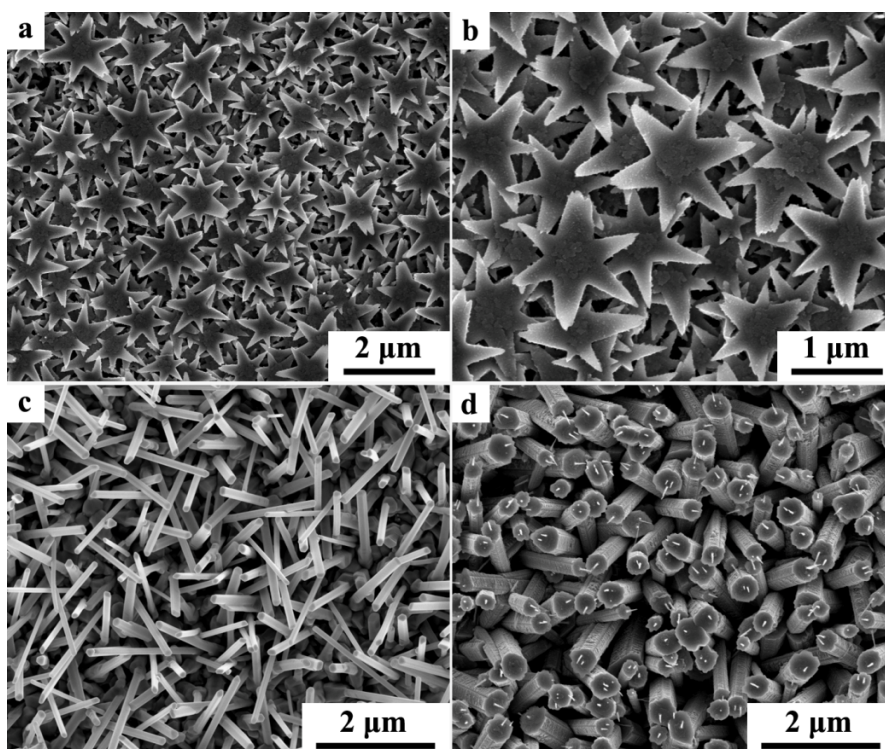
Figure 12: (a, b) SEM images of ZnO hexabranched nanowires after secondary growth using a piece of nanowire seeds with a smaller size. (c) SEM image of long ZnO nanowires grown by chemical vapor deposition. (d) SEM images of ZnO hexabranched nanowires after secondary growth using the sample in (c) as the seeds. A very short and undeveloped branched configuration is shown. For both the cases, the reaction was conducted at 90 °C for 24 h using 1 mL PEG and 12.5 mM of precursor concentrations for both $Zn(NO_3)_2$ and HMTA.

3.2.4 Photocatalytic Activity

ZnO has been known as photocatalyst displaying impressive applications in the photodegradation of some organic compounds.[47] To compare the photocatalytic activity of normal ZnO nanowires and ZnO branched nanostructures, photocatalyzed dye degradation experiments with organic dye methylene blue (MB) under ultraviolet light was conducted. Aqueous solution of MB (4mL, 2 µM) was separately prepared in 10 ml glass beakers. One sample solution was used as reference to measure the degradation without catalyst (Blank). Two dye solutions were separately added with a piece of normal ZnO nanowires catalyst (2 cm^2) and a piece of hexabranched nanorods catalyst (2 cm^2), both of which were grown from continuous ZnO film seeds. The above solutions were kept overnight in dark for establishing adsorption-desorption equilibrium. Then all the three MB solutions were exposed to a UV lamp with a wavelength of 254 nm and a power of 15 W. At each time interval the irradiation was paused and solution from each sample was taken out to quartz cuvettes for absorbance measurement using a UV-Vis spectrophotometer. After the measurement the solutions were returned to the beaker and the irradiation was resumed. As shown in figure 13, after exposure to UV light for 4 h, the ZnO branched nanorods were able to degrade 82% MB (green curve), whereas the normal ZnO nanowires degraded only 56% (red curve). The corresponding AAS results for these two samples (figure 5) have evidenced that the concentration changes of Zn ions in the growth solution with and without PEG followed a similar trend and rate, indicating the products of both the samples have a comparable amount. Moreover, when the morphologies of the nanowires and the branched nanorods samples are compared, the branched nanorods sample would show a 'negative' effect of the total ZnO volume regarding its much lower height if the volume difference still existed. Therefore, the contribution from a larger volume of the hexabranched nanorods sample to the enhanced MB degradation efficiency was excluded. ZnO hexabranched nanorods are of larger total surface area and polar surface compared to nanowires. Since the polar (0001) faces are of intrinsically highest energy, the higher photocatalytic activity could be attributed to the larger polar surface area or larger total surface area or their synergetic effect.

Furthermore, the photocatalytic activities of the ZnO hexabranched nanorods with the ZnO hexabranched nanowires *via* secondary growth of the normal nanowires are compared. As shown in figure 13 (blue curve), the ZnO branched nanowires by secondary growth degraded almost all the MB within 4 h, showing higher degradation efficiency. In contrast to the ZnO branched nanorods, the sample of ZnO branched nanowires by secondary growth has

a comparable (0001)-polar surface area, but a significantly enlarged total volume and total surface area. However, the enhancement of its dye degradation efficiency fell far behind this increase. Therefore, it is reasonable to suggest that the proportion of polar surfaces in the ZnO hexabranched nanostructures plays a major role in the enhancement of the degradation of organic pollutants.[47]
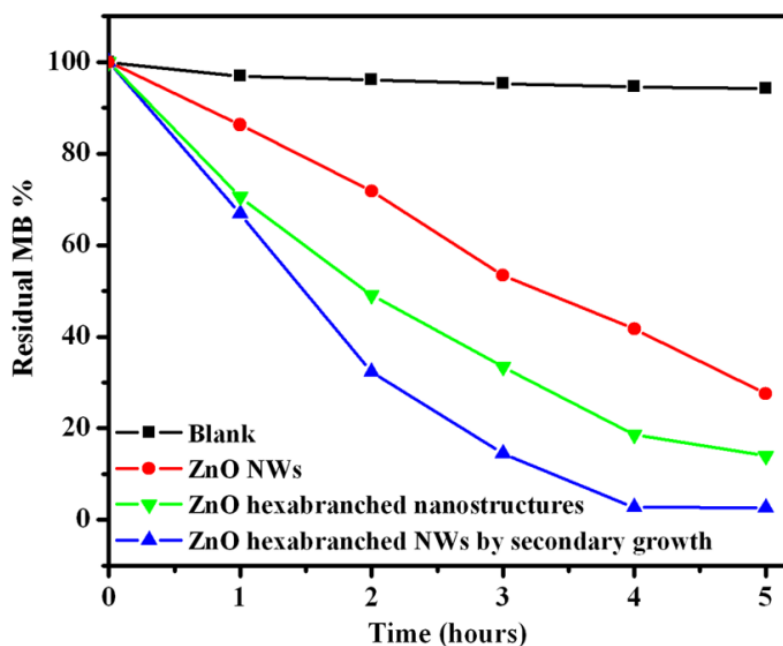
Figure 13: Degradation of MB photocatalyzed by normal ZnO nanowires, primary ZnO hexabranched nanorods, and secondarily-grown ZnO hexabranched nanowires under UV irradiation.

3.3 Summary

In summary, the polymer PEG was introduced as an efficient structure-directing agent for aqueous seeded growth of single-crystalline ZnO hexabranched nanowires. In the growth process the polymer acts as an effective capping agent that inhibits axial growth along *c*-direction thereby promotes the radial growth. This ends up in single crystalline ZnO hexabranched structures. This is a simple, controllable, and efficient method to increase the polar surface area of ZnO nanostructures. The generality of this PEG-assisted growth process using different ZnO seed layers including continuous film, patterned dots and vertically aligned nanowire arrays were investigated. All the obtained branched nanostructures are single crystalline in nature that is essentially determined by the homoepitaxial growth mode.

The single-crystalline hexabranched nanowires are of better photocatalytic activity compared to normal nanowires, which can be attributed to the increased total surface area/polar surface area. These structures are expected to find applications in various fields such as UV photocatalysts for organic pollutant degradation and photoanodes for DSSCs.

3.4 References

[1]   Z. R. Tian, J. A. Voigt, J. Liu, B. McKenzie, M. J. McDermott, M. A. Rodriguez, H. Konishi, H. Xu, *Nat. Mater.* **2003**, *2*, 821.

[2]   Z. R. Tian, J. a Voigt, J. Liu, B. McKenzie, M. J. McDermott, *J. Am. Chem. Soc.* **2002**, *124*, 12954.

[3]   B. Li, Y. Wang, *J. Phys. Chem. C* **2010**, *114*, 890.

[4]   Q. Wu, X. Chen, P. Zhang, Y. Han, X. Chen, Y. Yan, S. Li, *Cryst. Growth Des.* **2008**, *8*, 3010.

[5]   Y. J. Xing, Z. H. Xi, X. D. Zhang, J. H. Song, R. M. Wang, J. Xu, Z. Q. Xue, D. P. Yu, *Solid State Commun.* **2004**, *129*, 671.

[6]   J. Zhang, S. Wang, M. Xu, Y. Wang, B. Zhu, S. Zhang, W. Huang, S. Wu, *Cryst. Growth Des.* **2009**, *9*, 3532.

[7]   Y. Zhang, J. Xu, Q. Xiang, H. Li, Q. Pan, P. Xu, *J. Phys. Chem. C* **2009**, *113*, 3430.

[8]   S. Ko, D. Lee, H. Kang, K. Nam, J. Yeo, *Nano Lett.* **2011**, *11*, 666.

[9]   F. Xu, M. Dai, Y. Lu, L. Sun, *J. Phys. Chem. C* **2010**, *114*, 2776.

[10]   Y. Gao, M. Nagai, T. Chang, J. Shyue, *Cryst. Growth Des.* **2007**, 3.

[11]   J. X. Wang, C. M. L. Wu, W. S. Cheung, L. B. Luo, Z. B. He, G. D. Yuan, W. J. Zhang, C. S. Lee, S. T. Lee, *J. Phys. Chem. C* **2010**, *114*, 13157.

[12]   S. Cho, K.-H. Lee, *Cryst. Growth Des.* **2012**, *12*, 994.

[13]   S. Yin, T. Sato, *J. Mater. Chem.* **2005**, *15*, 4584.

[14]   B. Postels, H.-H. Wehmann, a Bakin, M. Kreye, D. Fuhrmann, J. Blaesing, a Hangleiter, a Krost, a Waag, *Nanotechnology* **2007**, *18*, 195602.

[15]   Y. Tak, K. Yong, *J. Phys. Chem. B* **2005**, *109*, 19263.

[16]   C. Xu, P. Shin, L. Cao, D. Gao, *J. Phys. Chem. C* **2010**, *114*, 125.

[17]   G. Hua, Y. Zhang, J. Zhang, X. Cao, W. Xu, L. Zhang, *Mater. Lett.* **2008**, *62*, 4109.

[18]   Y. Zhou, W. Wu, G. Hu, H. Wu, S. Cui, *Mater. Res. Bull.* **2008**, *43*, 2113.

[19]   M. Law, L. E. Greene, J. C. Johnson, R. Saykally, P. Yang, *Nat. Mater.* **2005**, *4*, 455.

[20]   P. Li, Y. Wei, H. Liu, X. Wang, *J. Solid State Chem.* **2005**, *178*, 855.

[21]   L. P. Bauermann, J. Bill, F. Aldinger, *Chem. Mater.* **2006**, *25*, 2016.

[22]   L. P. Bauermann, J. Bill, F. Aldinger, *J. Phys. Chem. B* **2006**, *110*, 5182.

[23]   C. Jiang, W. Zhang, G. Zou, W. Yu, Y. Qian, *J. Phys. Chem. B* **2005**, *109*, 1361.

[24]   S. Konar, Z. R. Tian, *J. Phys. Chem. B* **2006**, *110*, 4054.

[25]   C. Kuo, T. Kuo, M. H. Huang, *J. Phys. Chem. B* **2005**, 20115.

[26]   N. J. Nicholas, G. V Franks, W. a Ducker, *Langmuir* **2012**, *28*, 7189.

[27]   J. S. Bendall, G. Visimberga, M. Szachowicz, N. O. V. Plank, S. Romanov, C. M. Sotomayor-Torres, M. E. Welland, *J. Mater. Chem.* **2008**, *18*, 5259.

[28]   J. Norwig, W. H. Meyer, *Chem. Mater.* **1998**, *4756*, 460.

[29]   A. Taubert, G. Glasser, D. Palms, *Langmuir* **2002**, 4488.

[30]   A. Taubert, C. Ku, D. C. Martin, *J. Phys. Chem. B* **2003**, 2660.

[31]   Y. Peng, A.-W. Xu, B. Deng, M. Antonietti, H. Cölfen, *J. Phys. Chem. B* **2006**, *110*, 2988.

[32]   H. Zhang, D. Yang, D. Li, X. Ma, *Cryst. Growth Des.* **2005**, *5*, 547.

[33]   L. Xu, Y. Guo, Q. Liao, J. Zhang, D. Xu, *J. Phys. Chem. B* **2005**, *109*, 13519.

[34]   Z. L. Wang, *J. Phys. Condens. Matter* **2004**, *16*, R829.

[35]   J. Joo, B. Y. Chow, M. Prakash, E. S. Boyden, J. M. Jacobson, *Nat. Mater.* **2011**, *10*, 596.

[36]   L. Chen, Y. Yin, *Cryst. Growth Des.* **2011**.

[37]   I. Ojea-jim, N. G. Bast, V. Puntes, *J. Phys. Chem. C* **2011**, *2*, 15752.

[38]   C. Y. Jiang, X. W. Sun, G. Q. Lo, D. L. Kwong, J. X. Wang, *Appl. Phys. Lett.* **2007**, *90*, 263501.

[39]   A. L. Briseno, T. W. Holcombe, A. I. Boukai, E. C. Garnett, S. W. Shelton, J. J. M. Fréchet, P. Yang, *Nano Lett.* **2010**, *10*, 334.

[40]   Y. Qiu, K. Yan, H. Deng, S. Yang, *Nano Lett.* **2012**, *12*, 407.

[41]   T. Zhang, W. Dong, M. Keeter-Brewer, S. Konar, R. N. Njabon, Z. R. Tian, *J. Am. Chem. Soc.* **2006**, *128*, 10960.

[42]   T. L. Sounart, J. Liu, J. a. Voigt, J. W. P. Hsu, E. D. Spoerke, Z. Tian, Y. B. Jiang, *Adv. Funct. Mater.* **2006**, *16*, 335.

[43] T. Sounart, J. Liu, J. Voigt, *J. Am. Chem. Soc.* **2007**, *129*, 15786.

[44] F. Zhao, J.-G. Zheng, X. Yang, X. Li, J. Wang, F. Zhao, K. S. Wong, C. Liang, M. Wu, *Nanoscale* **2010**, *2*, 1674.

[45] H. Morkoc, U. Ozgur, *Zinc Oxide: Fundamentals, Materials and Device Technology*; Wiley-VCH Verlag GmbH & Co. KGaA: Weinheim, Germany, 2009.

[46] Z. Li, Y. Xiong, Y. Xie, *Inorg. Chem.* **2003**, *42*, 8105.

[47] A. McLaren, T. Valdes-Solis, G. Li, S. C. Tsang, *J. Am. Chem. Soc.* **2009**, *131*, 12540.

4
Sb-Doped Core-Shell ZnO Nanowires

Core-shell nanowires are an important class of structures for functional units in optoelectronic and spintronic devices owing to their interface properties. In this chapter, the fabrication of ZnO @ Sb-doped ZnO core-shell nanowires is demonstrated. They are prepared by PEG-assisted hydrothermal method using antimony glycolate as the dopant source. The morphology and crystallinity of prepared structures, oxidation state of the dopant, and dopant distribution have been investigated using SEM, TEM, EDX, and XPS. The results show that the core-shell nanowires are single crystalline and epitaxially grown radially over ZnO nanowires. The oxidation states of the dopants and their distribution show successful incorporation of the dopants in ZnO host matrix. Since the process is based on the radial secondary growth, a perfect site-selectivity of dopant distribution is achieved. As a proof of concept experiment, the magnetization behaviors of the prepared structures have also been studied.

4.1 Introduction

4.1.1 Core-shell Nanowires

Engineering II-VI and III-V group semiconductors by introducing various types of impurities makes them suitable candidates for applications in electronics, spintronics, and optics.[1–13] Tailoring the morphology and functional properties of semiconductor nanostructures has been a long-standing goal in the development of bottom-up device fabrication processes. Integration of semiconductor nanostructures in devices is intriguing to improve efficiency, cost effectiveness, and size.[14–17] Semiconductor hetero-structures or homo-structures fabricated by manipulating the composition or doping enable passivation of interfaces and the generation of devices with novel electronics and/or optics functions.[18] Introduction of hetero-junctions and homo-junctions in semiconductors has produced many devices of immense utility.

In this perspective, axial, radial, branched, and hierarchical heterostructures have been prepared by modulation of composition and/or doping for different applications.[19–24] Being a potential candidate in various modern devices, ZnO based heterostructures attracted research attention in recent years.[22–24] Among these heterostructures, designs in which coaxial structures with a doped nanowire core surrounded by a shell of identical or opposite doping type are of particular interest.[25–28] A one-dimensional core–shell junction could play several important roles in device applications. First, if the shell is selectively doped to achieve a larger bandgap, charge carriers can be injected and confined in the core, generating a quasi-one-dimensional electron system with higher mobility. Second, highly doped nanowire shells can effectively reduce the depletion region in core−shell nanowires, thus avoiding the formation of fully depleted shells. Another advantage of such coaxial nanowires is that a high doping level in the nanowire shell can lead to low resistive contacts, resulting in fewer constraints on material quality. Moreover, in recent photovoltaic applications, a coaxial nanowire p-n junction is capable of decoupling carrier extraction across the radius of the nanowire, reducing carrier recombination before charge separation. Meanwhile, the long axial length of the nanowires can still permit high optical absorption of incoming light.[27] Such a core−shell nanowire photovoltaic cell design has been confirmed to achieve higher photovoltaic efficiency.[26] In the various fields mentioned above, core−shell nanowires with coaxial homogeneous junctions have become an imperative option in materials design as they facilitate energy band engineering and charge transfer in radial direction.

There have been considerable efforts toward the fabrication of ZnO based core-shell structures using different physical and chemical deposition methods. In this regard, strategies using a solvothermal method are advantageous compared to other techniques as they are inexpensive, simple, and more environmentally benign.[29,30] Moreover solution based methods are fundamentally one of the best methods for large-scale fabrication of the structures, which is vital when the structural units are used in devices in future.

The difficulty to control the radial growth of ZnO holds the key for development of radial heterostructures either by doping or modulating the composition. For example, already grown ZnO nanowires when put in a fresh growth solution does not lead to radial growth.[31] Addition of impurities during the primary growth also faces challenges in terms of dopant distribution in the structure. Therefore, so as to obtain a well-controlled modulation profile, a reasonable radial, secondary growth strategy for site-selective doping of ZnO nanowires has to be adopted.

4.1.2 p-Type Doping of ZnO

ZnO is intrinsically a n-type semiconductor. The source of inadvertent n-type conduction characteristics of ZnO nanowires is under debate. In the past, it has been postulated that it originates from oxygen vacancies and interstitial Zn. But recent measurements and density functional calculations have shown that oxygen vacancies are actually deep donors and cannot contribute to n-type conductivity[32–35] and point defects such as Zn interstitials are also implausible causes of the n-type conductivity observed in as-grown ZnO crystals.[36] Additionally it has also been reported that unintentional incorporation of impurities that act as shallow donors, such as hydrogen which is unavoidable in almost all growth conditions.[37,38]

A reliable method for p-type doping of ZnO faces many challenges besides its tendency toward n-type conductivity. Even though the defects do not contribute to n-type conductivity, they do play a role as compensating centers in p-type doping. In addition to that the selection of an efficient p-type dopant for ZnO, which is majorly chosen according to the size and electronegativity of the anion, has been one of the hurdles for a long time. But there are many reports showing successful p-doping with large-size-mismatched dopants (P, As, Sb)[39–43] and K[44] which are considered to be deep acceptors on Zn site or stable as interstitial donors that compensate p-type conductivity.

The cause of p-typeness of Sb-doped ZnO has been a puzzle for a long time considering possibility of chemical bonding and the mismatch in ionic radii. The solubility of Sb ions in ZnO substituting O^{2-} is very low due to larger ionic radius of Sb ions compared to that of O^{2-}. Moreover it has also been established that the substitutional Sb cannot act as a shallow acceptor thereby contribute to p-typeness. In order to explain the p-type characteristics of Sb-doped ZnO, a new model has been suggested that Zn antisites, instead of O^{2-} are substituted by Sb cations.[45] This results in Sb_{Zn}-$2V_{Zn}$ complexes in which Sb ion occupies a Zn antisite and is accompanied by two Zn vacancies. These Sb_{Zn}-$2V_{Zn}$.complexes can act as shallow acceptors, which might be responsible for the p-typeness of Sb-doped ZnO. This model explains well the reported p-type nature of Sb-doped ZnO and has been experimentally validated by lattice location studies using radioactive isotope ^{124}Sb.[46] Besides the p-typeness, Sb_{Zn}-$2V_{Zn}$ seemingly can introduce ferromagnetism in Sb-doped ZnO. The ferromagnetism in Sb-doped ZnO is mainly due to Sb_{Zn}-$2V_{Zn}$ which originates from the p-p and p-d coupling interaction between the dopant Sb p orbitals and the host O 2p and Zn 3d orbitals.[47,48]

The Sb_{Zn}-$2V_{Zn}$-model encouraged the efforts to dope ZnO nanowires with Sb by various methods.[43,49–51] Introduction of Sb ions in to ZnO matrix by hydrothermal method faces many challenges since direct addition of Sb ionic salts would undergo hydrolysis in water medium. There are barely any Sb salts that are both water soluble and compatible with the ZnO growth condition. But this problem can be overcome using a chelating agent that coordinates with Sb.[51] Among these approaches, hydrothermal method using coordinate compounds of Sb^{3+} with α-hydroxycarboxylate ligands produce nanowires with reliable p-type conductivity.[43] But hydrothermal synthesis of Sb-doped core-shell nanowires is barely reported.

In the present study, a facile hydrothermal strategy to prepare ZnO core–shell nanowires based on seeded secondary growth to achieve radial growth and simultaneous site-selective doping of ZnO nanowires is presented. In general ZnO nanowires with the intrinsic hexagonal wurtzite structure are known to grow along the [0001] direction (*c*-axis) by alternatively stacking planes composed of O^{2-} anions and Zn^{2+} cations. As shown in *Chapter 3*, a versatile *c*-growth inhibitor like polyethylene glycol (PEG) can induce secondary growth of ZnO nanowire seeds preferentially along the nonpolar {10-10} surfaces.[31] Herein, the PEG-assisted epitaxial growth process is modified by the addition of Sb dopant to prepare ZnO@Sb-doped ZnO core–shell nanowires, thus forming a radial junction. Here the

investigations are particularly focused on the detailed structural features of these two ZnO core–shell nanowires to understand the dopant distribution profile in the coaxial nanowires. Magnetic properties of the ZnO coaxial nanowires induced by doping of Sb are also inspected.

4.2 Results and Discussion

4.2.1 Growth and Characterization

For the primary growth of ZnO nanowires, a uniform ZnO film with a thickness of 30 nm was grown on Si substrates by atomic layer deposition (ALD) to serve as the seed layer. The substrate with the seed layer was placed facing downward into an aqueous solution system containing zinc nitrate ($Zn(NO_3)_2$) and hexamethylenetetramine (HMTA). Figure 1a shows an SEM image of ZnO nanowires formed under normal growth condition, in which dense nanowires about 80 nm in diameter are aligned on the silicon substrate. The as-grown ZnO nanowires have a hexagonal cross-section together with a smooth side surface.

Since Sb ionic salts are extremely easy to hydrolyze in aqueous medium, introduction of Sb ions into the ZnO matrix was conducted by adding Sb^{3+} ions coordinated with a chelating agent to ZnO solution *via* this hydrothermal method.[43] In this experiment, water-soluble antimony glycolate was used as a source of the dopant to achieve a slow dopant release rate.[43] The SEM image in figure 1b shows that Sb-doped primary ZnO nanowires are short and bunched together. The nanowires are on average ∼200–400 nm in diameter (figure 1c), much larger than those grown without Sb doping. The surfaces of these structures are rough, indicating that the impurities dramatically affected the growth behavior of ZnO nanowires. It was suggested that an antimony glycolate absorption doping mechanism should be responsible for this doping process.[43] The incorporation of Sb ions onto the growing surfaces of ZnO possibly altered the steps based on a layer-by-layer growth mode.
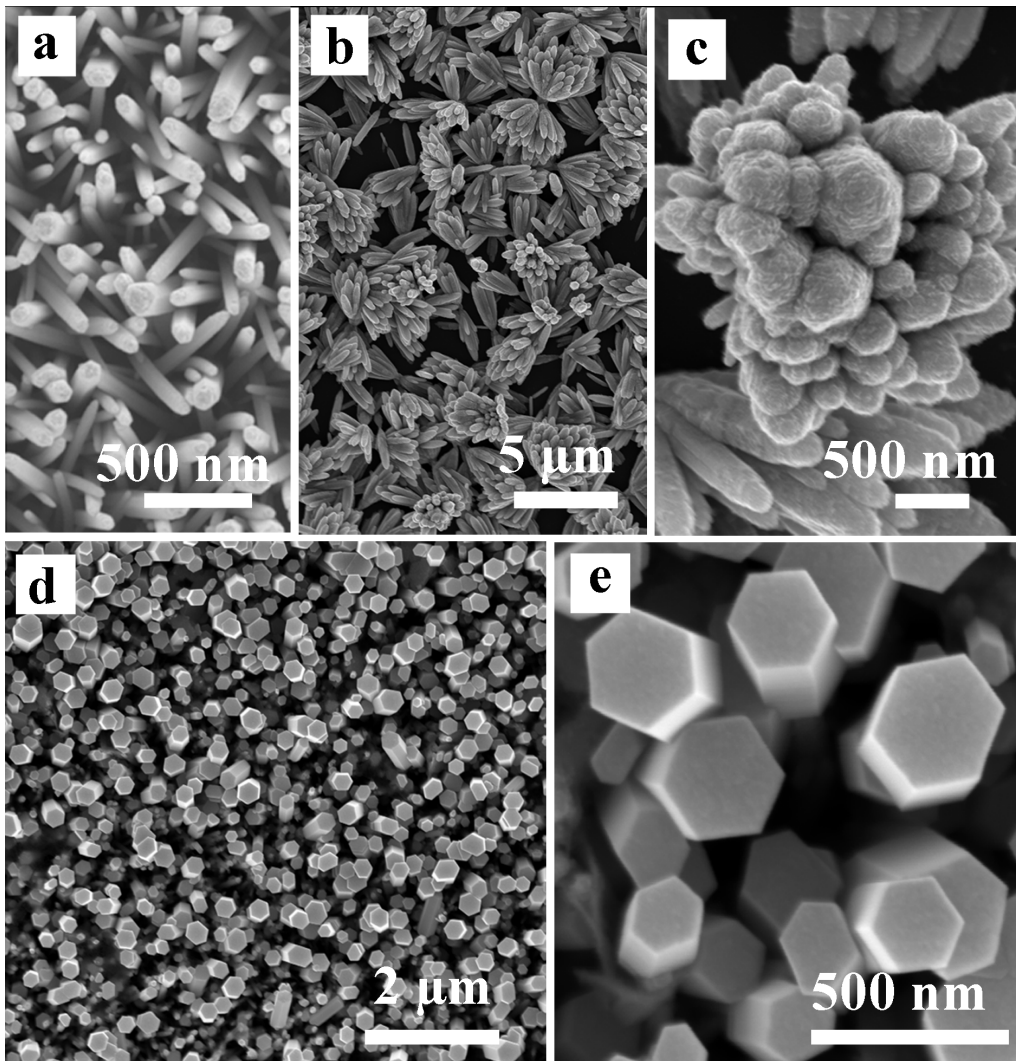
Figure 1. Morphologies of undoped and Sb-doped ZnO nanowires: (a) SEM image of hydrothermally grown ZnO nanowires. (b) SEM image of Sb-doped primary ZnO nanowires. A close view is shown in (c). (d) SEM image of ZnO@Sb-doped ZnO core–shell nanowires. A close view is shown in (e).

It has been shown that a radial secondary growth of primary ZnO nanowires can occur in the presence of capping agents such as polyethylene glycol (PEG).[31] PEG is found to act as a structure-directing agent by binding to the Zn-terminated polar (0001) surface of ZnO, thus inhibiting the axial growth of the ZnO nanowires. For growing Sb-doped ZnO shells over ZnO nanowires, the as-grown primary ZnO nanowire array (figure 1a) was used as nanowire seeds and inserted into an aqueous solution of $Zn(NO_3)_2$, HMTA, Sb dopant solution (antimony glycolate), and 1 mL of PEG. In the subsequent secondary growth, the

axial growth of the primary ZnO nanowires was apparently suppressed. Relative to the primary ZnO nanowires, radial growth happened as shown in figure 1d and 1e. This result is consistent with the previous findings discussed in *Chapter 3* regardless of the existence of the Sb dopant source antimony glycolate in the current system. The thickness of the layer depends on the concentration of the reactant precursors in the bath and the growth duration. In the given experiment, the optimal time for the secondary growth was 6 hours to obtain well-faceted ZnO nanowires with a perfect hexagonal geometry. It was observed from high resolution TEM analysis that the resulting ZnO nanostructures from secondary growth are perfectly single crystalline and forms no boundaries between the primarily grown nanowire core and the secondarily grown layer over it (figure 2a-d). The side surface was quite flat. As expected for ZnO wurtzite crystal structure, the lattice spacing for the defect-free lattice is 0.52 nm.

To confirm the inclusion of Sb in ZnO matrix and to evaluate the chemical state of the dopant, an XPS analysis of the sample was conducted. The Zn $2p_{3/2}$ peak appears at 1021.8 eV and the LMM Auger line at 988 eV indicating the presence of Zn in oxidation state +2.[52] Figure 2e shows the spectra of O1s overlapped with the doublet Sb $3d_{5/2}$ and Sb $3d_{3/2}$ at 530.4 eV and 539.9 eV respectively, which can be attributed to Sb in oxidation state +3.[53,54] Because of the overlapping of O 1s and Sb $3d_{5/2}$ signals, only the Sb $3d_{3/2}$ peak was used for the quantitative analysis. For an Sb concentration in the growth solution of 32 vol%, this resulted in 4.7 at% of Sb and 21.7 at% of Zn. When the concentration of the antimony dopant in the growth solution was doubled, the Sb concentration in the shell increased to 12.6 at%, an increase of Sb by the factor of 2.6. This result suggests that the doping concentration can be tuned by adjusting the volume of the soluble Sb dopant source.
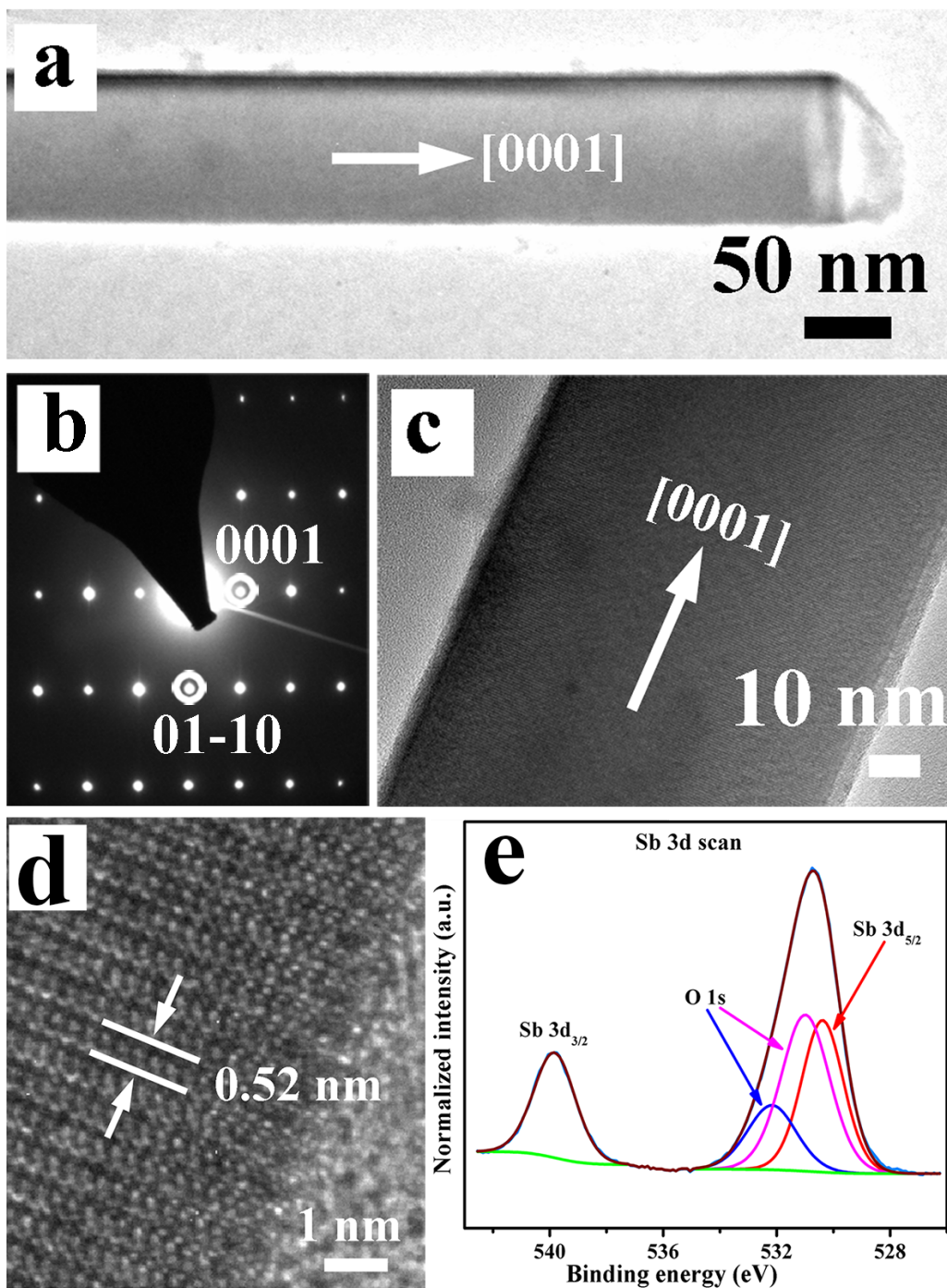
Figure 2. (a) TEM image of a ZnO@Sb-doped ZnO core–shell nanowire. (b) Corresponding electron diffraction pattern. (c, d) Zoom-in TEM image of a ZnO@Sb-doped ZnO core–shell nanowire and HRTEM image near its sidewall. (e) XPS O 1s and Sb 3d spectra of the ZnO@Sb-doped ZnO core–shell nanowires.

To understand the distribution profile of Sb, a detailed elemental mapping study was conducted for a single secondarily-grown nanowire (figure 3). As depicted in figure 3d, the concentration of Sb is prominent at both sides, while the concentration remains uniform for the rest of the area selected. This elemental distribution in projection is characteristic for a thin shell with a high Sb concentration around a core without Sb. Considering the radial epitaxial growth mode, the dopant Sb is most likely distributed throughout the secondary layer, thus forming the ZnO@Sb-doped ZnO core–shell nanowires. The abundance of Sb in the shell was further confirmed by EDX spectrum of an area selected from figure 3d, as given in figure 3b.
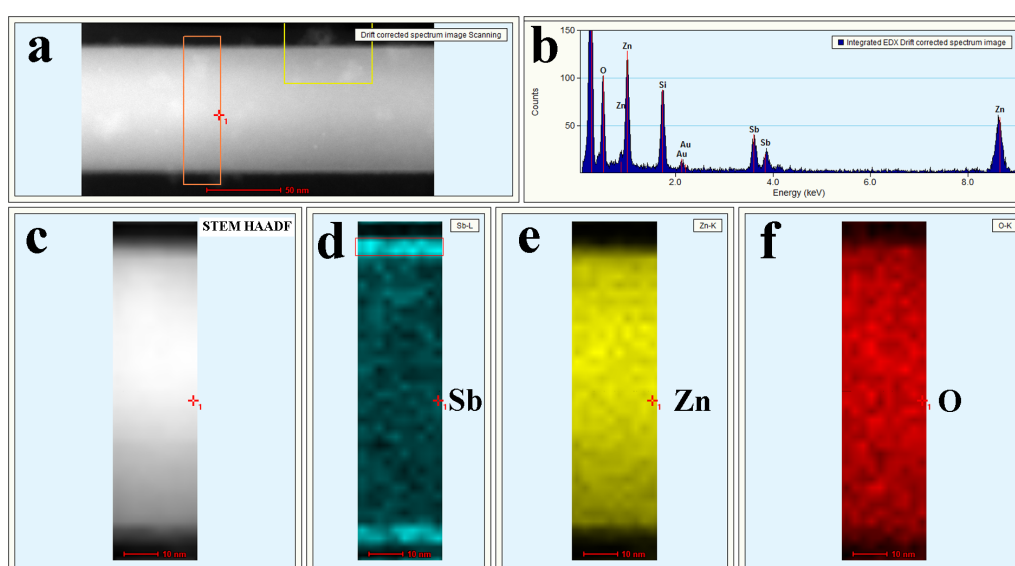

Figure 3: Elemental analysis of ZnO@Sb-doped ZnO core–shell nanowires. (a) STEM-HAADF image of a nanowire. (b) EDX spectrum of the selected area marked in (d). (c) The part of the nanowire selected for mapping. (d–f) elemental mapping images of the area.

The above structural investigations demonstrated that the dopant Sb was incorporated in the secondary shell of the undoped primary ZnO nanowires during radial growth under the assistance of PEG. It was speculated that *in situ* Sb doping occurs based on adsorption of Sb-coordinating ions onto the growing surface of ZnO, followed by desorption of the ligands.[43] Then additional host material ZnO buries the Sb ions. However, the incorporation of Sb ions onto the growing surfaces of ZnO might lead to growth steps less reactive or inoperative, thus resulting in a reduced axial growth and greater radial growth of the nanowires.[43] This is most likely the reason why the Sb-doped primary ZnO nanowires (figure 1b) are much thicker than the undoped ones (figure 1a). When PEG was used as *c*-growth inhibitor during

secondary growth, the upcoming ZnO preferentially grows on the ZnO nanowire side facets. With the simultaneous doping process, the accumulation of Sb ions on the ZnO side surfaces further contributed to the radial growth by acting as a surfactant to decrease adatom diffusion length. The good faceted structure of the starting ZnO nanowires was maintained during the epitaxial lateral growth. In addition, the tapered evolution of the top surface was prevented due to the restrained axial growth, which led to the secondarily-grown ZnO nanowires with perfect hexagonal morphology. Considering that the primary undoped ZnO nanowires are intrinsically n-type, the Sb-doped p-type ZnO shells are expected to lead to ZnO core–shell p–n junction nanowires.

4.2.2 Magnetization

One of the interests in doping in II-VI and III-V group semiconductors lies in their novel magnetic properties as diluted magnetic semiconductors (DMSs). Therefore, the magnetization behavior of the Sb-doped and Co-doped core–shell nanowire arrays was studied at 300 K and 70 K (figure 4). The measurements revealed that both the ZnO@Sb-doped ZnO and ZnO@Co-doped ZnO core–shell nanowire arrays exhibited a magnetic hysteresis at room temperature due to the successful doping processes.

The room temperature ferromagnetism of Sb- and Mn- codoped ZnO nanowires was reported while Mn-doped ZnO under similar compositions and conditions did not show ferromagnetism.[47] The saturation magnetization (Ms), remanence (Mr), and coercivity (Hc) of Sb-doped ZnO core–shell nanowire array were found to be 6.8×10^{-5} emu, 2.8×10^{-5} emu, and 222.3 Oe at 70 K whereas 4.9×10^{-5} emu, 1.1×10^{-5} emu, and 218.4 Oe were measured at 300 K. Recently, DFT calculations have shown that both Sb_O and Sb_{Zn}-$2V_{Zn}$ are of magnetic nature.[48] According to Sb_{Zn}-$2V_{Zn}$ model, the magnetic moments in Sb-doped ZnO originate from the O atoms that are the nearest neighbors to the V_{Zn}. Moreover under oxygen-rich conditions, Sb dopant favors the formation of Sb_{Zn}-$2V_{Zn}$ complexes.[49] Therefore the origin of magnetism in the Sb-doped sample could be triggered by Sb_{Zn}-$2V_{Zn}$ complex.
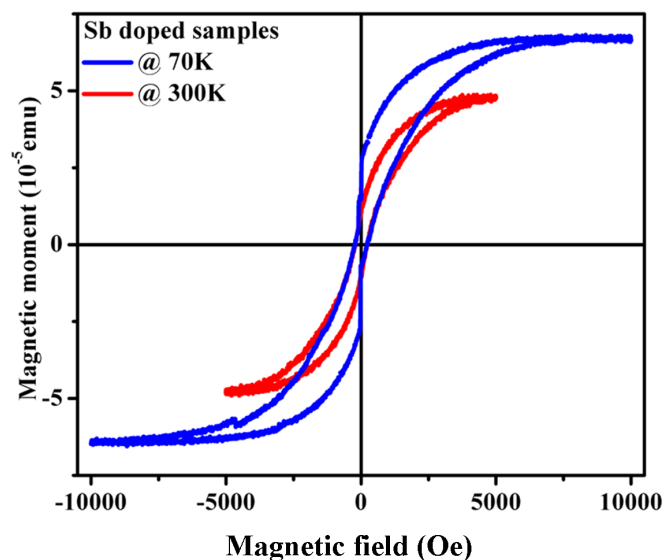
Figure 4. Magnetization behavior of ZnO@Sb-doped ZnO core–shell nanowires at 300 K and 70 K.

4.3 Summary

A hydrothermal synthetic route for the fabrication of ZnO@Sb-doped ZnO core-shell nanowires using already prepared ZnO nanowires as templates has been developed. Sb-doping of the shell has been achieved by using Sb-glycolate as the dopant source. In this process PEG was used as a capping reagent to inhibit the growth of primary ZnO nanowires along the axial direction, and thus to achieve radial growth. The secondarily-grown ZnO layer was successfully doped with Sb through adsorption of Sb-glycolate ions onto the lateral growing surface of ZnO, followed by desorption of the ligands. Since the growth is epitaxial, perfect morphology control was observed. To demonstrate successful doping, magnetizations of the samples are also shown. These strategies can be used to prepare different types of core-shell ZnO 1-D heterostructures that are envisioned to be potential functional units in electrical and spintronic devices.

4.4 References

[1]   R. Fiederling, M. Keim, G. Reuscher, W. Ossau, G. Schmidt, A. Waag, L. W. Molenkamp, *Nature* **1999**, *402*, 787.

[2]   Y. Ohno, D. Young, B. Beschoten, F. Matsukura, H. Ohno, D. D. Awschalom, *Nature* **1999**, *402*, 790.

[3]   T. Dietl, H. Ohno, F. Matsukura, J. Cibert, D. Ferrand, *Science* **2000**, *287*, 1019.

[4]   P. Sharma, A. Gupta, K. V Rao, F. J. Owens, R. Sharma, R. Ahuja, J. M. O. Guillen, B. Johansson, G. A. Gehring, *Nat. Mater.* **2003**, *2*, 673.

[5]   K. Sato, H. Katayama-Yoshida, *Phys. E* **2001**, *10*, 251.

[6]   K. Ueda, H. Tabata, T. Kawai, *Appl. Phys. Lett.* **2001**, *79*, 988.

[7]   D. C. Kundaliya, S. B. Ogale, S. E. Lofland, S. Dhar, C. J. Metting, S. R. Shinde, Z. Ma, B. Varughese, K. V Ramanujachary, L. Salamanca-Riba, T. Venkatesan, *Nat. Mater.* **2004**, *3*, 709.

[8]   J. H. Kim, H. Kim, D. Kim, Y. Ihm, W. K. Choo, *J. Eur. Ceram. Soc.* **2004**, *24*, 1847.

[9]   J. H. Park, M. G. Kim, H. M. Jang, S. Ryu, Y. M. Kim, *Appl. Phys. Lett.* **2004**, *84*, 1338.

[10]   Y. Q. Chang, D. B. Wang, X. H. Luo, X. Y. Xu, X. H. Chen, L. Li, C. P. Chen, R. M. Wang, J. Xu, D. P. Yu, *Appl. Phys. Lett.* **2003**, *83*, 4020.

[11]   J.-J. Wu, S.-C. Liu, M.-H. Yang, *Appl. Phys. Lett.* **2004**, *85*, 1027.

[12]   W. Liang, B. D. Yuhas, P. Yang, *Nano Lett.* **2009**, *9*, 892.

[13]   C. Klingshirn, *ChemPhysChem* **2007**, *8*, 782.

[14]   B. Tian, X. Zheng, T. J. Kempa, Y. Fang, N. Yu, G. Yu, J. Huang, C. M. Lieber, *Nature* **2007**, *449*, 885.

[15]   M. Grätzel, *Nature* **2001**, *414*, 338.

[16]   X. Duan, Y. Huang, Y. Cui, J. Wang, C. M. Lieber, *Nature* **2001**, *409*, 66.

[17]   Y. Cui, Q. Wei, H. Park, C. M. Lieber, *Science* **2001**, *293*, 1289.

[18]   S. Sze, *Physics of Semiconductor Devices*; Wiley-Interscience: New York, 1969.

[19]   M. S. Gudiksen, L. J. Lauhon, J. Wang, D. C. Smith, C. M. Lieber, *Nature* **2002**, *415*, 617.

[20] M. T. Björk, B. J. Ohlsson, T. Sass, a. I. Persson, C. Thelander, M. H. Magnusson, K. Deppert, L. R. Wallenberg, L. Samuelson, *Appl. Phys. Lett.* **2002**, *80*, 1058.

[21] L. J. Lauhon, M. S. Gudiksen, D. Wang, C. M. Lieber, *Nature* **2002**, *420*, 57.

[22] X. Wang, P. Gao, J. Li, C. J. Summers, Z. L. Wang, *Adv. Mater.* **2002**, *14*, 1732.

[23] C.-Y. Chang, H.-M. Huang, Y.-P. Lan, T.-C. Lu, L.-W. Tu, W.-F. Hsieh, *Cryst. Growth Des.* **2013**, *13*, 3098.

[24] A. Kargar, Y. Jing, S. J. Kim, C. T. Riley, X. Pan, D. Wang, *ACS Nano* **2013**, *7*, 11112.

[25] J. Yoo, C.-H. Lee, Y.-J. Doh, H. S. Jung, G.-C. Yi, *Appl. Phys. Lett.* **2009**, *94*, 223117.

[26] J. A. Czaban, D. A. Thompson, R. R. LaPierre, *Nano Lett.* **2009**, *9*, 148.

[27] M. Heurlin, O. Hultin, K. Storm, D. Lindgren, M. T. Borgström, L. Samuelson, *Nano Lett.* **2014**, *14*, 749.

[28] D. C. Dillen, K. Kim, E.-S. Liu, E. Tutuc, *Nat. Nanotechnol.* **2014**, *9*, 116.

[29] H. Wang, H. B. Wang, F. J. Yang, Y. Chen, C. Zhang, C. P. Yang, Q. Li, S. P. Wong, *Nanotechnology* **2006**, *17*, 4312.

[30] B. Panigrahy, M. Aslam, D. Bahadur, *J. Phys. Chem. C* **2010**, *114*, 11758.

[31] R. Kozhummal, Y. Yang, F. Güder, A. Hartel, X. Lu, U. M. Küçükbayrak, A. Mateo-Alonso, M. Elwenspoek, M. Zacharias, *ACS Nano* **2012**, *6*, 7133.

[32] A. Janotti, C. G. Van de Walle, *Appl. Phys. Lett.* **2005**, *87*, 122102.

[33] A. Janotti, C. G. Van de Walle, *Rep. Prog. Phys.* **2009**, *72*, 126501.

[34] L. Vlasenko, G. Watkins, *Phys. Rev. B* **2005**, *71*, 125210.

[35] L. Vlasenko, G. Watkins, *Phys. Rev. B* **2005**, *72*, 035203.

[36] A. Janotti, C. G. Van de Walle, *J. Cryst. Growth* **2006**, *287*, 58.

[37] A. Janotti, C. G. Van de Walle, *Nat. Mater.* **2007**, *6*, 44.

[38] Van De Walle CG, *Phys. Rev. Lett.* **2000**, *85*, 1012.

[39] K.-K. Kim, H.-S. Kim, D.-K. Hwang, J.-H. Lim, S.-J. Park, *Appl. Phys. Lett.* **2003**, *83*, 63.

[40] C. Morhain, M. Teisseire, S. Vézian, F. Vigué, F. Raymond, P. Lorenzini, J. Guion, G. Neu, J.-P. Faurie, *Phys. Status Solidi B* **2002**, *229*, 881.

[41] Y. R. Ryu, T. S. Lee, H. W. White, *Appl. Phys. Lett.* **2003**, *83*, 87.

[42] T. Aoki, Y. Shimizu, A. Miyake, A. Nakamura, Y. Nakanishi, Y. Hatanaka, *Phys. Status Solidi B* **2002**, *229*, 911.

[43] F. Wang, J.-H. Seo, D. Bayerl, J. Shi, H. Mi, Z. Ma, D. Zhao, Y. Shuai, W. Zhou, X. Wang, *Nanotechnology* **2011**, *22*, 225602.

[44] X. S. Nguyen, C. B. Tay, E. A. Fitzgerald, S. J. Chua, *Small* **2012**, *8*, 1204.

[45] S. Limpijumnong, S. Zhang, S.-H. Wei, C. Park, *Phys. Rev. Lett.* **2004**, *92*, 155504.

[46] U. Wahl, J. G. Correia, T. Mendonça, S. Decoster, *Appl. Phys. Lett.* **2009**, *94*, 261901.

[47] G.-H. Ji, Z.-B. Gu, M.-H. Lu, D. Wu, S.-T. Zhang, Y.-Y. Zhu, S.-N. Zhu, Y.-F. Chen, *J. Phys. Condens. Matter* **2008**, *20*, 425207.

[48] Y.-B. Lu, Y. Dai, M. Guo, L. Yu, B. Huang, *Phys. Chem. Chem. Phys.* **2013**, *15*, 5208.

[49] W. Guo, A. Allenic, Y. B. Chen, X. Q. Pan, Y. Che, Z. D. Hu, B. Liu, *Appl. Phys. Lett.* **2007**, *90*, 242108.

[50] F. X. Xiu, Z. Yang, L. J. Mandalapu, D. T. Zhao, J. L. Liu, W. P. Beyermann, *Appl. Phys. Lett.* **2005**, *87*, 152101.

[51] J. Briscoe, D. E. Gallardo, S. Dunn, *Chem. Commun.* **2009**, 1273.

[52] S. Bera, S. Dhara, S. Velmurugan, A. K. Tyagi, *Int. J. Spectrosc.* **2012**, *2012*, 1.

[53] F. Montilla, E. Morallón, A. De Battisti, S. Barison, S. Daolio, J. L. Vázquez, *J. Phys. Chem. B* **2004**, *108*, 15976.

[54] T. Honma, R. Sato, Y. Benino, T. Komatsu, V. Dimitrov, *J. Non. Cryst. Solids* **2000**, *272*, 1.

5 Co-doped ZnO Core-shell ZnO Nanowires

As discussed in Chapter 4, epitaxial secondary growth of ZnO nanowires by PEG-assisted method offers rational control over site-selectivity of dopant distribution. Unlike the case of Sb, this method does not produce transition metal-doped ZnO due to exhaustive precipitation of dopants. In this chapter, a nonaqueous strategy to fabricate ZnO@Co-doped core–shell nanowires is demonstrated, where ethylene glycol is used both as the solvent and the axial growth inhibitor. The growth of ZnO nanowires are disturbed by ethylene glycol and whisker-like lateral growth occurs accompanied with the incorporation of the Co dopants into the shell. The morphology and crystallinity of the prepared structures, the oxidation state of the dopant, and the dopant distributions have been investigated. As a proof of concept experiment, the magnetization behavior of the prepared structures has also been shown.

5.1 Introduction

5.1.1 Transition Metal Doping of ZnO Nanowires

Transition metal doping of II-VI and III-V group semiconductors has been generating much research interest predominantly for their novel magnetic properties as diluted magnetic semiconductors (DMSs). They have already been explored as the spin-polarization materials in spin-dependent light emitting diodes.[1,2] Bulk crystals and thin films of transition metal-doped ZnO has been theoretically predicted and later experimentally proven to be ferromagnetic at room temperature.[3–9] DMSs use the advantage of using both charge and spin of electrons in a semiconductor.[10] Size and dimensionality play a substantial role in determining various properties of such systems. Low dimensional DMS materials are required for integrating them into modern electronics, in order to exploit the advantage offered by spins.[11]

ZnO nanowires can be doped with transition metals in many different techniques like vapor deposition, ion implantation, electrodeposition etc.[12–14] Simple addition of metal ions into the ZnO nanowire growth solution does not essentially result in inclusion of transition metal atoms in ZnO nanowires. It was suggested that the interfacial energy must be adjusted to reduce the energy barrier for the incorporation of dopants into the ZnO nanowires.[15] Cui *et al.* used a negative potential of 0.8 V relative to a gold reference electrode in order to achieve a measurable doping in the nanowires by electrochemical deposition method.[16,17] Strategies using comparatively elevated temperatures, based on low volatile organic solvents like trioctylamine give more control over the doping fraction and thereby ensuing properties.[18,19] In addition, low-temperature hydrothermal routes have also been reported.[20,21] But to the best of knowledge, there has been no report so far for fabrication of ZnO/transition metal-doped ZnO core-shell nanowires based on any of these methods.

PEG-assisted growth with the addition of transition metal salts does not lead to successful incorporation of dopants in the final nanowires. As reported previously Co-doping of ZnO nanowires using high boiling organic solvents offers a reliable doping pathway, for example, *via* a solution-based reaction using trioctylamine as solvent at 310°C.[19] Therefore, strategy was modified by using ethylene glycol (EG, OH-CH$_2$-CH$_2$-OH), which acts both as the solvent medium and the structure-directing agent in the secondary growth

5.2 Results and Discussion

5.2.1 Co-doping by PEG-assisted Growth

The attempts to dope ZnO nanowires with other transition metal ions in PEG-assisted radial secondary growth approach have failed, as no detectable amount of dopant was found in the ZnO matrix. One major advantage of the strategy described in *Chapter 4* is that the dopant source, antimony glycolate is both soluble in aqueous medium and has a slow dopant release rate. For instance, the attempts to fabricate Co-doped ZnO core–shell nanowires using cobalt nitrate as the dopant source in the PEG-assisted route led to single crystalline, well faceted nanowires, but the structures do not contain any detectable amount of Co (figure 1). This result suggests that the rapid and exhaustive precipitation of the dopant in water prevented the incorporation of Co into the ZnO crystal. As previously reported, Co doping of ZnO using high boiling organic solvents offers a reliable doping pathway.[19] Hence, strategy was modified by substituting the PEG monomer ethylene glycol (EG, OH-CH_2-CH_2-OH) for PEG, which can act both as the solvent medium and the structure-directing agent in the secondary growth.
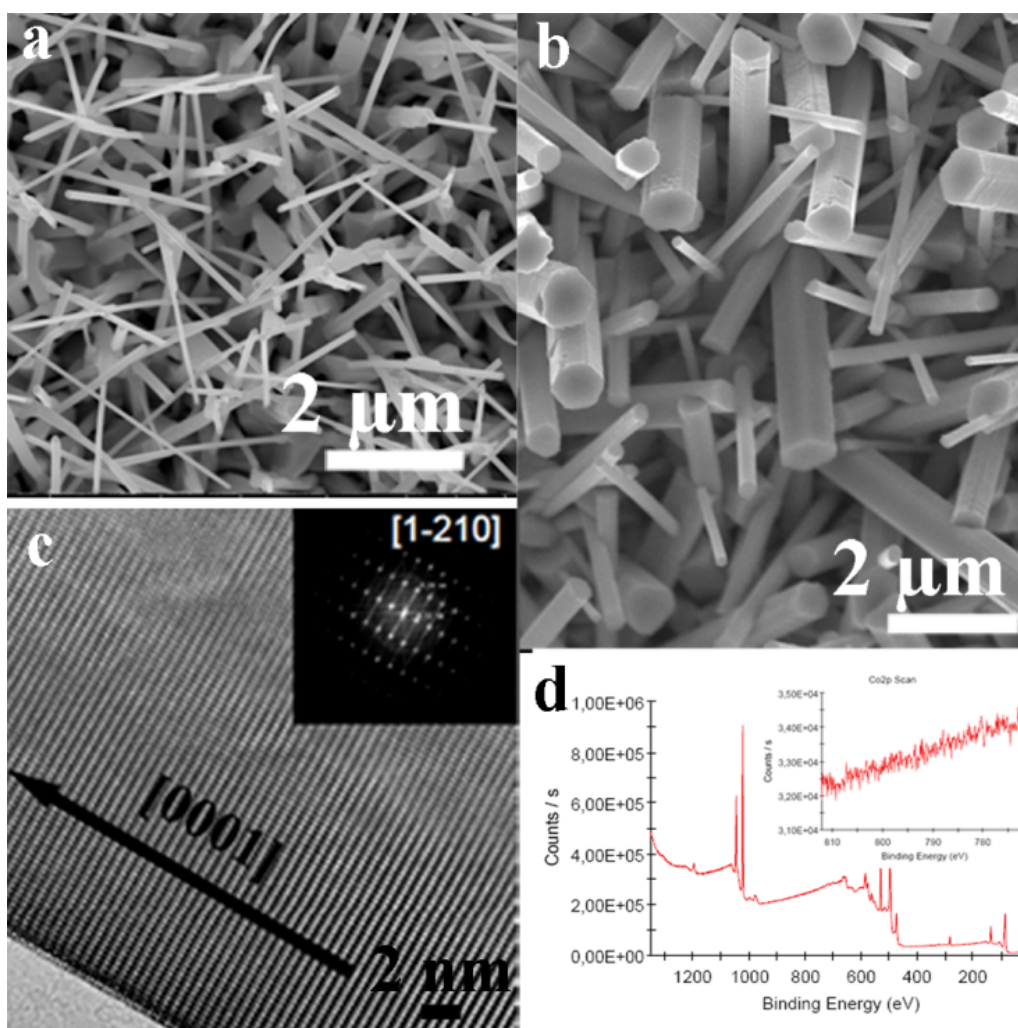
Figure 1. Fabrication of Co-doped ZnO core-shell NWs by PEG-assisted method. (a,b) SEM image of CVD-grown ZnO NW array before and after homoepitaxial lateral growth with the addition of cobalt precursors. (c) HRTEM image of a secondarily-grown nanowire sample. Corresponding FFT pattern is given in the inset. (d) XPS survey spectrum. Co 2p scan is shown in the inset.

5.2.2 Ethylene Glycol-assisted Growth

Ethylene glycol (EG) is a low-volatile hygroscopic liquid with low viscosity and a boiling point of 197.1°C. It has been used as a structure-directing agent in chemical bath deposition (CBD) of ZnO and other metal oxide structures.[22,23] When EG is used as solvent for the secondary growth, the solvothermal reactions could be conducted at much higher temperatures of up to 190 °C compared to those in water. The primary ZnO nanowires

employed in this study were grown on a silicon substrate by a gold-catalyzed chemical vapor deposition (CVD) method, as shown in figure 2a. The secondary growth of the ZnO nanowire seeds was performed in an EG solution consisting of zinc nitrate and HMTA at 180 °C. The dopant source cobalt nitrate was also added to the nutrient solution for simultaneous incorporation of the dopant into the structure. Figure 2b exhibits a representative SEM image of the nanostructures obtained after reaction for 24 hrs. There has been negligible growth observed in axial direction of the primary nanowires; the lengths of the nanowires do not exhibit an obvious change, but the thickness increased considerably after 24 hrs. The surface of these thick, modified nanowires exhibit a noticeable roughness as shown in the magnified image given in the inset of figure 2b. In addition, it was found that the thickness of the nanowires can be tuned by adjusting the growth time. In order to study the interface between the primary core and the shell, nanowires with a thin solid shell are preferred to thick ones. Consequently, the growth time of the samples was also reduced to 1 hour for the detailed structural characterization.
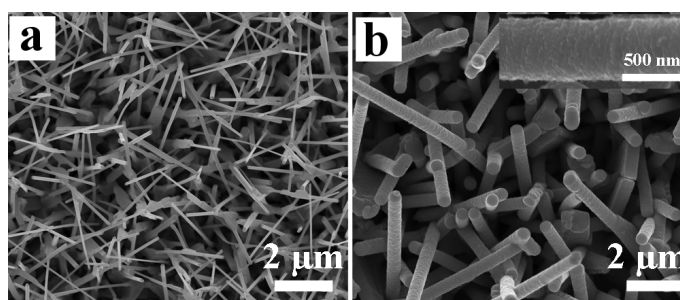

Figure 2. SEM images of (a) as-prepared ZnO nanowires by CVD and (b) the resulting structures formed by secondary growth in EG in the presence of cobalt nitrate. The inset in image (b) shows zoom-in view of a single nanowire after the secondary growth.

HAADF-STEM image of a ZnO nanowire subjected to secondary growth of 24 hours is shown in figure 3a, in which the core–shell nanostructure was clearly observed, indicating the density of the ZnO shell is lower than that of the core. The BF-TEM image in figure 3b demonstrates that the core has a bumpy dense surface, which is further stacked by whisker-like crystals with empty space in between. A high resolution TEM image of the tip of the nanowire is shown in figure 3c. A lattice spacing of 0.52 nm was observed, which fits well to the c lattice constant of the ZnO wurtzite crystal structure. Therefore, the overall orientation of this nanowire is [0001], consistent with that of the primary ZnO nanowires. However, the streaking of its FFT pattern (figure 3d), indicates that the obtained nanowire is not perfectly

single-crystalline due to the overgrowth of the whiskers with slightly different orientation after the secondary growth. By reducing the time of growth to 1 hour, the thickness of the shell was reduced as shown in the HAADF-STEM image in figure 3e. From the HRTEM images in figure 3f and 3g, it can be seen that the growth direction and the lattice spacing remained the same as for the secondarily-grown ZnO nanowires with a thick shell. The bumpy surface hints that the overgrowth of a nonuniform ZnO shell happened from the initial growth stage. This structure showed no streaking in its corresponding FFT pattern (figure 3h). Considering that the growth of the whiskers is not yet as pronounced at this stage, the FFT is almost completely dominated by the ZnO nanowire core. However, no significant lattice deviations can be seen for the outside of the fiber in the image itself, suggesting a regular growth at the beginning of the formation of the whisker-like structures.

XPS spectra were measured for the ZnO nanowires subjected to the secondary growth for 1 hour to verify the presence of the dopant Co in the host lattice. From the Co 2p scan shown in figure 3i, a noisy doublet with peaks at 780.6 eV and 796.0 eV were detected, which corresponds to Co $2p_{3/2}$ and Co $2p_{1/2}$ binding energies, respectively. The spin-orbit splitting of 15.4 eV indicates that the dopant Co in the Co-doped ZnO nanowires may have a valence of +2.[10,20,24] The existence of metallic Co gives a peak difference of 15.05 eV between $2p_{3/2}$ and $2p_{1/2}$.[10,20] The XPS spectrum indicates the presence of Co as Co^{2+}. Moreover there were no metal clusters identified in the structural analysis. Based on the XPS results, the elements at the surface have been quantified. It showed that the surface contains 0.8 at% of Co and 35.3 at% of Zn when 13.3% of Co salts were used in the nutrient solution. When the concentration of the cobalt precursor was doubled in the growth solution, the resulting sample contained an atomic percentage of 1.3 % of Co and 32.5 % of Zn, showing an increase of Co content by a factor of 1.7.
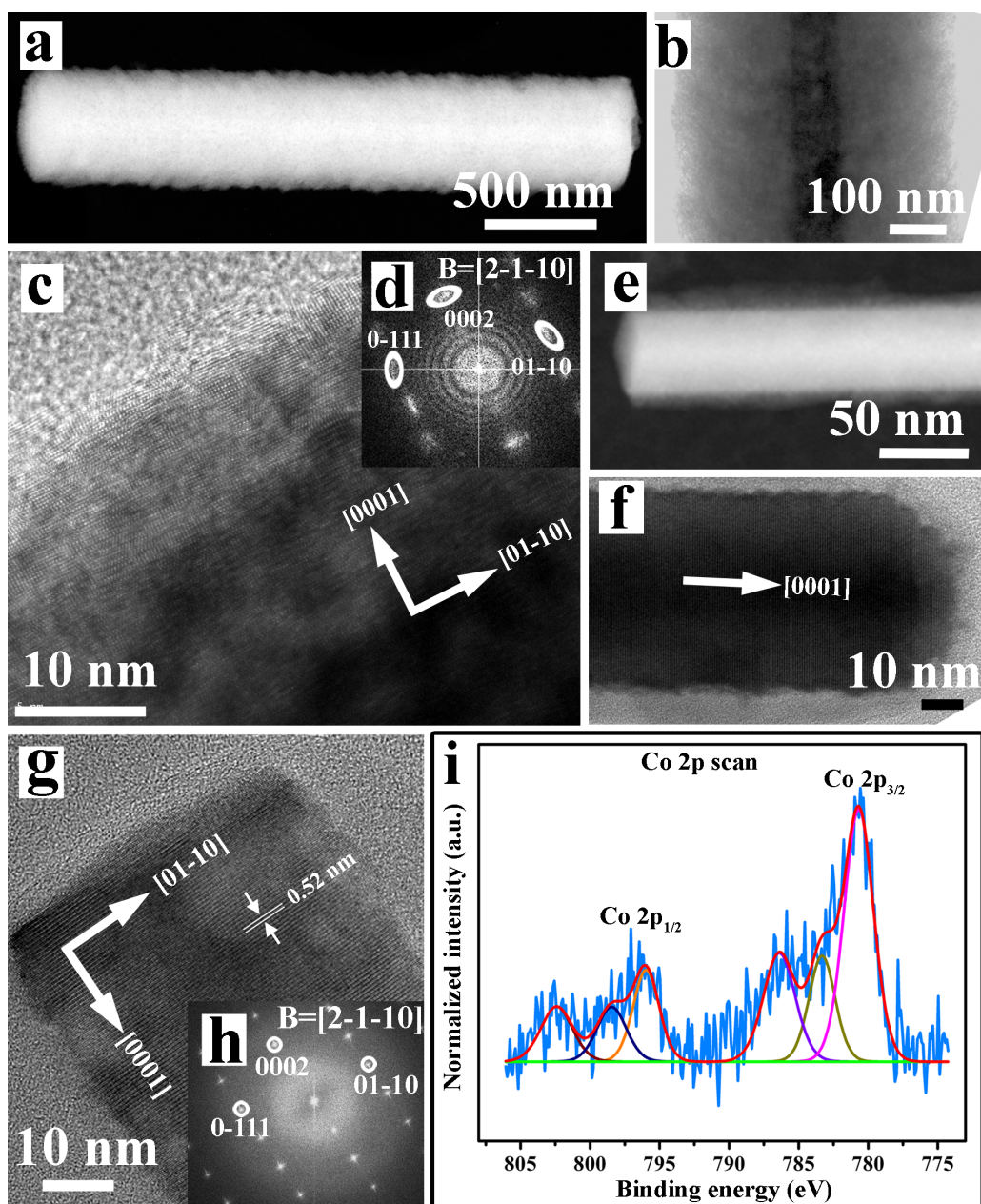
Figure 3. Structural investigations and XPS spectrum of ZnO@Co-doped ZnO core–shell nanowires. (a) HAADF-STEM image of a core–shell nanowire subjected to secondary growth of 24 hrs. (b) Zoom-in view differentiating the core and the shell of the same nanowire. (c) HRTEM image of the tip of a core–shell nanowire with a thick shell. (d) Its corresponding FFT pattern. (e) HAADF-STEM image of nanowire with a thinner shell prepared by reducing reaction time to 1 hr. (f–h) HRTEM images of a nanowire with a thin shell and corresponding FFT pattern of the area shown in image. (i) XPS Co2p spectrum of the sample.

78

To further investigate the distribution of Co in the structure, EDX elemental mapping was done for a ZnO nanowire with a thin shell (figure 4a). It was revealed that the dopant Co is exclusively distributed in the shell region, as shown in figure 4b, similar to the Sb doped core–shell materials as shown in *Chapter 4*. This conclusion was further confirmed by EDX spectra of three different areas marked in figure 4a. The areas were selected in such a way that areas 3 and 5 included more fraction of the shell than the area 4. The separate EDX spectra (figure 4c–e) showed stronger Co peaks in areas 3 and 5, whereas hardly any Co was detected in area 4.
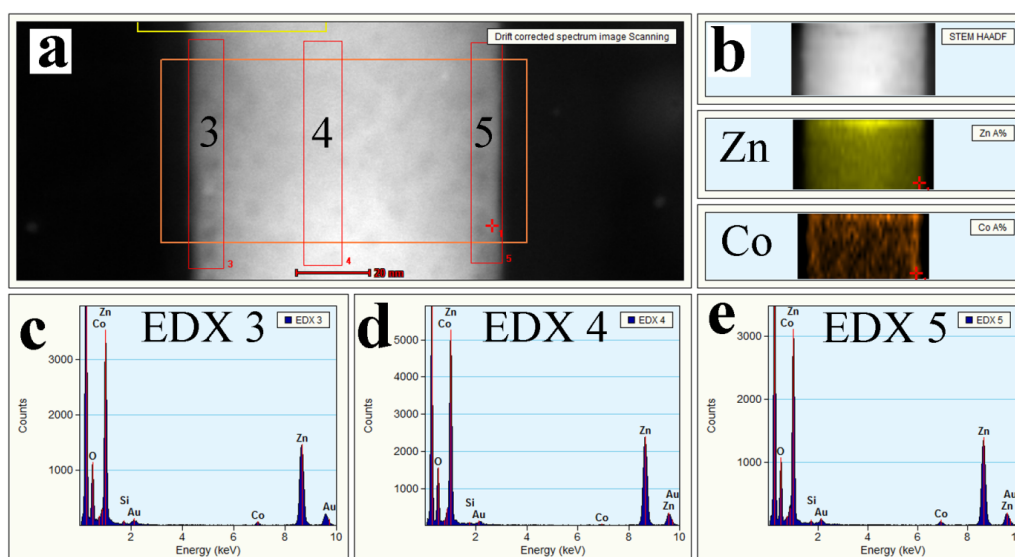

Figure 4. (a) STEM-HAADF image of ZnO@Co-doped ZnO core–shell nanowires. (b) EDX elemental mapping of Zn and Co. (c–e) EDX spectra of areas 3, 4, and 5, respectively.

It is clear that when EG was used as the solvent medium, site-selective doping of cobalt occurred simultaneously with the radial growth of ZnO nanowires. However, in contrast to the PEG-assisted aqueous route for the doping of antimony, the resulting nanowires are not faceted but cylindrical. Structural characterization showed that the shell grown on the ZnO nanowire seeds is of low density, consisting of oriented whisker-like crystals with space in between. Since either EG or the dopant Co can dramatically affect the growth behavior of ZnO in solution, it is necessary to identify the major cause of the emerging phenomena.

First, the growth of ZnO in EG in the absence of the cobalt precursor was investigated. The method was initially carried out on a seed layer of ZnO to test the

efficiency of inhibition to growth of ZnO. A ZnO seed layer of 30 nm thickness was prepared by ALD on a silicon substrate and then annealed at an elevated temperature (figure 5a). Figure 5b shows the morphology of the ZnO nanostructure formed after growth in the nutrient solution for 24 hrs. Different from the seeded growth of ZnO in normal aqueous solution, no 1-D nanostructures could be found to grow out of the substrate. The initial ZnO grains in the seed layer were transversely developed to form a denser and more continuous film. Similar to the result shown in figure 2b, the top surface of the formed film in EG is very bumpy. Obviously, the developed film showed strong hindrance for the growth of ZnO along its inherent [0001] direction in the EG solution.
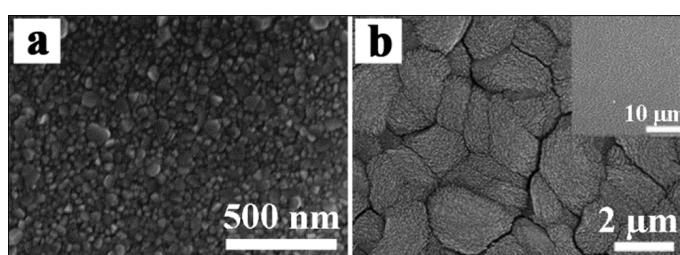

Figure 5. (a) SEM images of ZnO seed layer prepared by ALD and (b) the developed film formed after solvothermal growth. A low magnification image is shown in the inset.

Subsequently, a time-dependent morphological study was conducted to understand the nature of growth in the EG solvothermal process by using ZnO nanowires as the seeds. In this case, hydrothermally grown ZnO nanowires (figure 6a) were employed because these nanowire arrays were found to be more vertically aligned in the previous experiments. Primary-grown hydrothermal nanowires were kept in the nutrient solution for different time intervals (6 h, 15 h, and 24 h). It was observed that the nanowires became thicker after 6 hrs of growth (figure 6b). The surfaces of the nanowires are rougher compared to the primary ZnO nanowires (figure 6c). After 15 hrs the nanowires grew much thicker and started to fuse each other (figure 6d), which is clearly shown in the cross-section image of the sample (figure 6e). After 24 hrs the entire array of nanowires fused into a continuous film (figure 6f). During the whole evolution, there was no significant axial growth of ZnO nanowires observed in these samples. This result indicated that EG is an effective *c*-growth inhibitor for the growth of ZnO. Since EG has the same functional groups as the polymer PEG, it can be assumed that the structure-directing effect is due to the coordination abilities of its oxygen atoms with zinc ions in the ZnO (0001) plane, as previously revealed.[25]
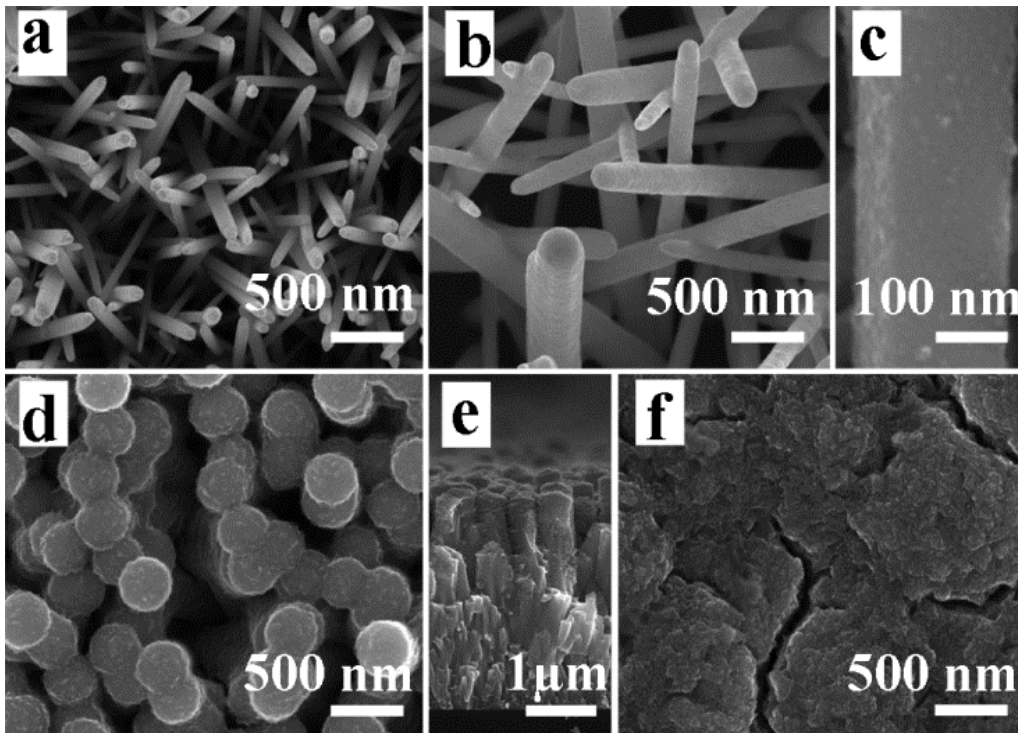
Figure 6: Time-dependent study of radial growth of ZnO NWs. (a) SEM image of ZnO NWs prepared by hydrothermal method. (b, d, f) SEM images of samples after 6 hrs, 15 hrs, and 24 hrs respectively. (c) A zoom-in view of surface of a NW after 6 hrs of growth. (e) Cross-sectional SEM image of NW array after 15 hours of growth.

The formation of the cylindrical morphology of ZnO nanowires during the secondary growth in EG is obviously independent on the presence of the cobalt precursor. Therefore, the radial and isotropic growth manner should be determined by EG and/or the higher temperature. In fact, the secondary growth of these nanowires in EG led to a cylindrical morphology with a bumpy surface even for a short time of 1 hr (figure 7), similar to the result shown in figure 3f. In contrast to the polymer PEG, EG is a much smaller molecule. When EG served as the solvent medium, abundant EG molecules could fill in all the growth space. It is reasonable to assume that, during the secondary growth in the EG-based process, EG molecules could not only hinder the growth of ZnO nanowires along the *c*-direction by the capping effect, but loosely adsorb on their sidewalls changing the activation energy for growth on the side wall. The layer-by-layer epitaxy of ZnO along the radial direction of the nanowire seeds might be disturbed while some ZnO clusters locally nucleated or attached in an oriented way on the ZnO sidewalls, both of which could be an explanation for the growth of individual whiskers around the side surface. The cylindrical morphology was thus formed

81

after sufficient evolution with bunches of whiskers in the radial direction. During this process, the released Co species were simultaneously incorporated into the growing whiskers and site-selective doping of Co was achieved. Due to the empty space among adjacent whiskers, the density of the shell is much lower than that of the core, as evidenced in figure 3a and 3b. Annealing the ZnO nanowires with a thick shell at 600 °C led to ripening of small whiskers, which converted the porous shell to a patchy crust.
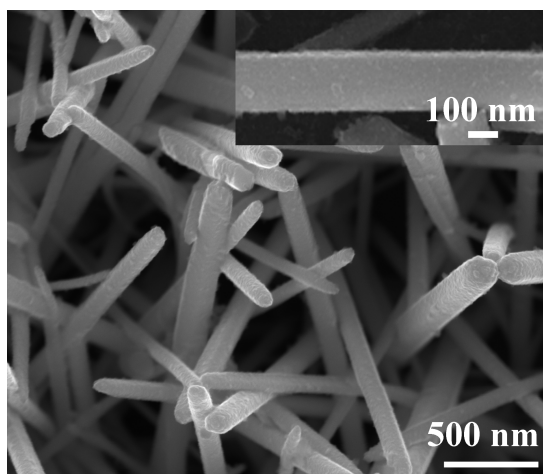

Figure 7. SEM image of ZnO nanowires after secondary growth in EG medium for 1 hour without the addition of the Co precursor. A magnified image of a nanowire is shown in the inset. Here, the primary ZnO nanowires were grown by the CBD method.

5.2.3 Magnetic Properties

The magnetization behavior of Co-doped core-shell NW array has been studied at 300 K and 70 K (figure 8) as a proof of concept experiment The measurements revealed that ZnO@CoZnO core-shell NW arrays exhibit a magnetic hysteresis at room temperature. In the literature, the causative factor for the magnetism in ZnO based systems other than the dopant is attributed to different effects such as zinc vacancies,[26] oxygen vacancies,[27] defect complexes,[28] anisotropic shape.[29]

To explain ferromagnetism observed in transition metal doped ZnO, there has been more than one theory proposed.[10,30–32] Nickel doped ZnO experiments strongly suggest the formation of a second phase in the structure.[30] According to this theory, ferromagnetism shown by Ni doped ZnO is not an intrinsic property of the material but results due to a strong tendency of Ni to precipitate out in the ZnO matrix. It is also shown that in films prepared by

pulsed laser deposition, the solubility of Ni in ZnO is very sensitive to the oxygen pressure during deposition. Samples prepared using low oxygen pressures undergo phase separation resulting in the precipitation of Ni metal clusters which in turn give rise to ferromagnetism[30]. In contrast, there are many reports suggesting that the ferromagnetism is an intrinsic property of the doped ZnO.[10,31,32] Considering the relatively greater extent of stability of the wurtzite form of CoO compared to that of NiO and magnitude of the driving force for phase separation shows that ZnO-CoO solid solutions are comparatively more stable. It has also been demonstrated that ZnO–CoO is not vulnerable to phase separation at concentrations of Co less than 25%-30%.[10,33,34] The saturation magnetization (*Ms*), remanence (*Mr*), and coercivity (*Hc*) of Co-doped ZnO core–shell nanowire array were found to be 5.7×10^{-5} emu, 1×10^{-5} emu, 42 Oe at 70 K whereas 8.7×10^{-5} emu, 1.3×10^{-5} emu, 246.3 Oe, were measured at 300 K. In the study, there were no cobalt metal clusters identified in the structure. This indicated that the magnetic behavior shown by the doped ZnO is an inherent property gained through doping. The magnetic saturation moment of the sample with the Co-doped ZnO shell decreases at low temperature and the hysteresis differs in the shape whereas at room temperature it shows a common hysteresis shape. In order to elucidate these properties and their dependence on temperature and Co composition, more careful studies are required.
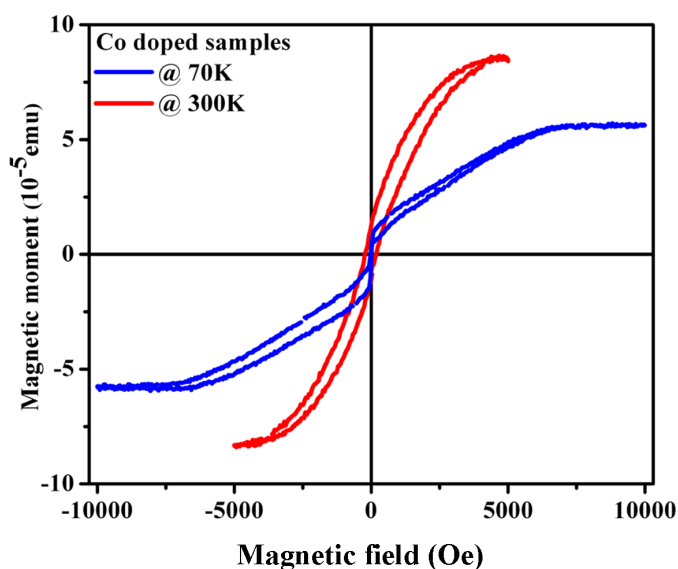

Figure 8: Magnetization behavior of Co-doped ZnO NW samples at 300 K. and at 70 K.

5.3 Summary

PEG-assisted method does not produce transition metal-doped ZnO due to rapid and exhaustive precipitation of dopant precursors in the aqueous medium. For avoiding such precipitation, a pathway using ethylene glycol medium at relatively higher temperature was developed for site-selective doping of other transition metal ions such as Co by secondary growth. In ethylene glycol medium the intrinsic growth propensity of ZnO along [0001] suffered strong hindrance due to capping, which is similar to the effect of PEG in aqueous solution. However, possibly due to adsorption of EG on the sidewalls of the primary ZnO nanowires, the epitaxial growth of ZnO in radial direction was disturbed during secondary growth. As a result, a whisker-like lateral growth mode occurred, accompanied with the incorporation of the Co dopants into the shell. In both cases, the site-selectivity of dopant distribution was confirmed by elemental mapping. Magnetizations of the samples were also presented to demonstrate successful doping. The proposed approach is compatible with the primary ZnO nanowires prepared both by CBD and CVD methods, which enriches the selection on the length, crystallinity, orientation and doping levels of ZnO nanowire cores for desired applications in electrical and spintronic devices.

5.4 References

[1]   R. Fiederling, M. Keim, G. Reuscher, W. Ossau, G. Schmidt, A. Waag, L. W. Molenkamp, *Nature* **1999**, *402*, 787.

[2]   Y. Ohno, D. Young, B. Beschoten, F. Matsukura, H. Ohno, D. D. Awschalom, *Nature* **1999**, *402*, 790.

[3]   T. Dietl, H. Ohno, F. Matsukura, J. Cibert, D. Ferrand, *Science* **2000**, *287*, 1019.

[4]   P. Sharma, A. Gupta, K. V Rao, F. J. Owens, R. Sharma, R. Ahuja, J. M. O. Guillen, B. Johansson, G. A. Gehring, *Nat. Mater.* **2003**, *2*, 673.

[5]   K. Sato, H. Katayama-Yoshida, *Phys. E* **2001**, *10*, 251.

[6]   K. Ueda, H. Tabata, T. Kawai, *Appl. Phys. Lett.* **2001**, *79*, 988.

[7]   D. C. Kundaliya, S. B. Ogale, S. E. Lofland, S. Dhar, C. J. Metting, S. R. Shinde, Z. Ma, B. Varughese, K. V Ramanujachary, L. Salamanca-Riba, T. Venkatesan, *Nat. Mater.* **2004**, *3*, 709.

[8]   J. H. Kim, H. Kim, D. Kim, Y. Ihm, W. K. Choo, *J. Eur. Ceram. Soc.* **2004**, *24*, 1847.

[9]   J. H. Park, M. G. Kim, H. M. Jang, S. Ryu, Y. M. Kim, *Appl. Phys. Lett.* **2004**, *84*, 1338.

[10]   H.-J. Lee, S.-Y. Jeong, C. R. Cho, C. H. Park, *Appl. Phys. Lett.* **2002**, *81*, 4020.

[11]   S. Han, D. Zhang, C. Zhou, *Appl. Phys. Lett.* **2006**, *88*, 133109.

[12]   Y. Q. Chang, D. B. Wang, X. H. Luo, X. Y. Xu, X. H. Chen, L. Li, C. P. Chen, R. M. Wang, J. Xu, D. P. Yu, *Appl. Phys. Lett.* **2003**, *83*, 4020.

[13]   J.-J. Wu, S.-C. Liu, M.-H. Yang, *Appl. Phys. Lett.* **2004**, *85*, 1027.

[14]   C. Ronning, P. X. Gao, Y. Ding, Z. L. Wang, D. Schwen, *Appl. Phys. Lett.* **2004**, *84*, 783.

[15]   S. Xu, Z. L. Wang, *Nano Res.* **2011**, *4*, 1013.

[16]   J. B. Cui, U. J. Gibson, *Appl. Phys. Lett.* **2005**, *87*, 133108.

[17]   J. Cui, U. J. Gibson, *J. Phys. Chem. B* **2005**, *109*, 22074.

[18]   W. Liang, B. D. Yuhas, P. Yang, *Nano Lett.* **2009**, *9*, 892.

[19]   B. D. Yuhas, D. O. Zitoun, P. J. Pauzauskie, R. He, P. Yang, *Angew. Chem.* **2006**, *118*, 434.

[20]   B. Panigrahy, M. Aslam, D. Bahadur, *J. Phys. Chem. C* **2010**, *114*, 11758.

[21] H. Wang, H. B. Wang, F. J. Yang, Y. Chen, C. Zhang, C. P. Yang, Q. Li, S. P. Wong, *Nanotechnology* **2006**, *17*, 4312.

[22] S. Ashoka, G. Nagaraju, C. N. Tharamani, G. T. Chandrappa, *Mater. Lett.* **2009**, *63*, 873.

[23] X. Jiang, Y. Wang, T. Herricks, Y. Xia, *J. Mater. Chem.* **2004**, *14*, 695.

[24] M. C. Biesinger, B. P. Payne, A. P. Grosvenor, L. W. M. Lau, A. R. Gerson, R. S. C. Smart, *Appl. Surf. Sci.* **2011**, *257*, 2717.

[25] R. Kozhummal, Y. Yang, F. Güder, A. Hartel, X. Lu, U. M. Küçükbayrak, A. Mateo-Alonso, M. Elwenspoek, M. Zacharias, *ACS Nano* **2012**, *6*, 7133.

[26] G. Z. Xing, Y. H. Lu, Y. F. Tian, J. B. Yi, C. C. Lim, Y. F. Li, G. P. Li, D. D. Wang, B. Yao, J. Ding, Y. P. Feng, T. Wu, *AIP Adv.* **2011**, *1*, 022152.

[27] T. Guo, Y. Zhang, Y. Luo, C.-W. Nan, Y.-H. Lin, *Mater. Lett.* **2013**, *108*, 273.

[28] C. Peng, Y. Liang, K. Wang, Y. Zhang, G. Zhao, Y. Wang, *J. Phys. Chem. C* **2012**, *116*, 9709.

[29] J.-I. Hong, J. Choi, S. S. Jang, J. Gu, Y. Chang, G. Wortman, R. L. Snyder, Z. L. Wang, *Nano Lett.* **2012**, *12*, 576.

[30] M. Snure, D. Kumar, A. Tiwari, *Appl. Phys. Lett.* **2009**, *94*, 012510.

[31] W. Yu, L. H. Yang, X. Y. Teng, J. C. Zhang, Z. C. Zhang, L. Zhang, G. S. Fu, *J. Appl. Phys.* **2008**, *103*, 093901.

[32] K. Kittilstved, D. Schwartz, A. Tuan, S. Heald, S. Chambers, D. Gamelin, *Phys. Rev. Lett.* **2006**, *97*, 037203.

[33] V. Jayaram, B. Sirisha Rani, *Mater. Sci. Eng. A* **2001**, *304-306*, 800.

[34] B. Loukya, D. S. Negi, K. Dileep, N. Kumar, J. Ghatak, R. Datta, *J. Magn. Magn. Mater.* **2013**, *345*, 159.

6 Antisolvent Crystallization of Copper (I) Iodide

This chapter describes a facile high-yield production of cuprous iodide (CuI) superstructures by antisolvent crystallization using acetonitrile/water as solvent/antisolvent couple under ambient conditions. In the presence of trace water, the metastable water droplets act as templates to induce the precipitation of hollow spherical CuI superstructures consisting of orderly aligned building blocks after drop coating. When water is used in excess in the mixed solution, an instant precipitation of CuI random aggregates takes place. This may be due to rapid crystal growth via ion-by-ion attachment induced by a strong antisolvent effect. Furthermore, the CuI superstructures have been applied both as a self-sacrificial template and as a structuring template for the flexible design of other porous materials such as CuO and TiO$_2$

6.1 Introduction

In the previous chapters structural engineering of a metal oxide semiconductor (ZnO) for different functionalities is discussed. In this chapter and the following one, structural studies of a metal halide semiconductor (copper (I) iodide) are focused. At present the research on halide semiconductors stands at the very beginning of semiconductor science and technology.[1] Cuprous iodide (copper (I) iodide, CuI) has been continuously studied over the last few decades with steadily increasing interest. Recently it draws great interest owing to the applications in organic electronics, solar cells, and bipolar diodes etc. General uses of CuI include their application as a catalyst in organic reactions, heat and light stabilizer in polyamide processing, photographic emulsions, and colorimetric detection of mercury. It is also used as a source of dietary iodine in table salt and animal feed, and as a double salt with mercury (II) iodide as a temperature indicator.[2–4]

6.1.1 Crystal Structure

Polymorphism of CuI, the existence in more than one form or crystal structure, has been investigated almost a century ago.[5] CuI is present in nature as mineral marshite (CuI). CuI adopts three crystalline phases namely α (rock salt structure), β (wurtzite structure), and γ (zinc blende structure). The transition temperatures of CuI are 369 °C (γ–β), 400 °C (β–α), and the melting point is 605 °C.[6,7] Even at room temperature, at high pressures the zincblende phase changes to rhombohedral structure at 1.4 GPa and further to tetragonal structure at 4 GPa. It is reported that further increase of pressure above 18 GPa leads to orthorhombic structure, contradicting earlier reports of a rocksalt phase.[8] Calculations based on the local density approximation (LDA) and experimental results show that CuI favors zincblende (γ-CuI) structure at normal conditions.[9]

6.1.2 Growth and Morphology

Generally, growth of zincblende single crystals from the melt is impossible due to the multi-phase nature of CuI. Growth of CuI crystals are carried out in various methods like sublimation, hydrothermal method, gel-based methods etc.[1,10–12] CuI thin films are mainly prepared using iodization reaction on copper films often deposited by sputtering.[1,13,14] The growth on highly oriented substrates leads to highly epitaxial growth and yields oriented CuI films.[15,16] Wet chemical routes are also available for growth of highly oriented γ-CuI films. An electrochemical strategy is reported by reduction of Cu(II)–ethylene diamine tetraacetic

acid disodium (EDTA) complex in presence of potassium iodide (KI) in aqueous solution at or near room temperature.[17] The preferential growth direction of γ-CuI is the [111] for most substrates.

CuI nanostructures with diverse features are produced by different methods. CuI crystallites have been deposited on indium tin oxide (ITO) substrates for photovoltaic applications. The deposition methods include glancing angle deposition and spraying solution of CuI in acetonitrile (CH_3CN).[18–20] Another strategy uses three steps, deposition of copper crystals, oxidation of copper to Cu_2O, and finally the conversion of Cu_2O to CuI using KI solution.[21,22]

Spherical CuI nanoparticles have been fabricated from $CuSO_4$ and KI-ethanol solutions.[23] CuI nanocrystals embedded in glass matrix have been presented and their quantum size effects were also investigated.[24] Aggregated CuI nanoparticles of about 20nm size have been synthesized by a single step chemical route at room temperature via iodization of copper sheet using a solution of iodine in ethanol under ultrasonication.[25] A similar sonochemical approach has also been reported using $CuSO_4$ as the Cu source, KI as the I source, and water as the solvent.[26] Using the successive ionic layer adsorption and reaction (SILAR) method, CuI nanostructures were deposited on Cu-tape/n-$CuInS_2$ substrates at room temperature.[27] This method used $CuSO_4$ as the cationic source, KI as the anionic source, and $Na_2S_2O_3$ as reducing and complexing agent. A similar SILAR approach has also been used to deposit CuI on glass and copper substrates. Irregular particles of CuI were formed on glass substrate, while arrays of cabbage-like tipped microrods were formed on copper substrate.[28] Single crystalline γ-CuI nanotetrahedra having four (111) facets have been obtained from the reaction between $CuSO_4$ and KI under ambient conditions.[29] In addition to the methods mentioned above, there are many reported methods used for fabrication of CuI with different morphology using structure directing agents, which will be discussed in *Chapter 7*.

6.1.3 Antisolvent Crystallization

In general, crystallization involves two processes; nucleation and growth. Nucleation is the formation of transition structures between solid and liquid phases at a concentration above equilibrium concentration (supersaturation). Supersaturation is the driving force for nucleation and subsequent crystal growth in a solution. Supersaturation can be achieved in the system using different methods like cooling, solvent evaporation, change of medium, and changing the solute by chemical reaction producing another substance with much lower

solubility etc. Antisolvent crystallization involves the changing the solubility of the medium by the addition of an antisolvent- a liquid miscible with the solvent which reduces solubility of solute in this new mixed solvent.[30] It is a simple, effective method for crystallization which can be done at ambient conditions. Even at a constant temperature, the size distribution and crystallinity of precipitated crystals can be controlled by this method. Additionally by adjusting the composition of solvent, a crystal form can be precipitated selectively in the cases that involve polymorphism.[31] This is a widely used method for separation and purification of pharmaceutical products.[32]

6.1.4 CuI Superstructures

Superstructures constructed by small nanocrystal units *via* bottom-up approaches are a new type of nanostructured matter with potentially inspiring applications, which have been intensively investigated in recent years.[33–42] The building blocks which are uniform in size and shape usually lead to the formation of nanocrystal superlattices with high crystallographic symmetry, analogous to the alignment of atoms or molecules in the classical crystallization process.[40–42] However, when the starting units are nonspherical and polydispersed, superstructures with plentiful intrinsic defects, for instance in the form of mesocrystal, are often constructed either as an intermediate or as the final product.[33,35,37,39] It has been generally acknowledged that organic additives can significantly influence the nucleation, evolution, and organized aggregation of such superstructures by altering the surface energies, controlling the interspaces, and regulating the orientational order of the adjacent nanocrystal building units. There exist a large amount of examples in the processes of biomineralization in nature, where specific organic–inorganic hybrid superstructures with complex morphologies and hierarchical order are presented. Therefore, optimal design of artificial superstructures has largely been conducted by introducing organic additives with specific functional groups during the synthesis of nanocrystal building blocks by mimicking the biomineralization process.[33–37,43–45]

Nevertheless, it has also been reported that organic additives are not always necessary for the construction of nanocrystal superstructures especially when a high orientation consistency among the building blocks does not become a major concern. One recent example is the formation of strontium sodium tantalite mesocrystals *via* an organic-additive-free molten salt process, where the molten salt restrains the further growth of the small building units and enhances their dipole field during the oriented aggregation process.[46]

Another encouraging example is the construction of superstructures consisting of hopper-like single crystals of sodium chloride exploiting metastable water droplets as the template by antisolvent crystallization.[47] This strategy proceeded almost in a "nonreactive" route, avoiding any harsh chemical reactions as well as related byproducts. However, due to the nature of alkali metal ions which are inert to most organic ligands, it is not realistic to further modify this system by introducing functional organic additives as structure-directing agents for tuning the organization of the building blocks.

Low temperature (below 390 °C) γ-phase CuI is an important p-type semiconducting binary metal halide with a large band gap of 3.1 eV. Synthesis of large single crystals,[48–50] high-quality thin films,[18,51–53] and low-dimensional nanostructures of CuI[29,54–59] has attracted much attention in recent years. However, so far the formation of CuI superstructures has not been reported. It is known that CuI is a water insoluble solid (pKsp = 11.96) at room temperature. In contrast, acetonitrile (CH_3CN) is a good solvent for the dissolution of CuI because acetonitrile can strongly solvate CuI leading to the formation of CuI–acetonitrile adducts. This is due to coordination of π* antibonding with nitrogen atoms of acetonitrile. Here, a facile and mild antisolvent crystallization approach for the construction of CuI superstructures by employing acetonitrile/water as a solvent/antisolvent couple is presented. It is demonstrated that the metastable water droplets can act as templates to form spherical CuI superstructures with orderly aligned building blocks under optimal conditions.

6.2. Results and Discussion

6.2.1 CuI Superstructures by Antisolvent Crystallization

The as-received commercial CuI powder is composed of random aggregates in a size range of several tens of micrometers. When the powder was dispersed in moisture-free acetonitrile in air (6.0 g/L, unsaturated), a transparent pale-yellow solution was formed. Drop coating this solution on a silicon substrate leads to the formation of microsized single-crystalline cubic CuI grains and some irregular aggregates, consistent with a previous report.[51] When 0.1 mL of water was added into 10 mL of the above CuI solution, polydispersed spherical particles with a hollow interior occurred through the same drop coating procedure, as shown in figure 1a. These hollow spheres with a "sink-hole" are very similar to particles obtained by a spray drying process,[60] indicating a significant effect of trace water on the morphology of the CuI product *via* solvent evaporation. Figure 1b shows a close view of an individual CuI hollow sphere, in which a highly wrinkled surface is

observed. Zooming on the unfolded areas of the surface, it is interesting to find that these flat areas are indeed composed of many small tetrahedral or truncated tetrahedral CuI building blocks with an average size of 80 nm (figure 1c and 1d). The tips of an array of CuI blocks face either outward (figure 1c) or inward (figure 1d) to the sphere surface. The arrangement in each array is very compact with narrow gaps. The corresponding sides of most building units are parallel, indicating the formation of CuI superstructures with a relatively long-range order.

It can be assumed that initially the solvation of CuI in the liquid film was hardly influenced by trace water because the acetonitrile was adequate. Relative to water, acetonitrile is easy to vaporize due to its lower boiling point and smaller specific heat capacity. Therefore, the solution film on the substrate was gradually dispersed into water-rich metastable droplets with the preferential evaporation of acetonitrile in the mixture. Once supersaturation was reached, homogeneous nucleation of CuI happened at multiple sites all over the droplet surface. Each CuI nucleus could continue to grow by sustainable supply of the CuI nutrient from the metastable water/acetonitrile droplets. After the remaining water in the center was finally vaporized, the CuI hollow spheres were formed.

CuI (γ-phase) has zinc blende-type cubic structure. Formation of tetrahedral nuclei with the zinc blende crystal structure is favored because the tetrahedral configuration exposes only close-packed {111} facets with the lowest surface energy.[29,53,57] Therefore, it is reasonable to form tetrahedral-shaped CuI crystals in the shell. The controlled alignment of tetrahedral-shaped CuI nanocrystals in the sphere shells was supposed to be favored by the air/droplet interface, which could provide an active platform to regulate the self-assembling behavior of the building blocks. However, the difference in boiling points and specific heat capacities of acetonitrile and water could induce different latent heat of evaporation and drying rates.[60] Therefore, the CuI shell was forced to fold during its growth for releasing the unbalanced stress, which led to the highly wrinkled surface. XRD measurements shown in figure 2 (blue curve) confirmed that the deposited solids were CuI with zinc blende-type cubic structure. No other crystallized impurities were detected.
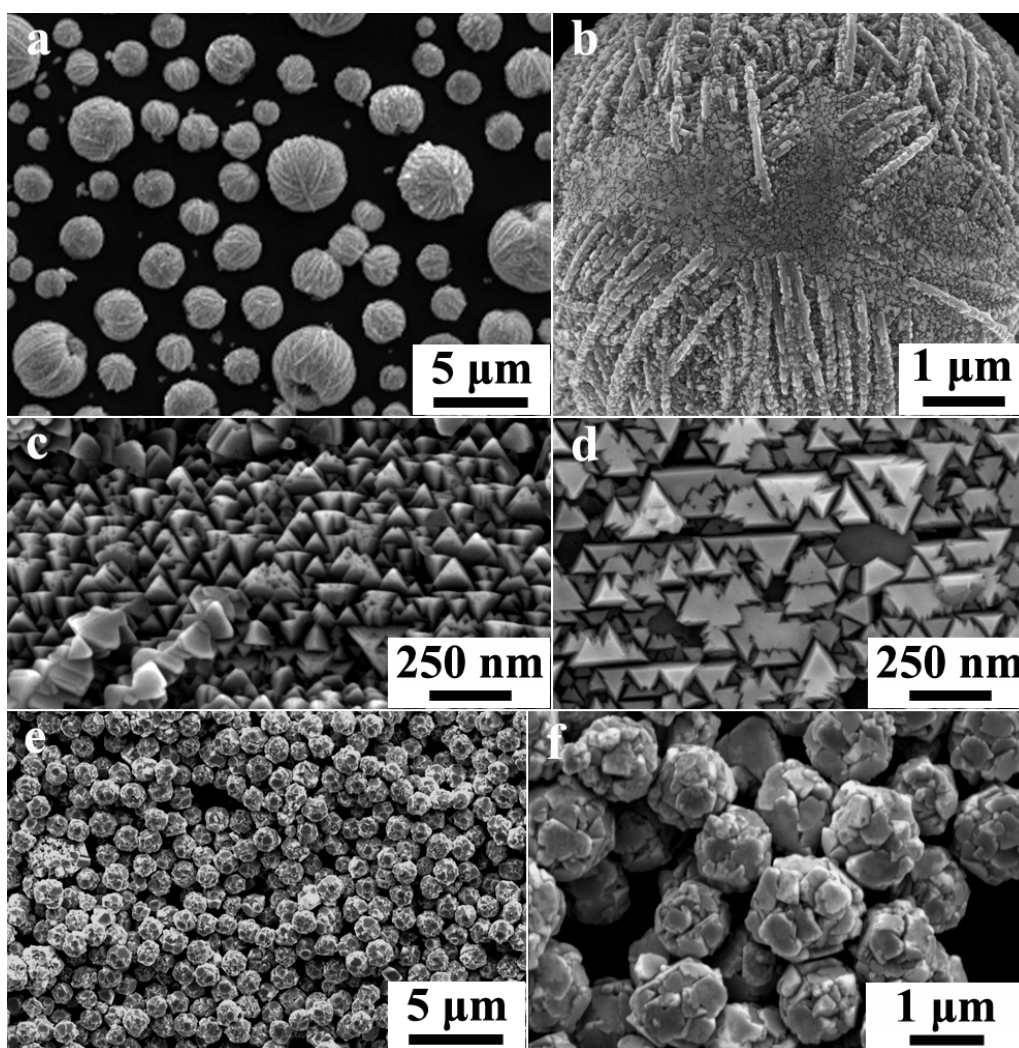
Figure 1: SEM images of (a) CuI microspheres obtained by drop coating of trace-water-added CuI-acetonitrile solution on silicon substrates at room temperature, (b) the surface of a single CuI sphere, and (c,d) zoomed surface areas. SEM images of CuI precipitates obtained by injecting excess water into the CuI-acetonitrile solution: (e) overview; (f) close view.

The morphologies of the final products were not altered when the concentration of CuI-acetonitrile solution was decreased to 3.0 g/L or increased to 12.0 g/L. Alternatively, when only 0.02 mL of water was added in 10 mL of 6.0 g/L CuI-acetonitrile solution, the similar wrinkled hollow spheres were exclusively obtained. Hence, the trace water could affect the deposition of the CuI film in a large component range. However, when 3 mL of water was rapidly injected into 1 mL of 6.0 g/L CuI-acetonitrile solution under vigorous stirring, a large amount of white precipitates instantly formed due to the strong antisolvent

effect of the excess water. Figure 1e shows a typical SEM image of the product, in which uniform spherical solids with an average size of 1 μm are presented. Each sphere is indeed an aggregate consisting of many irregular CuI crystals with different sizes, as clearly illustrated in figure 1f. Inverse injection of CuI-acetonitrile solution into the same amount of water led to a similar product.

The strong interaction between the water molecule and the acetonitrile molecule *via* hydrogen bonding would severely weaken the solvation of CuI when the CuI-acetonitrile solution was rapidly injected into sufficient pure water or inversely. The attainment of supersaturation of CuI in the mixed solvents led to homogeneous nucleation of CuI clusters in the solution because the supersaturated solution is not energetically stable. The tetrahedral nuclei quickly grew into large particles by an alternative arrangement of I^- ions and Cu^+ ion at the interface based on classical crystallization. Tens of large particles further randomly aggregate into one spherical structure for reducing the surface area and finally precipitated.
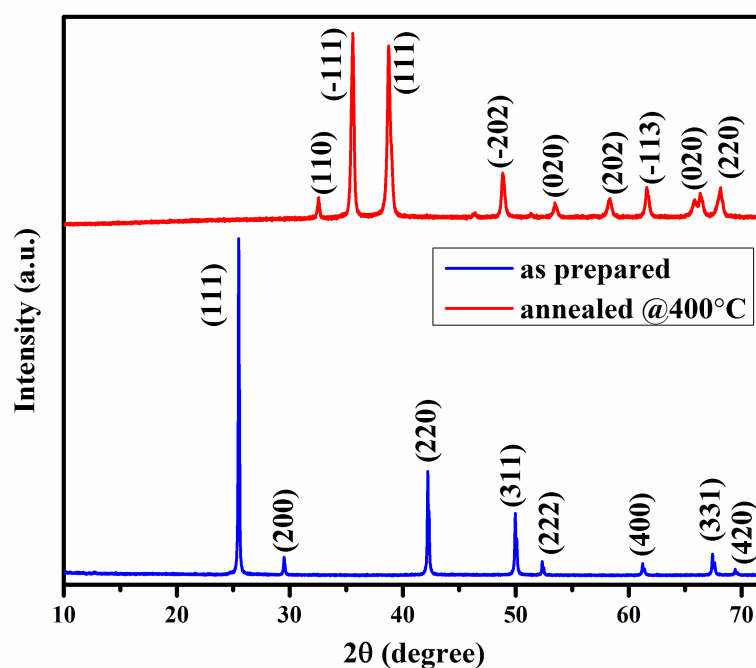

Figure 2: XRD patterns of sphere-like structures as prepared (blue curve) and after annealing (red curve).

6.2.2 CuI Superstructures as Templates

Exploiting the reactivity of CuI at high temperatures, the CuI superstructures can be further used as self-sacrificial templates for conversion to other copper-derived functional materials. For instance, when the sphere-like CuI superstructures shown in figure 1a were annealed in air at 400 °C for 1 h, highly porous CuO structures were formed, as exhibited in figure 3a and 3b. The XRD pattern shown in figure 2 (red curve) confirms the complete conversion of CuI into CuO.

Furthermore, it was revealed that the oxidation of each CuI building unit followed the nanoscale Kirkendall effect, by which a net outward flow of Cu^+ through the initially formed CuO shell could lead to an opposite transport of vacancies into the crystal interior, which would gradually condense into large voids.[29] The shell of the finally formed hollow CuO units was supposed to crack and dissociate into smaller subunits during the annealing at 400 °C. As evidenced in figure 3b, most CuO nanoparticle-aggregates on the surface of the CuO microspheres display the morphology of a tetrahedral cage, hence, maintaining the geometry of the initial CuI building blocks shown in figure 1c. For this reason, the CuO hierarchical structures consist of smaller blocks and became much more porous.

Additionally, the CuI superstructures were employed as templates for the deposition of titania (TiO_2) by ALD. In a typical experiment, a TiO_2 layer with a thickness of 15 nm was deposited. In virtue of the good solubility of CuI in acetonitrile, the CuI templates were easily etched by acetonitrile at room temperature. Figure 3c shows an SEM image of the obtained TiO_2 structure by using hollow sphere-like CuI superstructure as the template, followed by the removal of CuI. The rugged surface feature indicates a large surface area compatible with the template morphology. A close view in figure 3d confirms that each surface building unit has been conformally transformed into a hollow block due to the self-limiting surface reaction of ALD and the subsequent removal of CuI.[61]
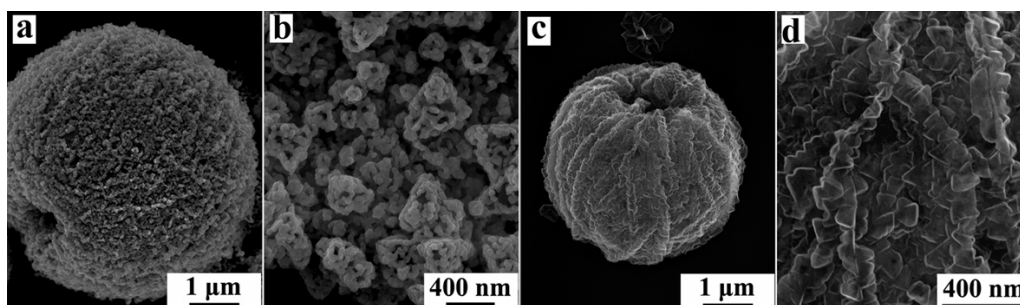
Figure 3: (a and b) SEM images of the CuO structures obtained by annealing the sphere-like CuI superstructures, (a) overview and (b) close view. (c and d) SEM images of the ALD-coated TiO$_2$ structures after CuI was etched away: (c) overview; (d) close view

6.3 Summary

CuI superstructures with spherical geometry were prepared using a simple antisolvent crystallization method. It is found that the presence of trace water can induce the formation of hollow sphere-like CuI superstructures by drop coating the CuI solution on a substrate. The gradually condensed metastable water droplets not only work as an antisolvent to help the precipitation of CuI nuclei with the evaporation of acetonitrile, but regulate their growth and arrangement at the droplet surface. For this reason, the finally formed sphere shells are composed of nanoscale tetrahedral CuI building blocks in an ordered alignment. When excess water is mixed with the CuI acetonitrile solution, spherical aggregates are instantly precipitated in the mixed solution due to the rapid growth of larger CuI crystals and subsequent random agglomeration. Superstructures were used as sacrificial and structural templates for the preparation of other functional materials with large surface area. The process has been carried out in mild and environmentally benign experimental conditions. Furthermore, the system gives a platform to design the geometry of the superstructure by introducing specific structure directing additives, which will be discussed in the next chapter.

6.4 References

[1]   M. Grundmann, F.-L. Schein, M. Lorenz, T. Böntgen, J. Lenzner, H. von Wenckstern, *Phys. Status Solidi* **2013**, 1.

[2]   S. Crisp, D. W. Meddle, J. M. Nunan, a. F. Smith, *Analyst* **1981**, *106*, 1318.

[3]   T. Harada, T. Iijima, *US Pat. 4,350,758* **1982**.

[4]   H Wayne Richardson, Copper Compounds. *Ullmann's Encycl. Ind. Chem. Electron. Release* **1998**, 69451.

[5]   P. . W. . Bridgman, *Proc. Am. Acad. Arts Sci.* **1916**, *52*, 91.

[6]   W. Bührer, W. Hälg, *Electrochim. Acta* **1977**, *22*, 701.

[7]   D. Keen, S. Hull, *J. Phys. Condens. Matter* **1995**, *7*, 1793.

[8]   M. Hofmann, S. Hull, D. Keen, *Phys. Rev. B* **1995**, *51*, 12022.

[9]   H. Hernández-Cocoletzi, G. H. Cocoletzi, J. F. Rivas-Silva, a. Flores, N. Takeuchi, *J. Nano Res.* **2009**, *5*, 25.

[10]   A. Armington, J. O'connor, *J. Cryst. Growth* **1968**, *3*, 367.

[11]   M. Gu, D. X. Wang, Y. T. Huang, R. Zhang, *Cryst. Res. Technol.* **2004**, *39*, 1104.

[12]   M. Gu, Y.-F. Li, X.-L. Liu, D.-X. Wang, R.-K. Xu, G.-W. Li, X.-P. Ou-Yang, *J. Cryst. Growth* **2006**, *292*, 74.

[13]   Y. Hayashi, H. Sasaki, T. Matsumnra, *US Pat. 3,677,816* **1972**.

[14]   K. Baedeker, *Ann. Phys.* **1909**, *334*, 566.

[15]   S. B. DiCenzo, *Appl. Phys. Lett.* **1982**, *40*, 888.

[16]   Z. Zheng, A. Liu, S. Wang, B. Huang, K. W. Wong, X. Zhang, S. K. Hark, W. M. Lau, *J. Mater. Chem.* **2008**, *18*, 852.

[17]   H. Kang, R. Liu, K. Chen, Y. Zheng, Z. Xu, *Electrochim. Acta* **2010**, *55*, 8121.

[18]   Y. Zhou, T. Taima, T. Miyadera, *Nano Lett.* **2012**, *12*, 4146.

[19]   M. N. Amalina, N. a. Rasheid, M. Rusop, *J. Nanomater.* **2012**, 1.

[20]   Y. Yan, S. Zhou, Z. Lu, Z. Li, *Rare Met.* **2011**, *30*, 22.

[21]   C.-T. Hsu, H.-H. Chung, A. S. Kumar, J.-M. Zen, *Electroanalysis* **2005**, *17*, 1822.

[22] G. S. Hsiao, M. G. Anderson, S. Gorer, D. Harris, R. M. Penner, *J. Am. Chem. Soc.* **1997**, *119*, 1439.

[23] H. T. Li, X. G. Li, *Inorg. Mater.* **2007**, *43*, 85.

[24] Y. Masumoto, K. Kawabata, T. Kawazoe, *Phys. Rev. B* **1995**, *52*, 7834.

[25] B. Sharma, M. K. Rabinal, *J. Alloys Compd.* **2013**, *556*, 198.

[26] A. Ziarati, J. Safaei-Ghomi, S. Rohani, *Ultrason. Sonochem.* **2013**, *20*, 1069.

[27] B. R. Sankapal, a. Ennaoui, T. Guminskaya, T. Dittrich, W. Bohne, J. Röhrich, E. Strub, M. C. Lux-Steiner, *Thin Solid Films* **2005**, *480-481*, 142.

[28] S. L. Dhere, S. S. Latthe, C. Kappenstein, S. K. Mukherjee, a. V. Rao, *Appl. Surf. Sci.* **2010**, *256*, 3967.

[29] C. Ng, W. Fan, *J. Phys. Chem. C* **2007**, 9166.

[30] M. Giulietti, A. Bernardo, In *Crystallization – Science and Technology*; Andreeta, M. R. B., Ed.; InTech, 2012; pp. 379–396.

[31] H. Takiyama, T. Minamisono, Y. Osada, M. Matsuoka, *Chem. Eng. Res. Des.* **2010**, *88*, 1242.

[32] R. A. Granberg, D. G. Bloch, Å. C. Rasmuson, *J. Cryst. Growth* **1999**, *198-199*, 1287.

[33] M. Antonietti, C. Göltner, *Angew. Chem.* **1997**, *36*, 910.

[34] Z. Tang, N. a Kotov, M. Giersig, *Science* **2002**, *297*, 237.

[35] H. Cölfen, M. Antonietti, *Angew. Chem.* **2005**, *44*, 5576.

[36] Z. Tang, Z. Zhang, Y. Wang, S. C. Glotzer, N. a Kotov, *Science* **2006**, *314*, 274.

[37] Q. Zhang, S.-J. Liu, S.-H. Yu, *J. Mater. Chem.* **2009**, *19*, 191.

[38] Y. Xia, T. D. Nguyen, M. Yang, B. Lee, A. Santos, P. Podsiadlo, Z. Tang, S. C. Glotzer, N. a Kotov, *Nat. Nanotechnol.* **2011**, *6*, 580.

[39] Y. Gao, Z. Tang, *Small* **2011**, *7*, 2133.

[40] a. L. Rogach, D. V. Talapin, E. V. Shevchenko, a. Kornowski, M. Haase, H. Weller, *Adv. Funct. Mater.* **2002**, *12*, 653.

[41] Y. Xia, Z. Tang, *Chem. Commun. (Camb).* **2012**, 6320.

[42] J. Gong, G. Li, Z. Tang, *Nano Today* **2012**, *7*, 564.

[43] S. Mann, D. Archibald, J. Didymus, *Science* **1993**, *1597*.

[44] J. F. Banfield, *Science* **2000**, *289*, 751.

[45] S.-H. Yu, H. Cölfen, K. Tauer, M. Antonietti, *Nat. Mater.* **2005**, *4*, 51.

[46] J. Sun, G. Chen, J. Pei, R. Jin, Q. Wang, X. Guang, *J. Mater. Chem.* **2012**, *22*, 5609.

[47] J. Zhang, S. Zhang, Z. Wang, Z. Zhang, S. Wang, S. Wang, *Angew. Chem.* **2011**, *50*, 6044.

[48] P. Gao, M. Gu, X. Lin-Liu, *Cryst. Res. Technol.* **2008**, *43*, 496.

[49] J. Pan, S. Yang, Y. Li, L. Han, X. Li, Y. Cui, *Cryst. Growth Des.* **2009**, *9*, 3825.

[50] D. Chen, Y. Wang, Z. Lin, J. Huang, X. Chen, D. Pan, F. Huang, *Cryst. Growth Des.* **2010**, *10*, 2057.

[51] P. . Sirimanne, M. Rusop, T. Shirata, T. Soga, T. Jimbo, *Mater. Chem. Phys.* **2003**, *80*, 461.

[52] Y. Yang, Q. Gao, *Langmuir* **2005**, *21*, 6866.

[53] X. Hu, J. Yu, J. Gong, Q. Li, *Cryst. Growth Des.* **2007**, *7*, 262.

[54] Y. Fujimori, Y. Gotoh, N. Tamaki, Y. Ohkoshi, M. Nagura, *J. Mater. Chem.* **2005**, *15*, 4816.

[55] Y. Yang, S. Liu, K. Kimura, *Chem. Lett.* **2005**, *34*, 902.

[56] X. Li, M. Wan, *Cryst. Growth Des.* **2006**, *6*, 2661.

[57] B. Zhang, A. Xie, Y. Shen, L. Yang, Y. Huang, J. Lu, *Eur. J. Inorg. Chem.* **2009**, *2009*, 1376.

[58] L. Meng, R. Mo, H. Zhou, G. Wang, W. Chen, D. Wang, Q. Peng, *Cryst. Growth Des.* **2010**, *10*, 3387.

[59] X. Wang, Y. Shen, A. Xie, L. Qiu, S. Li, Y. Wang, *J. Mater. Chem.* **2011**, *21*, 9641.

[60] R. Vehring, *Pharm. Res.* **2008**, *25*, 999.

[61] M. Knez, K. Nielsch, L. Niinistö, *Adv. Mater.* **2007**, *19*, 3425.

7 PVP-assisted Antisolvent Crystallization of CuI

In this chapter the process of superstructure formation of CuI by antisolvent crystallization is modified by adding polymer polyvinyl pyrrolidone (PVP) to get structures with designed morphologies. In this process PVP restricts the size of initially formed CuI crystal nuclei through effective coordination effect. CuI superstructures with a cuboid geometry are constructed by gradual self-assembly of the small CuI crystals via oriented attachment. The precipitated CuI superstructures have been used as a competent adsorbent to remove organic dyes from the water due to its mesocrystal feature. Similar to spherical superstructures described in the previous chapter, the CuI superstructures have been used as a self-sacrificial template and as a structuring template for the flexible design of CuO and TiO$_2$. This system together with the formation of spherical superstructures provides an ideal platform to simultaneously investigate the superstructure formation enforced by antisolvent crystallization with and without organic additives.

7.1 Introduction

Classical chemistry dealing with hierarchical construction of matter is about the connection of atoms and molecules into new functional units. But superstructures are formed by the connection of larger objects whose dimensions are measured in nanometers. Random arrangement of these structural units does not yield reproducible functionalities. Controlling the chemistry of the surfaces of each unit can lead to self assembly in 'mesoscopic' scale to form structures which can produce superior functionalities. This is often operated in the size regime 1-500 nm that bridges the gap between atoms and molecules on the one side and solid-state science on the other. In recent years structures thus constructed have been extensively investigated owing to their potentially inspiring applications.[1–10]

As described in the previous chapter, antisolvent precipitation of CuI produces structural units, which self assemble to form superstructures. Due to the coordination effect favored by the d^{10} electronic configuration of Cu (I), the antisolvent crystallization of CuI can be sufficiently modified by introducing specific organic additives for achieving CuI superstructures with other geometries. This system provides an ideal platform to simultaneously investigate the superstructure formation enforced by antisolvent crystallization, which will enhance our understanding on how to design functional superstructures with desired morphologies.

7.1.1 Structure-directing Agents

Organic additives have been combined with CuI for structural modifications and for novel resultant properties. A polyvinyl alcohol (PVA)-CuI nanocomposite electrolyte layer was synthesized *via* the reduction of $CuCl_2$ by NaI in an aqueous PVA solution. Hexagonal CuI nanoparticles were found embedded in the PVA matrix.[11] Cauliflower-like CuI nanostructures have been prepared by an ampicillin-assisted synthesis strategy at room temperature for catalytic and adsorbent applications.[12] Truncated tetrahedral CuI nanocrystals were synthesized by an ascorbic acid-assisted process for catalytic applications in organic coupling reactions.[13] Tetramethylethylenediamine (TMEDA) assisted route has been developed for the preparation of CuI thin films from nano-particles for dye sensitized solar cell (DSSC) applications.[14,15] Single crystalline γ-CuI nanosheets with (111) basal surfaces have been fabricated using polyethyleneglycol (PEG)-assisted aqueous solution approach at room temperature.[16] In addition to organic additives, inorganic functional templates have also been used to alter the growth behavior and morphology of CuI. Single

crystalline γ-CuI nano-crystals with diamond and platelet morphologies have been prepared using UV- irradiated 12-tungstosilicate anions ($[SiW_{12}O_{40}]^{5-}$).[17] Here tungstosilicate ions act as reducing agent for the reduction of Cu^{2+} in the solution containing $CuSO_4$ and KI.

7.2 Results and Discussion

7.2.1 PVP-Assisted Antisolvent Crystallization

Nitrogen-containing polymers such as PVP and PANI have been known as efficient matrices for the dispersion of CuI nanocrystallites.[18,19] The strong coordination effect between nitrogen atoms and Cu(I) ions can stabilize the crystallite surface, which is analogous to the solvation of CuI induced by acetonitrile. For investigating the effect of organic additives on the antisolvent crystallization of CuI, PVP aqueous solution instead of pure water is selected to mix with the CuI-acetonitrile solution. Shortly after 1 mL of CuI-acetonitrile solution (6.0 g/L) was injected into 3 mL of PVP aqueous solution (68.2 g/L) under vigorous magnetic stirring at room temperature, the mixed solution remained transparent. Colloidal precipitates gradually appeared about 30 min later under continuous stirring.

Figure 1a shows an SEM image of the collected deposits. Different from the precipitates by antisolvent crystallization in the absence of PVP, the current product exhibits the profile of a rodlike structure with various lengths and diameters. On the basis of the observation of figure 1b, it can be seen that most of the rods are well-defined with a cuboid shape. However, the surface of these faceted rods is not smooth and is full of hidden lines. Figure 1c presents another rodlike structure with a fracture section caused by the mechanical force. It is clear that both the exterior and the interior of the rod are composed of numerous nanoparticles. The external morphologies of the rod tips are either flat or truncated (figure 1d), implemented by the orientational alignment of small building units. The formation of the rodlike superstructures was not influenced by the injection sequence, injection speed, and solution temperature (examined up to 60 °C). However, the concentrations of both the PVP and CuI had a major effect on the final morphologies. When the concentration of the PVP aqueous solution was doubled, longer stirring time was required to make the precipitation happen, which accordingly led to a less amount of CuI rods with smaller diameters, as shown in figure 1e. When the concentration of CuI in acetonitrile was increased, the precipitation appeared much more quickly. The dominant morphology became a very regular planar rectangle (SEM image in figure 1f and its inset). The thickness of the sheetlike structure is

only 100 nm, while its width and length are up to several and tens of micrometers, respectively. Although the right angles and parallel sides are well-defined, the fabric of this sheet is also small nanoparticle building blocks. Therefore, all the precipitates with defined geometries obtained in the presence of PVP are not single crystals, but superstructures arranged by small nanoparticles.
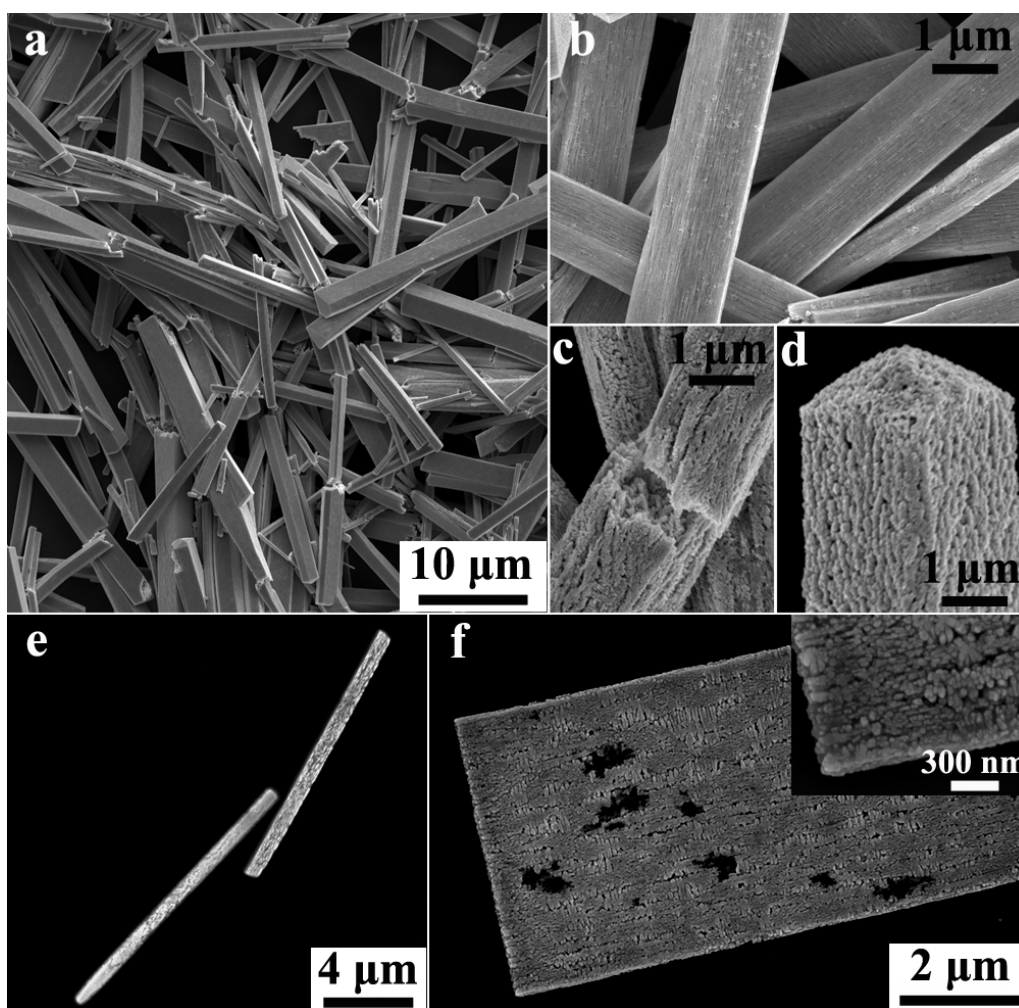

Figure 1: SEM images of rodlike CuI superstructures obtained by injecting 1 mL of CuI-acetonitrile (6.0 g/L) into 3 mL of PVP aqueous solution (68.2 g/L) through a syringe pinhole under vigorous magnetic stirring at room temperature: (a) overview; (b–d) close view on typical individual rods. (e) SEM image of rodlike CuI superstructures obtained by injecting 1 mL of CuI-acetonitrile (6.0 g/L) into 3 mL of PVP aqueous solution (136.4 g/L). (f) SEM images of sheet-like CuI superstructures obtained by injecting 1 mL of CuI-acetonitrile (12.0

g/L) into 3 mL of PVP aqueous solution (68.2 g/L). Inset is a magnified image of one corner of the structure.

A typical TEM image of the rodlike superstructure is shown in figure 2a. The surface of the rod is not crystallographically flat. The porous interiors could be revealed by the low contrast regions. The selected area electron diffraction (SAED) pattern for the entire rod in figure 2b dominantly shows cubic symmetrical diffraction spots corresponding to the zinc-blende phase of CuI. Although a detectable orientational distortion or scattering of the diffraction spots is demonstrated, this result confirms a high orientational order of the CuI subunits in the rodlike superstructure. The SAED pattern additionally shows that the elongation of the rod is along one 220 direction. This applies to all the rodlike structures during TEM observation. In combination with the cuboid shape based on the SEM investigation (figure 1b), the four side faces of the rod should be bound by two {001} and two {220} planes, as indicated by the diffraction pattern. When the electron beam was purposely focused on a small portion of the rod (figure 2c), interestingly the structure undergoes an obvious degradation. The stem slightly shrank while many tiny nanoparticles were released from the beam-focusing area. The halo-like SAED pattern shown in figure 2d evidence an amorphous phase of the residue after irradiation for 30 s by the focused electron beam. Foam-like pores are uniformly distributed throughout the remaining structure (figure 2d), which are most probably composed of the PVP matrix. This result straightly indicates that a certain amount of the organic additive was included in the CuI superstructures during antisolvent crystallization. The released species are very tiny Cu nanoparticles due to the decomposition of CuI into Cu solid and iodine vapor induced by the focused electron beam in the TEM chamber, which is confirmed by the TEM image and its corresponding SAED pattern presented in figure 2e.
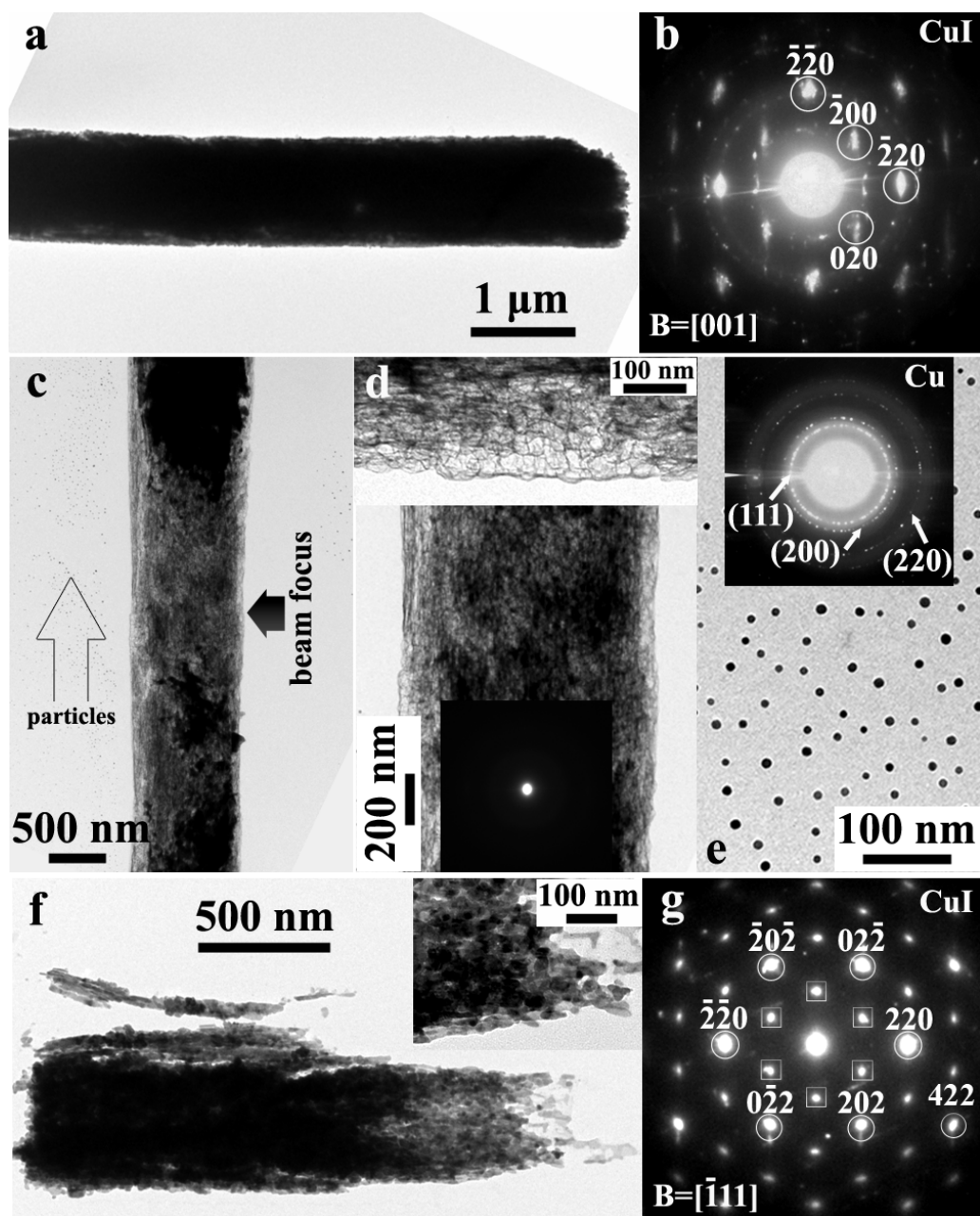
Figure 2: (a) TEM image and (b) corresponding SAED pattern of a rodlike CuI superstructure. (c) TEM image illustrating the irradiation of a focused electron beam on a selected portion after 30 s. (d) TEM images of the residual in the rod after beam irradiation. The inset is the SAED pattern of the bottom structure. (e) TEM image and corresponding SAED pattern (inset) of the released particles. (f) TEM image and (g) corresponding SAED pattern of a sheet-like CuI superstructure. The inset in panel f is a magnified view of its

thinnest area. The spots marked by the cubic frames in the SAED pattern correspond to 1/3{422} reflections.

Figure 2f shows a TEM image of a sheet-like superstructure with an imperfect appearance. Because the sheet-like structure is very thin, a better visualization of its internal configuration can be facilitated. It is found that some rod bundles partially merged into the sheet. A magnified region of the thinnest part of the sheet clearly reveals the brick-by-brick aggregation of small building units. The SAED pattern in figure 2g was obtained by aligning the electron beam perpendicular to the planar surface. The diffraction spots with a 6-fold rotational symmetry originate from the zinc-blende phase of CuI, which confirms the highly oriented alignment of the CuI nanoparticles in this sheet-like structure. The long side of the observed sheet-like structures is all elongated along one 220 direction (exemplified in figure 2g), agreeing with the rodlike superstructures. However, their flat top and bottom faces are always bound by two {111} planes. The existence of amplified 1/3{422} face-centered-cubic (FCC) reflections (marked by the cubic frames in figure 2g) indicates the possibility of the presence of multiple parallel twins on {111} planes parallel to the top and bottom surfaces of the lamellar structure.[20]

The {111} atomic planes of the tetrahedral CuI nuclei are polar, either negatively charged terminated by I^- ions or positively charged terminated by Cu^+ ions which are designated as the {222} planes. In the presence of polymer PVP, the {222} planes could be effectively stabilized due to the sufficient interaction between Cu^+ and the nitrogen atoms in PVP. Thus, the rapid growth of the critical crystal nuclei of CuI initiated by the antisolvent effect of water could be prevented. Moreover, the steric hindrance complied by the long-chain structure of PVP could retard the aggregation of these tiny CuI crystals. Therefore, after being mixed with the same volume of water, there were no immediate precipitates in the solution. With continuous vigorous stirring, these dispersed small blocks started to collide and fuse into each other. According to the surface energies associated with different crystallographic planes in the γ-phase CuI crystal lattice, the general sequence follows {111} < {100} < {110}. Therefore, these PVP-stabilized subunits could preferentially self-assemble along one 220 direction via oriented attachment possibly templated by PVP for minimizing the total free energy of the system.[21,22] The rodlike superstructures were gradually constructed and finally precipitated. Considering the random aggregates formed without PVP (*Chapter 6*, figure 1e and 1f), the formation of highly controlled alignment of CuI in the superstructures is greatly beneficial from the small sizes of the building units confined by

PVP because the larger the grain is, the harder the oriented attachment is.[22] However, smaller crystal nuclei obtained by further increasing the concentration of PVP became more soluble, which accordingly restricted the evolution of the CuI superstructures by organized aggregation (figure 1e). When the concentration of CuI was moderately increased, the coordination number of PVP at the rate-determining interfaces of the crystal nuclei was reduced, which led to the distribution of PVP more specific to certain planes. The 2-dimensional expansion based on the oriented attachment of the building blocks might become possible once an additional active plane was available. The sheet-like superstructures exhibited in our experiment hints that the oriented assembly also happened along one 422 direction in addition to the more preferred [220] direction in that case. A similar result was previously reported for the controlled dendritic growth of germanium with the FCC structure.[23] It was found that the principal surfaces of the long thin strips were bound to {111} crystallographic planes while the crystals grew rapidly in the [211] direction. The authors proposed that the presence of twin planes parallel to the flat surfaces was fundamental and necessary to this growth mode, which was expected to apply generally to materials with the zinc-blende structure.[23] Structural observations for the sheet-like superstructure (figure 2f and 2g) verify that this mechanism is still valid for the nonclassic crystallization of superstructures by organized aggregation.

The rodlike superstructures of CuI were stable at ambient conditions up to 6 months without any change of the geometries (figure 3a). The same stability was found after the CuI superstructures had been stored in water up to 3 months. However, when these structures were aged in the mother solution, a significant morphological transformation occurred within 72 h (figure 3b and 3c). The surface of all the rods became very rough, decorated with many small particles or platelets. The faceted feature of the rods almost faded away. From a thermodynamic point of view, the cuboid rodlike superstructures are not stable because they are enclosed by the exposed planes with a high surface energy. Upon extended ripening in the mother solution, surface subunits with a relatively high mobility started to reconstruct based on the dissolution–recrystallization process, which finally eliminated the high-energy surfaces. This result implies that the CuI superstructures with well-defined geometries are kinetic, metastable intermediates rather than thermodynamically stable products.
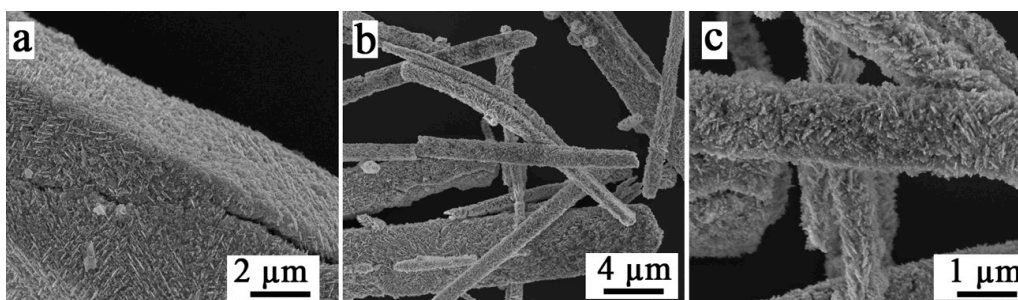
Figure 3: SEM images of samples after aging. (a) Close view of a rodlike structure kept at ambient conditions for 6 months. (b) Overview and (c) close view of rodlike structure kept in mother solution for 72 hours.

For further investigation of the generality of this polymer-assisted antisolvent crystallization approach, other organic additives were also examined for the fabrication of CuI superstructures. When 3 mL of Triton X-100 was mixed with 1 mL of the CuI-acetonitrile solution (6.0 g/L), spherical CuI aggregates consisting of randomly aligned crystals were quickly precipitated from the solution (figure 4a and 4b). Injection of 3 mL of PANI-isopropanol solution into the CuI-acetonitrile solution produced rodlike CuI superstructures after a long-time stirring, as shown in figure 4c. These rods are relatively shorter and thicker, but still very faceted with defined geometries (figure 4d). The above results demonstrate the necessity of using organic additives with nitrogen-containing functional groups for modifying the antisolvent crystallization of CuI from the acetonitrile solution.

110
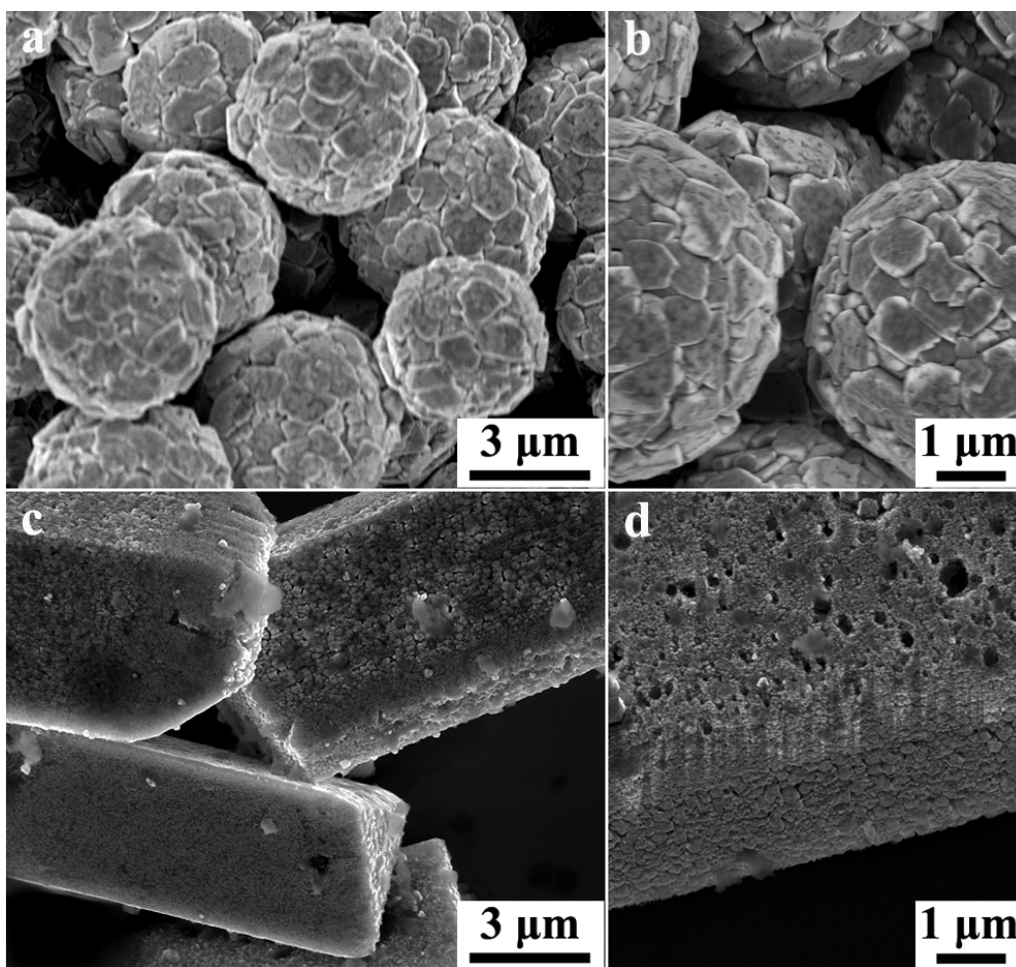
Figure 4: (a, b) SEM images of CuI precipitates obtained by mixing 3 mL of Triton X-100 with the CuI-acetonitrile solution: (a) overview; (b) close view. (c, d) SEM images of CuI precipitates obtained by injecting 3 mL of PANI isopropyl alcohol solution (1.4 g/L) into the CuI-acetonitrile solution: (c) overview; (d) close view.

7.2.2. Adsorption Experiments

The CuI superstructures have building blocks with polydispersed size distribution and surface defects. As a result there were spaces left among the particles even after their self-assembly into superstructures through lattice-matched surfaces.[24,25] Such an internal porous feature has been confirmed by our structural characterizations. For investigating the potential applications of the CuI porous superstructures in water treatment, the rodlike CuI superstructures induced by PVP and PANI (simplified as CuI-PVP and CuI-PANI, respectively) were used as adsorbents (10 mg) to remove the organic dye methylene blue (MB) (4 mL, 6.4 g/L) at room temperature. For comparison, the adsorption ability of the

equal mass of the as-received CuI powder was also examined under the same adsorbing conditions. The adsorption experiments were first performed at ambient conditions and then continued under UV irradiation to distinguish the contribution of CuI as a possible photocatalyst. Figure 5a outlines the adsorption curves of all the tested samples. It can be found that the adsorption percentage of the CuI-PVP reached to 83% after 30 min (also refer to the photograph in the inset), accompanied by the attainment of the adsorption/desorption equilibrium. CuI-PVP sample changed its colour from off-white to dark blue due to adsorption of MB (figure 5b). The removal efficiency of the CuI-PANI reached to 90% after 30 min, which was further increased to 97% up to 2 h. The presence of the as-received CuI powder hardly reduced the concentration of MB even after long-time UV irradiation, indicating the negligible effect of CuI for the photocatalytic degradation of MB.[26] A large surface area derived from the high porosity is thus believed to be responsible for the efficient removal of MB by the CuI superstructures.[27,28]
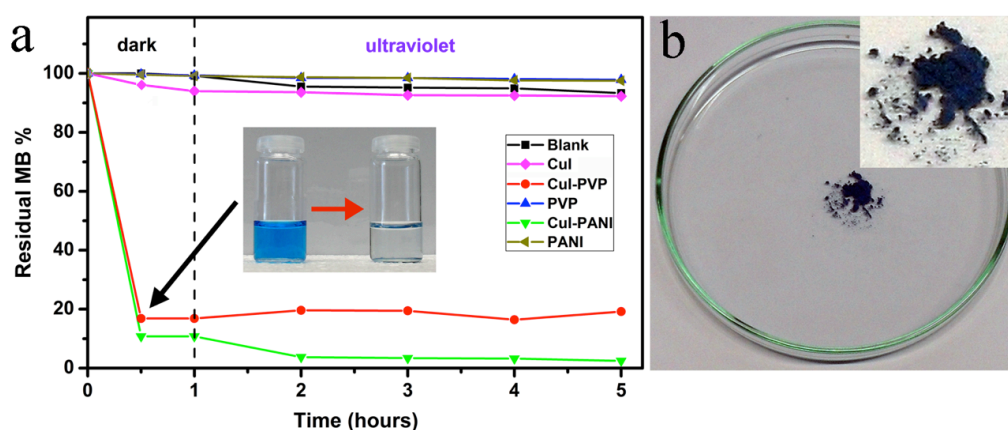
Figure 5: (a) Adsorption rate of an aqueous solution of MB (4 mL, 6.4 g/L) for CuI-PVP and CuI-PANI rods, and for the as-received CuI powder. The mass of each sample was 10 mg. The photograph in the inset shows the color change of the MB solution before and 30 min after the addition of the CuI–PVP rods. (b) CuI-PVP sample collected from the bottom of the vial after adsorption of MB.

7.2.3 Templating Experiments

Similar to the templating results using spherical CuI superstructures discussed in the previous chapter, analogous transformation happened for the rodlike CuI superstructures as

well (figure 6a and 6b). The resultant CuO structures inherited the geometries of the starting CuI structures throughout oxidation, but with higher porosities. The oxidation of CuI-PVP to CuO led to a significant mass loss, which provided more free spaces in the stacking structures.
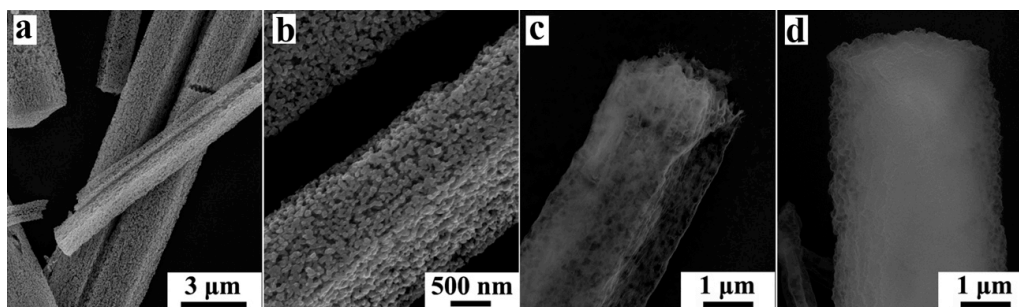

Figure 6: (a, b) SEM images of the CuO structures obtained by annealing the rodlike CuI superstructures, (a) overview, (b) close view, at 400 °C in air for 1 h. (c, d) SEM images of the ALD-coated TiO_2 structures subjected to the etching in acetonitrile at room temperature of the sphere-like: (c) overview; (d) close view. A total number of 1000 ALD cycles was applied at 150 °C for achieving the deposition of a TiO_2 layer with a thickness of 15 nm.

When the rodlike CuI superstructures were used as the template, similar replication was achieved. As clearly reflected in figure 6c and 6d, the rodlike TiO_2 structures are porous, presenting a hierarchical interior and a foam-like surface. An obvious advantage of this route lies in the easy, mild, and specific removal of the CuI templates only by the neutral organic solvent acetonitrile, which is expected to be a general templating strategy for the fabrication of many other porous materials, especially in combination with the ALD technique.[29]

7.3 Summary

In this chapter the formation of CuI superstructures by antisolvent crystallization with specific organic additives have been investigated. Unlike the cases discussed in the previous chapter, simultaneous antisolvent precipitation does not take place in the presence of organic additives such as PVP. The strong stabilizing effect of PVP on the initially formed CuI crystal nuclei can restrict the crystal growth *via* ion-by-ion attachment. Afterward, small CuI crystals with a confined size only behave like building blocks and gradually self-assemble into CuI superstructures by oriented attachment. The finally precipitated CuI superstructures in the majority are cuboid mesocrystals with a well-defined geometry, which could be tuned by the PVP concentration and the molar ratio of CuI relative to PVP. This antisolvent

crystallization approach is ideal to form CuI superstructures with tunable geometries in a single step with feasibility for large-scale production. Moreover, any harsh chemical reactions for the solidification of CuI crystals can be avoided by this route. A proof of concept experiment have shown that the formed CuI mesocrystals can be used as competent adsorbents for the fast removal of organic dyes in water due to their high porosity. The CuI superstructures can also be applied either as a self-sacrificial template or only as a structuring template for the flexible design of other functional porous materials. Such an antisolvent crystallization approach is expected to be a general strategy for constructing superstructures of many other ionic compounds containing a transition metal.

7.4 References

[1]   M. Antonietti, C. Göltner, *Angew. Chem.* **1997**, *36*, 910.

[2]   Z. Tang, N. a Kotov, M. Giersig, *Science* **2002**, *297*, 237.

[3]   H. Cölfen, M. Antonietti, *Angew. Chem.* **2005**, *44*, 5576.

[4]   Z. Tang, Z. Zhang, Y. Wang, S. C. Glotzer, N. a Kotov, *Science* **2006**, *314*, 274.

[5]   Q. Zhang, S.-J. Liu, S.-H. Yu, *J. Mater. Chem.* **2009**, *19*, 191.

[6]   Y. Xia, T. D. Nguyen, M. Yang, B. Lee, A. Santos, P. Podsiadlo, Z. Tang, S. C. Glotzer, N. a Kotov, *Nat. Nanotechnol.* **2011**, *6*, 580.

[7]   Y. Gao, Z. Tang, *Small* **2011**, *7*, 2133.

[8]   a. L. Rogach, D. V. Talapin, E. V. Shevchenko, a. Kornowski, M. Haase, H. Weller, *Adv. Funct. Mater.* **2002**, *12*, 653.

[9]   Y. Xia, Z. Tang, *Chem. Commun. (Camb).* **2012**, 6320.

[10]   J. Gong, G. Li, Z. Tang, *Nano Today* **2012**, *7*, 564.

[11]   E. Sheha, H. Khoder, T. S. Shanap, M. G. El-Shaarawy, M. K. El Mansy, *Optik (Stuttg).* **2012**, *123*, 1161.

[12]   Y. Jiang, S. Gao, Z. Li, X. Jia, Y. Chen, *Mater. Sci. Eng. B* **2011**, *176*, 1021.

[13]   S. Gao, Z. Li, X. Jia, K. Jiang, H. Zeng, *Green Chem.* **2010**, *12*, 1442.

[14]   a R. Zainun, M. H. Mamat, U. M. Noor, M. Rusop, *IOP Conf. Ser. Mater. Sci. Eng.* **2011**, *17*, 012009.

[15]   A. R. Zainun, U. M. Noor, M. Ruso, *Int. J. Phys. Sci.* **2011**, *6*, 3993.

[16]   Y. Xu, D. Chen, X. Jiao, L. Ba, *J. Phys. Chem. C* **2007**, *111*, 6.

[17]   B. Zhang, A. Xie, Y. Shen, L. Yang, Y. Huang, J. Lu, *Eur. J. Inorg. Chem.* **2009**, *2009*, 1376.

[18]   Y. Yang, S. Liu, K. Kimura, *Chem. Lett.* **2005**, *34*, 902.

[19]   X. Wang, Y. Shen, A. Xie, L. Qiu, S. Li, Y. Wang, *J. Mater. Chem.* **2011**, *21*, 9641.

[20]   a. I. Kirkland, D. a. Jefferson, D. G. Duff, P. P. Edwards, I. Gameson, B. F. G. Johnson, D. J. Smith, *Proc. R. Soc. A Math. Phys. Eng. Sci.* **1993**, *440*, 589.

[21]   R. L. Penn, *Science* **1998**, *281*, 969.

[22]   D. Li, M. H. Nielsen, J. R. I. Lee, C. Frandsen, J. F. Banfield, J. J. De Yoreo, *Science* **2012**, *336*, 1014.

[23]   A. Bennett, R. Longini, *Phys. Rev.* **1959**, *116*, 53.

[24]   H. R. Tan, J. Pei, Y. Tan, C. Boothroyd, T. W. Hansen, Y. L. Foo, M. Lin, E. Ruska-centrum, P. Gr, J. Forschungszentrum, *J. Phys. Chem. C* **2012**, 242.

[25]   H. Zhan, X. Yang, C. Wang, J. Chen, Y. Wen, C. Liang, H. F. Greer, M. Wu, W. Zhou, *Cryst. Growth Des.* **2012**, *12*, 1247.

[26]   B. Lv, C. Cheng, H. Yuan, D. Xiao, M. M. F. Choi, *J. Mater. Res.* **2011**, *23*, 1722.

[27]   J. Liu, Y. Wan, F. Meng, X. Huang, J. Liu, *J. Mater. Chem.* **2012**, *22*, 2885.

[28]   T. Zhai, S. Xie, X. Lu, L. Xiang, M. Yu, W. Li, C. Liang, C. Mo, F. Zeng, T. Luan, Y. Tong, *Langmuir* **2012**, *28*, 11078.

[29]   M. Knez, K. Nielsch, L. Niinistö, *Adv. Mater.* **2007**, *19*, 3425.

8

Conclusion and Outlook

In recent years the intensive research that has been focused to nanotechnology, generated new morphologies with novel properties. It is still essential to develop new methods for the fabrication of functional structures that can act as components in novel devices. The research on synthetic methods can lead to new novel structures and thereby helps to fully exploit the structure-related properties. As an active field in nanotechnology, the work presented in this thesis is mostly focused on the fundamental study about the fabrication of functional semiconductor nanostructures based on wet chemical methods.

In general the fabrications of novel functional structures using structure-directing agents are intrigued. Hydrothermal synthesis is an established method for preparation of ZnO nanowires. The method is modified using polymer additive, which has a huge impact on dictating the growth direction. It has been used for the growth of hexabranched ZnO structures with increased total/polar surface area. As demonstrated in *Chapter 3*, increased surface area has been exploited for improved photocatalytic activity of the nanostructure. The novel growth mode has also been attuned by adjusting the parameters and addition of specific impurities to use as a method for fabrication of core-shell structures. Thus Sb-doped core-shell nanowires have been synthesized by controlled radial growth process. Since this method used is based on radial secondary growth, good site-selectivity is achieved.

Apart from the hydrothermal growth of ZnO nanowires, the method is also extended toward structural tuning of CuI superstructures. Antisolvent crystallization and subsequent assembly of CuI nanosized units to superstructures has been demonstrated in *Chapter 6*. This process is again optimized using polymer additives to control the mode of assembly and thus to form structures with well-defined morphology. The porous nature of the structures has been exploited for improved adsorption ability. Making use of chemical nature of CuI and the highly convoluted structure of the superstructures, they

have been used as self-sacrificial templates for other functional structures like CuO and TiO$_2$.

This work presented in this thesis is only a preliminary study for the extended research for advanced applications in the future. The purview of this work is restricted on the fundamental study on the synthesis of the novel structures. The studies on the practical properties of the fabricated structures have not been done in this work. Therefore the follow-up studies should concentrate on the practical applications and device designs using these structures. As a start, solar cell fabrication using the hexabranched ZnO nanowires has been initiated.

Appendix 1

Fabrication of Micron-sized Silicon Tetrahedra

This part describes a new method to prepare micron-sized anisotropic-shaped particles: tetrahedral structures bounded by (111) faces. It is based on micromachining of (111)-oriented silicon wafers and retraction edge lithography (REL). The size of these Si structures is tunable but limited: roughly from 20 to 2000 nm. The importance of this method is that the fabricated structure resembles almost perfectly the mathematical tetrahedron. Furthermore, it is demonstrated the technique offers room to change the anisotropic property of the particle by selective modification of the faces using self-aligned lithography.

1 Introduction

Well-defined silicon structures bounded by (111) planes are important in micro system technology. They find applications in optical and electronic devices, sensors and MEMS.[1–3] The possibility of tetrahedral Si particles to assemble and form crystal structures has found to be intriguing, notably in simulation studies. In 2005, it has been shown that spherical particles with patches on the surface at the corners of a tetrahedron can form a diamond-like structure by self-assembly.[4] Simulations indicate that tetrahedra pack into quasicrystals with a high packing fraction.[5–7] Tetrahedral particles have been synthesized by bottom-up as well as top-down pathways. Chemically, by using a coordinating and capping ligand, Si tetrahedra were prepared bottom-up.[8] By contrast, Berenschot *et al.* reported a top-down method to machine single crystalline tetrahedral structures bound by Si (111) faces and outlined the prospected applications principally in self-assembly.[9] They described the preparation of tetrahedra in the range from 20 nm to 1000 nm. Here a new self-aligned strategy is presented, which facilitates a high degree in symmetry of the particle's shape. It uses Si (111) wafers and enables selective modification of the faces as will be demonstrated.

2 Fabrication Process

The strong anisotropy of etch rate among the crystallographic planes is well known in wet etching. For example, the Si etch rate in the (111) direction is much smaller than in the other directions for widely-used etchants like KOH, EDP (ethylene-diamine pyrocatechol) and TMAH (tetra-methyl-ammonium hydroxide).[10] This anisotropy is often used in the fabrication of structures in Si (100) wafers,[11–14] but in the present work Si (111) wafers will be used to fabricate tetrahedra. However, a process using photolithography to open a triangular shape along the (111) faces, followed by Si etching, typically would not form a tetrahedron. However, in the present study another method is adopted to preserve sharp corners in which the three out-of-wafer plane faces of the tetrahedron are formed in a three-step process one by one. Even though this technique increases the process complexity, the advantage is that the engineer has more freedom to design and change the property of individual faces of the tetrahedron. The latter might encourage the process of self-assembly.

Wet etching of Si (111) is generally concerned with the slow etch property of the (111) faces and as such will form hollow octahedral or parallelepiped features.[15–17] In the current technique, one corner of such a solid parallelepiped is machined into a tetrahedron. As shown in figure 1, the wafer surface itself forms the 1st face of the tetrahedron (ABC). The

2nd and 3rd (111) faces, ACD and ABD, are created sequentially by lithography and Si etching. After each stage, the newly opened Si (111) surface is protected with silicon dioxide (SiO$_2$). The 4th and last face, BCD, is made by a maskless lithographic technique called retraction edge lithography (REL), which is a perfect tool for fabricating wafer-scale nanostructures precisely and controllably.[18–21] In the coming sections, the exact procedure of above is described.
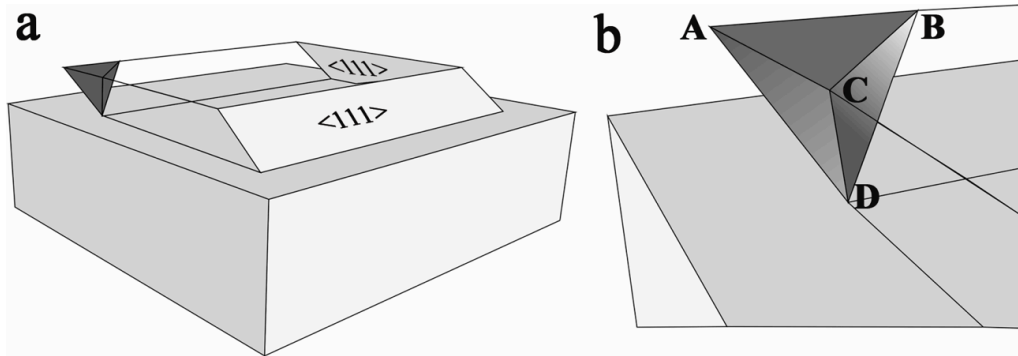
Figure 1: (a) Schematic representation of a tetrahedron bound by Si (111) facets machined out of a parallelepiped structure, which is machined out of a Si (111) wafer. (b) This zoom-in shows the four tips of the tetrahedron A, B, C and D. The plane described by the face ABC is part of the initial wafer surface.

2.1 Opening of the 2nd Face of the Tetrahedron

This process involves Si etching using KOH through a grating mask to reveal two parallel (111) surfaces: A wafer (100 mm diameter p-type Si (111), thickness 525μm±25μm) is dry oxidized at 950°C to grow 40 nm SiO$_2$. Subsequently, 70 nm of low-stress Si-rich nitride (SiN$_x$) is deposited by low pressure chemical vapor deposition (LPCVD). This double layer is patterned with photoresist using a grating mask (15μm line and 5 μm spacing) in a direction perpendicular to the wafer-flat, i.e. the grating is aligned with the (110)-direction. The nitride is etched by dry etching, the resist is stripped and the oxide is etched by buffered hydrofluoric acid (BHF 1:7) for 2 minutes to create a double mask on Si as depicted in figure 2a. Subsequently, the unprotected Si is etched for 180 minutes (25 wt% KOH at 75°C) reaching a depth of 2.6 μm to open two parallel Si (111) surfaces on both sides of the grating pattern (figure 2b).
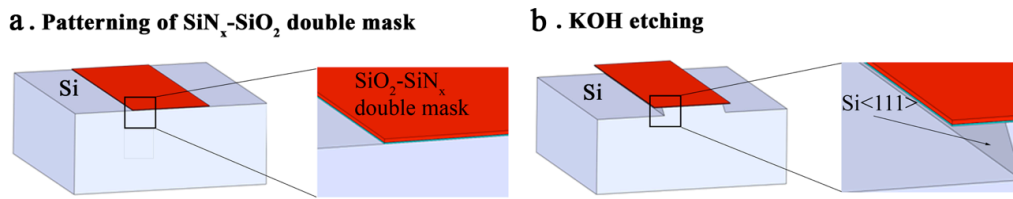
Figure 2: Schematic representation of opening the 2nd Si (111) face. (a) 70 nm nitride on top of 40 nm oxide is patterned resulting in a double mask. (b) Anisotropic KOH etching using the double mask opens up two Si (111) parallel planes.

2.2 Opening of the 3rd Face of the Tetrahedron

As shown in the process flow in figure 3, this step is to create a semi-parallelepiped structure bound by Si (111) faces: First, the KOH-patterned wafer of *section 2.1* is cleaned by RCA2 and dry oxidized at 1100°C to get 190 nm LOCOS protective oxide (LOCal Oxidation of Silicon) at the just revealed (111) planes (figure 3a). A layer of 100 nm LPCVD poly-silicon is deposited at 590°C (figure 3b) followed by wet oxidization at 800°C to grow 10 nm thin oxide on top of the poly-Si layer (figure 3c). Next, the same grating pattern as before is applied, but roughly 60° rotated with respect to the initial pattern. The process is not affected by misalignment of a few degrees and even more. This is because the anisotropic etch will force the shape to stop at the nearest (111) plane. When a mask edge is misaligned, instead of an atomically flat facet (at T=0), it leads to a train of steps like a staircase, where the surface of the step is atomically flat (111). Etching proceeds such that atoms are removed from the step edge, that means that the step moves.[22,23] There is also a small etch rate of the ledges of the step, but the edge is etching much faster. The features are etched quite deep, so that the steps due to misalignment had all time to move along the lateral length of the features, so the small misalignment has no influence on the result. After the development of the resist, the unprotected oxide on the poly-Si is etched by 1% HF (figure 3d). Note that the residual resist under the roofs of the undercuts protects this thin oxide too, because the poly-Si is opaque for the UV exposure. The resist is removed using acetone/isopropanol to prevent native oxide growth (figure 3e) and the poly-Si layer is etched by 25 wt% TMAH at 70°C for 25 seconds using the oxide pattern (figure 3f). The thin oxide on top of the poly-Si pattern is stripped (figure 3g) and the exposed double layer of nitride on top of oxide is etched by H_3PO_4 at 180°C and the oxide is etched in BHF (figure 3h,i). Next, the wafer is immersed in TMAH for 180 minutes to open the 3rd (111) face to reach a depth of 3.2 μm (figure 3j). TMAH is

chosen instead of KOH owing to its high selectivity to oxide.[24,25] This step also strips the poly-Si layer on top of the double layer.
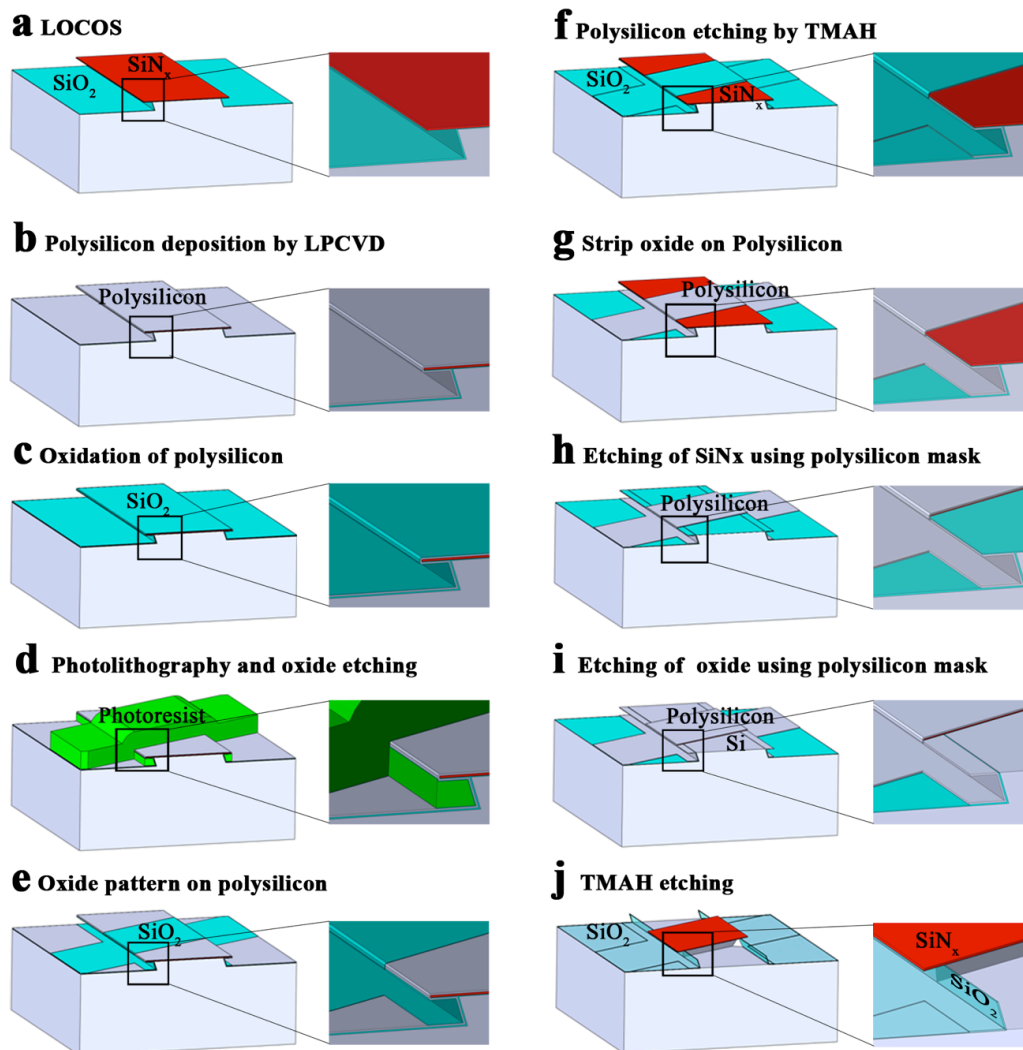

Figure 3: Schematic of the fabrication steps to reveal the 3rd (111) face of the tetrahedron. (a) Local oxidation of Si (LOCOS). (b) Conformal coating with LPCVD poly-Si. (c) Oxidation. (d) Resist pattern, roughly 60° rotated to the initial pattern, and subsequent oxide etch. (e) Resist strip. (f) Wet TMAH etch of poly-Si. (g) Oxide strip. (h) Nitride etch. (i) The 40 nm oxide is also removed using the same mask. (j) TMAH etch forms the 3rd face and it strips poly-Si.

2.3 Opening the 4th Face of the Tetrahedron: Retraction Edge Lithography (REL)

A straightforward method to form the 4th face, BCD, might be using lithography once again to open a part of the nitride mask at the top face of the parallelepiped. However, this method is not preferred for the fabrication of small accurate structures considering the resolution and precision of lithography. Therefore, REL has been adopted as described by Zhao *et al.*.[18] REL can overcome the need of an extra mask by using the already present double layer, i.e. undercutting the oxide beneath the nitride layer (figure 4 and figure 5a). In figure 4, the oxide pull-back underneath the edges is represented as X and θ is half the angle between two edges, i.e. 30 degrees. From the figure, $X= L \sin \theta$ giving $L=2X$. By varying the pull-back, the size of the tetrahedron formed can be tuned from ~20 to 2000 nm. The size can be scaled up, as long as the nitride overhang is mechanically stable. Note that the line roughness of the double layer, derived from the lithographic procedure, is virtually removed by the forming of the (111) planes. These almost perfect (111) planes are the starting point of the retraction etching.[26]
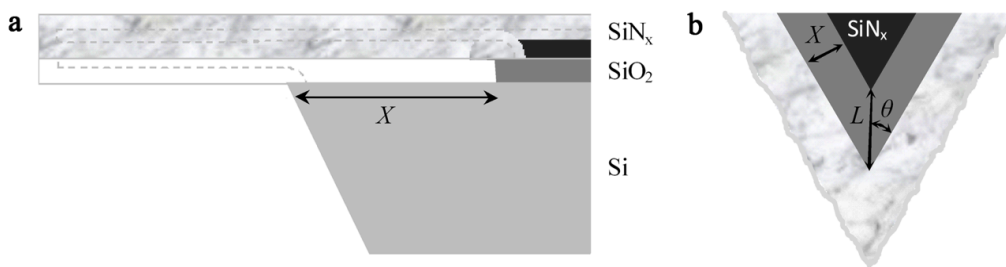
Figure 4: Top and cross sectional view of figure 5a: the corner after oxide REL with nitride overhang.

To start this sequence, the double layer is treated with 50% HF to retract the oxide layer below the nitride (figure 4 and 5a). The etch time is adjusted to 2 minutes for an oxide retraction of X~2.3 µm. The nitride is etched to slightly more than half of the thickness with H_3PO_4 for the shaping of the top nitride layer (figure 5b). The overhang is removed completely in this step since it is etched at top and bottom. The wafer is cleaned and Si is wet oxidized at 1100°C to grow 350 nm thick oxide (figure 5c). The native oxide on the nitride is removed with 1% HF and the nitride is etched with H_3PO_4 for 28 min. The 40 nm oxide from the double layer is then stripped with BHF for 50 seconds. This leaves the thicker oxide on the three faces of the corner virtually intact (figure 5d). Finally, the 4th and last (111) face is formed by etching with TMAH for 170 minutes to leave a tetrahedron at the tip of the

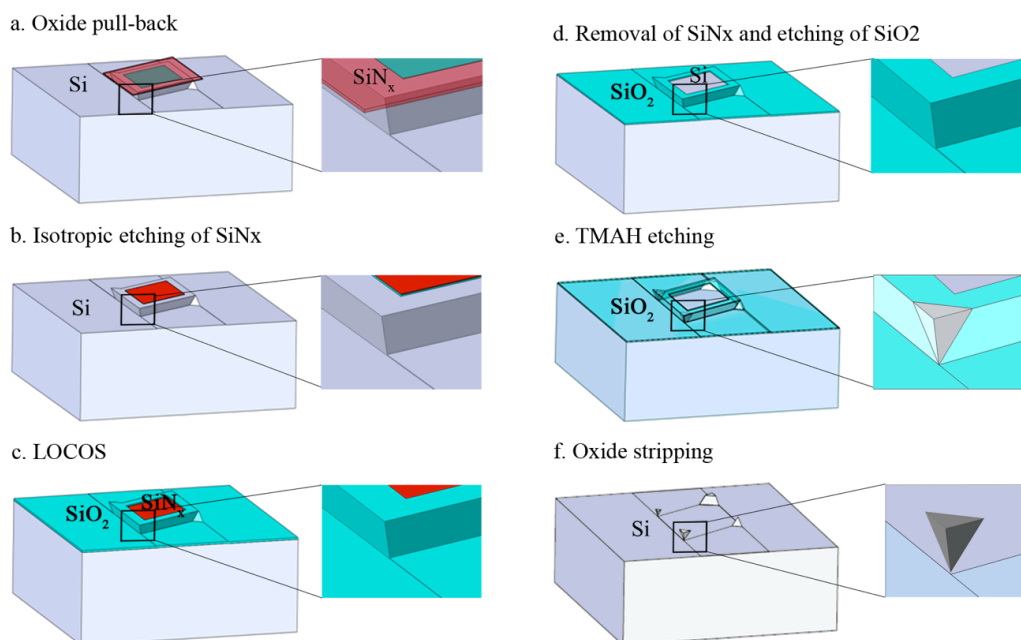parallelepiped (figure 5e). In order to free the tetrahedron, the oxide is etched with HF (figure 5f).

Figure 5: Schematic drawing of how to finish the tetrahedron out of the parallelepiped by REL. (a) Oxide retraction by HF. (b) Removal of the nitride overhang. (c) A thick oxide layer is grown. (d) The double layer is completely stripped leaving part of the thick oxide. (e) TMAH etch to get the 4th face of the tetrahedron. (f) Oxide strip releases the tetrahedron from the wafer.

2.4 Independent Patterning the 1st Face of the Tetrahedron: A Self-aligned Process

A big advantage of creating the faces of the tetrahedron one-by-one is that the faces can have different properties. This is an important feature in the process of self-assembly. In figure 6 the self-aligned patterning of the 1st face is demonstrated. The process description starts after shaping the final face of the tetrahedron (figure 5e and 6a). Structures with tetrahedral features of edge length 1.7μm are used for this patterning. The drawing is rotated and the tetrahedron is cut midways for clarity (figure 6b and 6c). To start with, the 4th face is protected with 20 nm dry oxide. The oxide on top of the tetrahedron is removed directionally with RIE (figure 6d)[27] and the unprotected Si is subsequently etched (100 nm in 5.5 min) by TMAH (figure 6e). Then, 136 nm of LPCVD nitride is conformally deposited (figure 6f) and partly etched for 41 min by H₃PO₄ using corner lithography[28] This leaves a nitride ring on

top of the Si structure (figure 6g). An additional TMAH etching through SiN_x opening results in a tetrahedron with a silicon ridge and a nitride ring on one of the faces (figure 6h). Both the structures (figure 6g and figure 6h) are released by etching with 50% HF for 1 min (figure 8a and 8b). Etching with 50% HF for longer time (15 min) strips off the nitride mask and forms modified silicon tetrahedral structures with ridge on top face (figure 6i and figure 8c).

A similar modification of the side BCD (figure 1) should be feasible since the side is open before release (figure 5f). Therefore, two different sides of the tetrahedral might be modified independently.
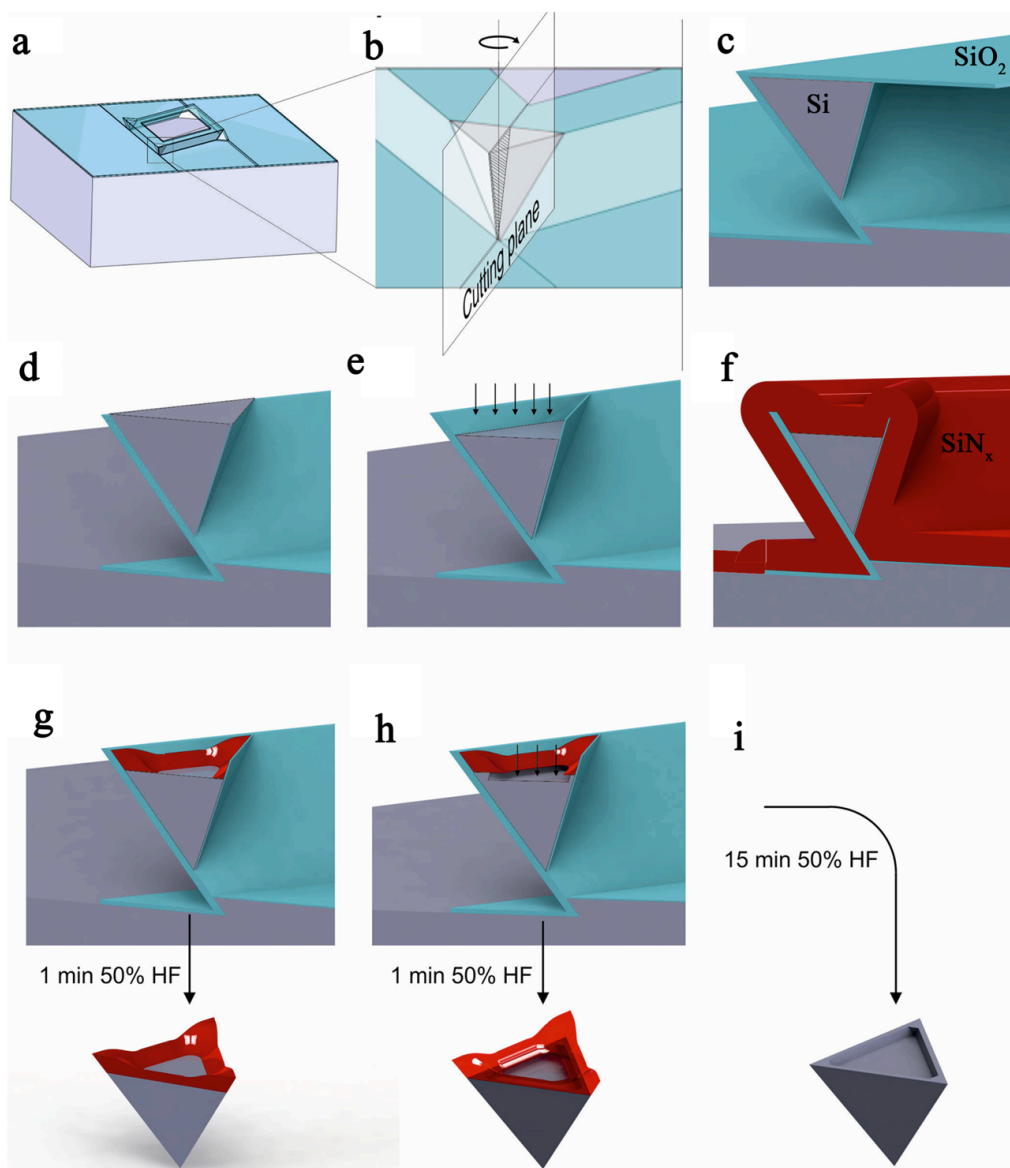
Figure 6: Self-aligned patterning of the 1st face of a tetrahedron: a-c) Rotation and zoom-in of figure.5e for clarity, d) RIE of oxide of top face, e) TMAH etching, f) LPCVD SiN$_x$ and g) Corner lithography of nitride. Subsequent etching in 50% HF for 1 min results in release of tetrahedron with a nitride ring is shown below. h) 2 min TMAH etching through the SiN$_x$ opening (40 nm deep). Tetrahedron releases after this step is shown below. i) Tetrahedron releases by etching with 50% HF for 15 min.

3 Results and Discussion

In the SEM image of figure 7a and 7b, at the corner marked as O, the tetrahedron is still protected by thick oxide. But, in the figures 7c and 7d, the tetrahedron is released by the HF. In addition to the intended tetrahedron some other structures are also produced. This includes a truncated pyramid (at the corner M), a pyramid at the corner N and a tetrahedron of smaller size at the corner P.
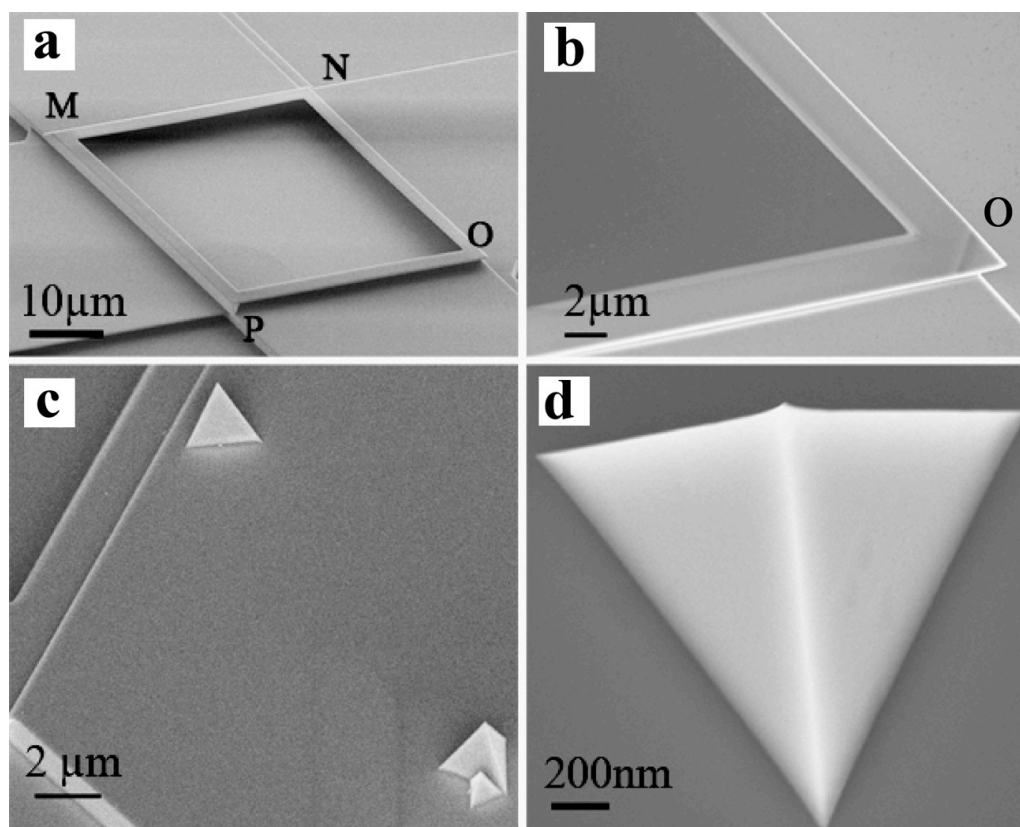
Figure 7: **(a)** SEM images of the final anisotropic structures. The tetrahedron is at the corner "O" of this structure. (b) Zoom in image of the O-corner showing the tetrahedron covered with oxide. (c, d) Tetrahedra released from the oxide frame after HF dip. A smaller

tetrahedron formed at the corner P is also observed along with the tetrahedron formed at the O-corner.
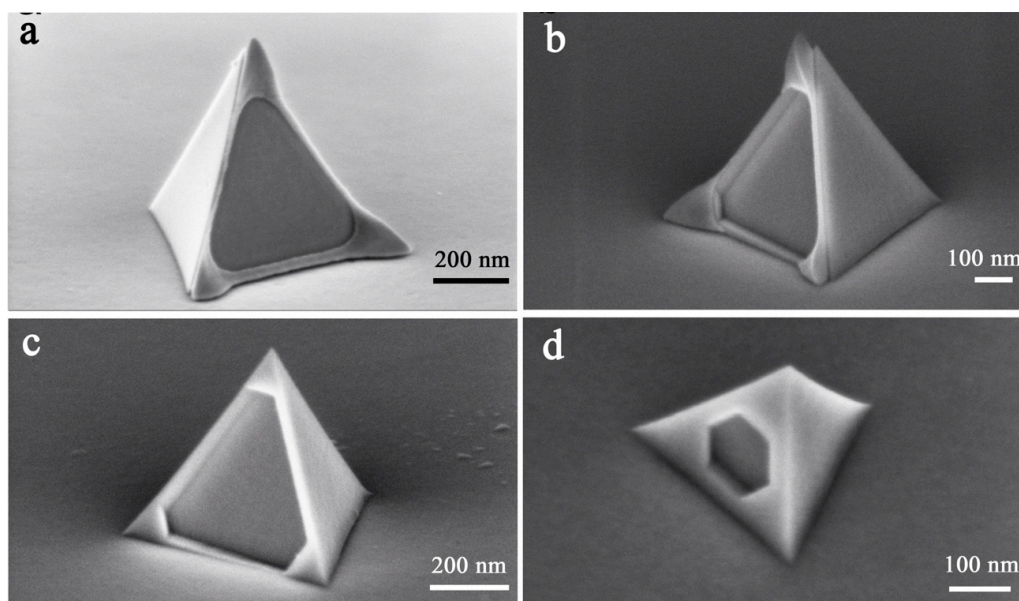

Figure 8: SEM images of tetrahedral structures after selective modification of top face. a) after release using HF but without an additional TMAH etch, b) after release while the 1st face is patterned in TMAH, c) the released structure of b after stripping the nitride mask d) structure released from the P-corner as marked as in figure 7, after stripping the nitride mask.

3.1 Effect of Oxidation Temperature on the Shape of Dry Oxidized Si (111) Convex Edges

Selection of an oxidation temperature, which hardly alters the morphology of the convex edge between (111) planes, is important in this process. The following experiment has been carried out: Test structures with convex (111) edges are prepared (figure 9a) by etching patterned (100)Si wafers as described by Berenschot *et al.*.[9] The samples have been dry oxidized at different temperatures between 950 and 1150°C to get around 50 nm oxide. 60 nm of LPCVD poly-Si is deposited to get a better contrast for SEM observation. As observed in figure 9, the convex shape varies with temperature. For 60 min at 950°C (figure 9b), a slightly sharpened Si edge after oxidation is formed. Successively less sharpening is observed for 40 min at 1000°C (figure 9c), for 24 min at 1050°C (figure 9d) and for 12 min at 1100°C (figure 9e). For 8.5 min at 1150°C the edge starts to round (figure 9f). It is concluded that 1100°C is the optimum temperature, which leaves the (110) ridge without excessive sharpening or rounding.
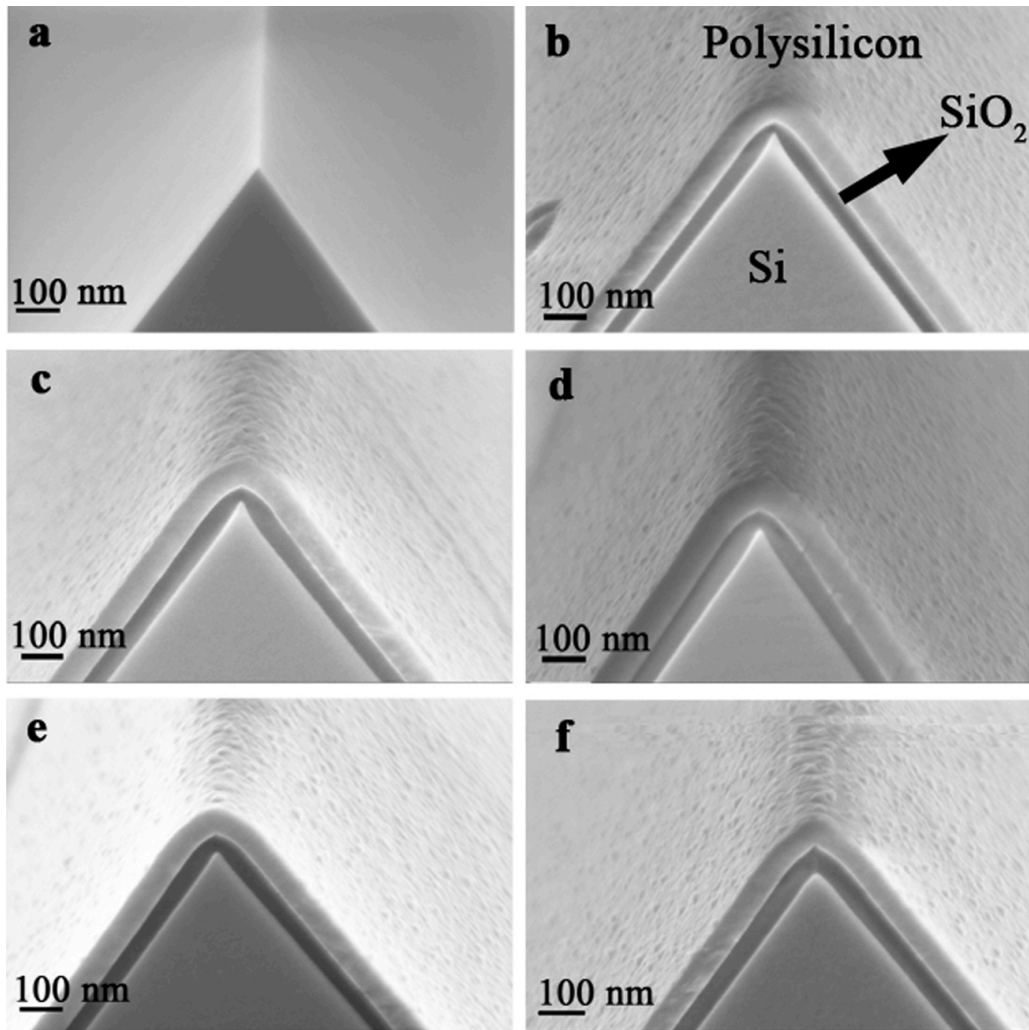
Figure 9: SEM images of the (111) ridges (a) before oxidation. (b) After dry oxidation at 950°C, (c) 1000°C, (d) 1050°C, (e) 1100°C, (f) and 1150°C.

Despite the former "optimized" result, the 350 nm LOCOS needed to reveal the last face does not lead to the mathematically correct tetrahedral shape. In the tetrahedron of figure 7d a slight sharpening can be observed at one of the tips, which it is not noticeable at the other tips. It is assumed that this imperfect tip is the A-tip as designated in figure 1b.

3.2 Uniformity

The size of the tetrahedra is controlled by two etch processes: The retraction length X in figure 4 and the etch rate of silicon in the (111) direction. The etch rate of silicon nitride in 50% HF is very close to 1.20 µm/min and according to microscopic inspection of the wafers quite homogeneous (the optical instrument limits the measurement of the retraction length to

130

about 100 nm; this is also the variation found in the measurements). The reproducibility of the Si (111) etch rate has not been systematically studied; the reducibility is within experimental errors. The uniformity of the process over a wafer is indicated in figure 8a–c: the specimens are from different parts of the wafer. They seem to be quite similar in size. The uniformity therefore is better than 5%.

4 Summary

In conclusion, silicon tetrahedral structures bound by (111) faces out of Si (111) wafers were fabricated. The special aspect of this process is that one of the tetrahedral faces is oriented parallel to the wafer surface. It is also shown that the side of the tetrahedron parallel to the wafer can be modified by corner lithography. Due to dependence of the thermal oxidation of silicon on stress the tetrahedra are not yet perfect: the tips tend to be slightly sharpened. The process yields tetrahedra of uniform size: the variation in size is less than 5%.

4 References

[1]   D. J. Sadler, M. J. Garter, C. H. Ahn, S. Koh, A. L. Cook, *J. Micromechanics Microengineering* **1997**, *7*, 263.

[2]   M. Trupke, F. Ramirez-Martinez, E. a. Curtis, J. P. Ashmore, S. Eriksson, E. a. Hinds, Z. Moktadir, C. Gollasch, M. Kraft, G. Vijaya Prakash, J. J. Baumberg, *Appl. Phys. Lett.* **2006**, *88*, 071116.

[3]   J. Kim, D. Cho, R. Muller, In *Proc. Transducers 2011: 11th Int. Conf. on Solid-State Sensors and Actuators*; Munich, Germany, 2001; Vol. 2, pp. 662–665.

[4]   Z. Zhang, A. S. A. Keys, T. Chen, S. S. C. Glotzer, *Langmuir* **2005**, *21*, 11547.

[5]   E. R. Chen, M. Engel, S. C. Glotzer, *Discrete Comput. Geom.* **2010**, *44*, 253.

[6]   P. Damasceno, M. Engel, S. Glotzer, *ACS Nano* **2011**, *6*, 609.

[7]   A. Haji-akbari, M. Engel, A. S. Keys, X. Zheng, R. G. Petschek, P. Palffy-muhoray, S. C. Glotzer, *Nature* **2009**, *462*, 773.

[8]   C. Barrett, C. Dickinson, S. Ahmed, *Nanotechnology* **2009**, *275605*.

[9]   J. W. Berenschot, N. R. Tas, H. V. Jansen, M. Elwenspoek, *Nanotechnology* **2009**, *20*, 475302.

[10]   M. Elwenspoek, H. V Jansen, *Silicon Micromachining*; Cambridge: Cambridge University Press, 1998.

[11]   C. Rusu, R. van't Oever, M. J. de Boer, H. V. Jansen, J. W. Berenschot, M. L. Bennink, J. S. Kanger, B. G. de Grooth, M. Elwenspoek, J. Greve, J. Brugger, a. van den Berg, *J. Microelectromechanical Syst.* **2001**, *10*, 238.

[12]   R. Holly, K. Hingerl, *Microelectron. Eng.* **2006**, *83*, 1430.

[13]   R. Holly, K. Hingerl, R. Merz, P. Hudek, *Microelectron. Eng.* **2007**, *84*, 1248.

[14]   E. Sarajlic, C. Yamahata, H. Fujita, *Microelectron. Eng.* **2007**, *84*, 1419.

[15]   M. Alavi, S. Büttgenbach, *Sensors Actuators A* **1992**, *32*, 299.

[16]   A. Tixier-Mita, Y. Mita, H. Fujita, In *TRANSDUCERS '03. 12th International Conference on Solid-State Sensors, Actuators and Microsystems.*; 2003; Vol. 1.

[17]   R. Oosterbroek, J. W. Berenschot, H. V. Jansen, A. J. Nijdam, G. Pandraud, A. van den Berg, M. C. Elwenspoek, *J. Microelectromechanical Syst.* **2000**, *9*, 390.

[18]   Y. Zhao, E. Berenschot, M. de Boer, H. Jansen, N. Tas, J. Huskens, M. Elwenspoek, *J. Micromechanics Microengineering* **2008**, *18*, 064013.

[19] Y. Zhao, E. Berenschot, H. Jansen, N. Tas, J. Huskens, M. Elwenspoek, *Microelectron. Eng.* **2009**, *86*, 832.

[20] Y. Zhao, E. Berenschot, H. Jansen, N. Tas, J. Huskens, M. Elwenspoek, *Nanotechnology* **2009**, *20*, 315305.

[21] Y. Zhao, H. Jansen, M. de Boer, E. Berenschot, D. Bouwes, M. Gironès, J. Huskens, N. Tas, *J. Micromechanics Microengineering* **2010**, *20*, 095022.

[22] P. Allongue, V. Costa-Kieling, H. Gerischer, *J. Electrochem. Soc.* **1993**, *140*, 1009.

[23] M. Elwenspoek, *J. Electrochem. Soc.* **1993**, *140*, 2075.

[24] U. Schnakenberg, W. Benecke, P. Lange, *TRANSDUCERS '91 1991 Int. Conf. Solid-State Sensors Actuators. Dig. Tech. Pap.* **1991**.

[25] O. Tabata, R. Asahi, H. Funabashi, K. Shimaoka, S. Sugiyama, *Sensors Actuators A* **1992**, *34*, 51.

[26] W. W. Koelmans, T. Peters, E. Berenschot, M. J. de Boer, M. H. Siekman, L. Abelmann, *Nanotechnology* **2012**, *23*, 135301.

[27] H. V Jansen, M. J. de Boer, S. Unnikrishnan, M. C. Louwerse, M. C. Elwenspoek, *J. Micromechanics Microengineering* **2009**, *19*, 033001.

[28] E. Berenschot, N. R. Tas, H. V. Jansen, M. Elwenspoek, *2008 3rd IEEE Int. Conf. Nano/Micro Eng. Mol. Syst.* **2008**.

Appendix 2

Experimental Details

This appendix gives additional experimental details. The description of experimental procedure and characterization methods that counts for all chapters is given under the general experimental details. Specific experimental details for each chapter are also given below.

1. General Experimental Details

1.1 Materials

Zinc nitrate hexahydrate ($Zn(NO_3)_2.6H_2O$), hexamethylenetetramine ($C_6H_{12}N_4$, HMTA), methylene blue ($C_{16}H_{18}N_3SCl$), polyethylene glycol (PEG, M_w 400), methylene blue ($C_{16}H_{18}N_3SCl$), sodium hydroxide (NaOH), ethylene glycol, glycolic acid ($C_2H_4O_3$), antimony acetate (($CH_3CO_2)_3Sb$), cobalt nitrate hexahydrate ($Co(NO_3)_2.6H_2O$), cuprous iodide (CuI), polyvinyl pyrrolidone (PVP, average M_W ~58000), polyaniline (emeraldine base) (PANI, average M_w ~50,000), Triton™ X-100, methylene blue (MB, $C_{16}H_{18}N_3SCl$), and acetonitrile (CH_3CN, 99.8%) were all analytical-grade reagents procured from Sigma Aldrich and used without further purification. Deionized water was used to prepare all the aqueous solutions throughout the experiments described in this book.

1.2 Preparation Methods

1.2.1 Preparation of ZnO Seed Layers by Atomic Layer Deposition (ALD)

ZnO thin film was grown at 115°C by reacting diethylzinc with water vapor in a vertical flow type reactor (OpAL, Oxford Instruments) at pressures between 80 and 180 mTorr. Nitrogen gas was used as the carrier gas with a flow rate of 25 sccm.

1.2.2 Hydrothermal Synthesis of ZnO Nanowires

Nanowires were prepared by the classic method. 15 mL of 12.5 mM solution of zinc nitrate and HMTA was contained in a glass tube. A piece of silicon (30 mm × 5mm) with annealed ZnO ALD layer was inserted into the solution in slanting manner facing the seed layer downward. The bottle was sealed and kept at 90°C for 24 hours. After 24 hours the

solution was cooled down and the sample was washed with deionized (DI) water and dried naturally.

1.2.3 Synthesis of ZnO Nanowires by Chemical Vapour Deposition (CVD)

Nanowires arrays have been grown on Si substrate with Au as catalyst in a two-zone furnace. The substrate was prepared by evaporating a film of Au catalyst on a piece of silicon wafer. Au coated substrate was placed inside the quartz tube at the downstream position in the first heating zone of the furnace. 1 g of ZnO powder (99.999%) and powdered graphite (99.99%) mixed in 1:1 ratio was placed in the second heating zone of the furnace. The tube was evacuated until a pressure of 4×10^{-5} mbar is achieved. Then oxygen gas and argon gas were set to flow through the tube at flow rates of 1.5 and 30 sccm, respectively. The temperature of the first heating zone was kept at 750°C and that of the second zone at 950 °C. The heating was continued for 1 hr. The tube was cooled naturally, the vacuum was released, and the sample was taken out of the furnace.

1.2.4 Templating Experiments with CuI Superstructures

For the conversion of CuI to CuO, CuI superstructures collected on silicon substrates were annealed in air in an open furnace at 400 °C for 1 h. For the application of CuI superstructures as templates for atomic layer deposition (ALD) of TiO_2, the deposition were conducted at 150 °C by reacting titanium isopropoxide with water vapor in a vertical flow type hot wall reactor (OpAL, Oxford Instruments). N_2 was used as the carrier gas with a flow rate of 100 sccm for this process. A total number of 1000 ALD cycles was applied for achieving the deposition of a TiO_2 layer with a thickness of 15 nm. The TiO_2-coated samples were dipped into acetonitrile for 5 min at room temperature to remove the CuI and then dried in air.

1.3 Characterization

1.3.1 Scanning Electron Microscopy (SEM)

The surface morphology of the structures was examined using a FEI Nova NanoSEM scanning electron microscope (SEM). Everhart-Thornley detector (ETD, routine imaging) or through-the-lens detector (TLD, high magnification/resolution imaging) was employed using an accelerating voltage of 10 kV with a working distance of about 5.0 mm.

1.3.2 Transmission Electron Microscopy (TEM)

TEM images of the ZnO nanostructures and the corresponding ED pattern were obtained by using JEOL 1010 microscope at an accelerating voltage of 100 kV. The nanostructures were scratched from the Si substrate, dispersed in ethanol (analytically pure, 99.99%), dip-coated onto a copper grid coated with thin carbon film, and dried at room temperature.

1.3.3 High Resolution TEM (HRTEM)

High resolution TEM analysis was made using an image corrected FEI Titan 80-300 microscope operated at 300 kV and equipped with a Gatan US1000 CCD camera for TEM imaging and electron diffraction. STEM images were obtained using a HAADF (high angle annular dark field) detector with a nominal spot size of 0.14 nm. EDX analysis and elemental mapping were performed in STEM mode with a nominal spot size of 0.5 nm using an EDAX S-UTW EDX detector. The ZnO nanostructures were scratched from the silicon substrate, dispersed in isopropanol (analytically pure, 99.99%), drop-casted onto copper grids (Quantifoil holey carbon grids coated with a 2 nm thickness carbon layer), and dried at room temperature.

1.3.4 X-ray Diffraction Spectroscopy (XRD)

Crystal structure was characterized by XRD theta–2theta scans using a Philips X'Pert MRD diffractometer with CuKα radiation.

1.3.5 X-ray Photoelectron Spectroscopy (XPS)

XPS measurements were performed using a K-Alpha XPS spectrometer (ThermoFisher Scientific, East Grinstead, UK). Data acquisition and processing were done using Thermo Avantage software. All samples were analyzed using a microfocused, monochromated Al K_α X-ray source (400 µm spot size). The K-Alpha charge compensation system was employed during analysis, using electrons of 8 eV energy, and low-energy argon ions to prevent any localized charge build-up. The spectra were fitted with one or more Voigt profiles (BE uncertainty: $\pm$0.2eV) and Scofield sensitivity factors were applied for quantification. All spectra were referenced to the C1s peak assumed to originate from surface hydrocarbon contamination at 285.0 eV binding energy controlled by means of the well-known photoelectron peaks of metallic Cu, Ag, and Au, respectively.

1.3.6 Magnetic Measurements

Magnetization of the Nanowire arrays has been studied at 300 K and 70 K using a Quantum Design Dynacool Vibrating Sample Magnetometer. Hysteresis curves have been recorded starting from the saturated state at 5 kOe or 10 kOe, respectively.

2. Chapter 2

2.1 Fabrication of Patterned ZnO Dot Arrays

A p-type Si(100) wafer was first coated with a 30 nm ALD ZnO layer. ZnO layer was additionally coated with a positive tone photoresist (AZ 5214) which was patterned by double exposure near-field phase shift lithography and developed in MIF 726 solution for approximately 1 minute. Note that the used mask is an inexpensive homemade borosilicate mask. The obtained resist patterns were then used as an etch mask to create patterned ZnO seed arrays with diameters <400 nm using reactive ion etching (RIE) with a gas mixture of 16:34:5 sccm CHF_3:CF_4:Ar at 200 watts of platen power. The etch duration was 4 minutes. Finally, the remaining photoresist residue was removed by acetone.

2.2 Atomic Absorption Spectrometry (AAS)

The concentration of Zn ions in the growth solution at different reaction stages was determined by an Analytik Jena: Vario 6 atomic absorption spectrometer (AAS). The samples were centrifuged at 4000 rpm for 10 min for removing the possible precipitates before the measurements.

3. Chapter 3

3.1 Synthesis of ZnO Nanowires and Hexabranched Nanostructures

Nanowires were prepared by the classic method. 15 mL of 12.5 mM solution of zinc nitrate and HMTA was contained in a glass tube. A piece of silicon (3cm×0.5cm) with a continuous annealed ZnO ALD layer or patterned ZnO dot arrays was inserted into the solution in slanting way. The bottle was sealed and kept at 90°C for 24 hours. After 24 hours the solution was cooled down and the sample was washed with deionized (DI) water and dried naturally. For hexabranched nanostructures, in addition to the precursor solution, 1 mL PEG was added to the solution and conducted the experiment in the same way.

3.2 Secondary Growth of ZnO Hexabranched Nanowires

In a typical experiment, nanowire samples of dimension 3cm×0.5cm prepared as described above were placed in 15mL precursor solution (zinc nitrate and HMTA, 12.5 mM) added with 1mL PEG. The bottle was sealed and kept at 90°C for 24 hours. After 24 hours the solution was cooled down and the sample was washed with DI water and dried naturally.

3.3 Photocatalytic Activity

The photocatalytic activities of various ZnO nanostructures grown on a Si substrate were investigated by using organic dye degradation under ultraviolet light. The test solution was aqueous solution of methylene blue (MB) (4mL, 2 µM) stored in a 10 mL glass beaker. The initial absorbance was measured by using a UV-Vis spectrophotometer (Perkin Elmer, Lambda 950). Then all the solutions with and without ZnO photocatalysts were exposed to UV (UV lamp XX-15S (UVP Inc.) with a wavelength of 254 nm and a power of 15 W. At each time interval the irradiation was paused and solution from each sample were taken out to quartz cuvettes for absorbance measurement. After the measurement the solutions were returned to the beaker and the irradiation was resumed.

4. Chapter 4

4.1 Synthesis of Sb-doped ZnO Nanowires

Sb-doped ZnO nanowires were prepared in the similar way as the ZnO nanowires were prepared. In addition to ZnO precursors Sb dopant solution was also added to the reaction mixture. The Sb dopant solution was prepared by the following method. Equal molar sodium hydroxide (NaOH) and glycolic acid ($C_2H_4O_3$) were dissolved in 10 mL water and kept stirring at 60°C for 30 minutes to form sodium glycolate ($NaC_2H_3O_3$). Then 0.1 M antimony acetate (SbAc3) was added to sodium glycolate solution. The ratio of antimony acetate to glycolate was kept at 1:12. In a typical synthesis 0.5 mL of Sb dopant solution was used.

4.2 Synthesis of Sb-doped Core-shell ZnO Nanowires

Sb-doped core-shell ZnO nanowires were prepared using the same method as the Sb-doped ZnO nanowires were prepared. In addition to ZnO precursors and Sb dopant solution, 1 mL of polyethylene glycol (Mw~400) was also added to the reaction mixture. Primary grown ZnO nanowire array was used as the substrate. The sealed bottle was kept at 90°C for 6 hours.

5. Chapter 5

5.1 Synthesis of Co-doped Core-shell ZnO Nanowires

In a typical experiment, ZnO nanowire array on silicon substrate of dimension 30 mm×5 mm were placed in 7.5 mL precursor solution in ethylene glycol (zinc nitrate and HMTA, 25 mM) added with 1 mL of cobalt nitrate solution in ethylene glycol (25 mM). The bottle was sealed with a glass stopper and kept at 170°C for 1 hour. After 1 hour the solution was cooled down and the sample was washed with DI water and dried naturally and annealed at 400°C for 1 hour to remove any precursor residues. Different volumes of cobalt nitrate solutions *viz.* 0.5 mL, 1mL, and 2mL and different time intervals *viz.* 1hr, 3hrs, 15hrs, and 24 hrs were also used in different experiments.

6. Chapter 6

6.1 Preparation of CuI Superstructures by Antisolvent Crystallization

Commercial CuI powder was dissolved in acetonitrile by ultrasonication for forming a transparent solution with a concentration of 6.0 g/L (solution A). Then 0.1 mL of water was added into 10 mL of solution A under stirring. Several droplets of the above solution were dispersed onto a silicon piece and dried at ambient conditions. White residues appeared on the silicon substrate after the solvent was evaporated. In the next experiment, 3 mL of water was quickly injected into 1 mL of solution A through a syringe pinhole (B.Braun-Sterican, 0.6 mm outside diameter of the needle) under vigorous magnetic stirring. The rapidly formed white precipitates were filtered and washed with deionized water and ethanol, and dried at room temperature.

7. Chapter 7

7.1 Preparation of CuI Superstructures by PVP-assisted Antisolvent Crystallization

In a typical experiment in the presence of organic additives, 3 mL of PVP aqueous solution (68.2 g/L) was injected into 1 mL of solution A through the syringe pinhole under vigorous magnetic stirring. After 30 min, cloudy white precipitates were collected by the removal of supernatant, followed by washing with deionized water and ethanol, and drying at room temperature. This experiment was also conducted by changing the injection sequence, injection speed, solution temperature and the concentration of PVP.

In addition, experiments were also performed by using 3 mL of Triton X-100 and 3 mL of PANI-isopropanol solution (1.4 g/L), respectively, instead of the PVP solution.

7.2 Adsorption Experiments

Adsorption experiments were carried out at room temperature. The as-prepared CuI-PVP and CuI-PANI rod-like superstructures (10 mg) were respectively dispersed into 4 mL of 20 mM MB aqueous solution by vigorous shaking for 30 s and then left for a specified time. The equilibrium concentrations of MB solution were measured with a UV-Vis spectrophotometer (Perkin Elmer, Lambda 950) at a wavelength of 664 nm corresponding to the maximum absorbance of MB. For comparison, the adsorbing property of the same amount of as-received CuI powder was also examined *via* the same process.

Acknowledgments

Kornelius Nielsch for their help with magnetic measurements. I thank Prof. Aurelio Mateo-Alonso, Dr. Elizabeth von Hauff, and Andreas Peukert for helpful discussions and their help.

I cannot find words to express my gratitude to Ms. Helen Pert at FRIAS. Without her help and support the life in Freiburg would not have been easy. I also would like to thank Aleksandra Tadic-Puzigaca and Dr. Britta Küst.

In my absence in Twente, the defense has been organized by Ms. Susan Janse and Ms. Satie Biharie. I owe my deepest gratitude to both of them.

I thank my friends Vidhu, Soumya, Prajisha, Sandeep, Sunil, Vignesh, Bobby, Deblina, Sagar, Amit, Musthafa, and Shahina.

Most of this thesis has been written from my hometown in India. My friends in Vellavayal have made this time enjoyable and motivating. I thank them for the get-togethers at Krishana Pillai Smaraka Vayanasala and entertaining tender coconut sessions.

This thesis would not have been possible without the encouragement of my family. My father Balachandran TV, my mother Ramani Kozhummal, my sister Sathi, my brother-in-law Rajesh, and my grand parents have always stood by me with great support. I also thank my niece Nandana for keeping me cheerful.

Finally, I would like to thank my wife Mili for her love and tireless supports.

Rajeevan Kozhummal
Karivellur, Kannur
India

About the Author

Rajeevan Kozhummal was born on 18th April 1986 in Karivellur, Kannur (India). He completed his Bachelors degree in Polymer Chemistry in the year 2006 from Kannur University, Kerala (India). In 2008, he finished his Masters from School of Chemical Sciences, Kannur University (India) in Chemistry (Material Science). He carried out his master's project entitled "Studies on Synthesis, Characterization, and Emulsion Co-Polymerization of Side Chain Liquid Crystalline Monomers" at Indian Institute of Chemical Technology (IICT), Hyderabad. After MSc he worked in Sree Chitra Thirunal Institute for Medical Science and Technology, Trivandrum (India) as a Junior Research Fellow. In July 2009, he joined as a PhD student under the guidance of Prof. Dr. Miko Elwenspoek and Prof. Dr. Margit Zacharias in Freiburg Institute for Advanced Studies (FRIAS), University of Freiburg (Germany) and Transducers Science and Technology, MESA+ Institute for Nanotechnology, University of Twente (The Netherlands). The results obtained from his PhD project are described in this thesis.

List of Publications

1. "Fabrication of micron-sized tetrahedra by Si<111> micromachining and retraction edge lithography"

    Kozhummal R., Berenschot E., Jansen H., Tas N., Zacharias M., and Elwenspoek M.

    J. Micromech. Microeng. **2012**, 22085032 (DOI:10.1088/0960-1317/22/8/085032)

2. "Homoepitaxial branching: an unusual polymorph of zinc oxide derived from seeded solution growth"

    Kozhummal R., Yang Y., Güder F., Hartel A., Lu X., Küçükbayrak U., Mateo-Alonso, A., Elwenspoek M.; and Zacharias M.

    ACS Nano **2012,** 6, 7133–7141 (DOI: 10.1021/nn302188q)

3. "Antisolvent Crystallization Approach to Construction of CuI Superstructures with Defined Geometries"

    Kozhummal R., Yang Y., Güder F., Küçükbayrak U.M., and Zacharias M.

    ACS Nano **2013**, 7, 2820-2828 (DOI: 10.1021/nn4003902)

4. "Superior functionality by design: selective ozone sensing realized by rationally constructed high-index ZnO surfaces"

    Güder F.,Yang Y., Menzel A., Wang C., Danhof J., Subannajui K., Hartel A., Hiller D., **Kozhummal R.**, Ramgir N.S. , Cimalla V., Schwarz U.T., and Zacharias M.

    Small **2012**, 8, 3307–3314 (DOI:10.1002/smll.201200841)

5. "Doping ZnO Nanowires in Solution while keeping the Nanowire Length: A Shell-doping Approach"

    Kozhummal R., Yang Y., Kübel C., Trouillet V., Bruns M., Görlitz D., Menzel A., Nielsch K., and Zacharias M.

    Manuscript submitted